Modeling Chromosomal Mosaicism During Early Human Embryogenesis on Microraft Array Platform

Ian Jan

A dissertation

submitted in partial fulfillment of the

requirements for the degree of

Doctor of Philosophy

University of Washington

2026

Reading Committee:

Nancy L. Allbritton, Chair

Hannele Ruohola-Baker

Cole DeForest

Program Authorized to Offer Degree:

Department of Bioengineering

University of Washington

Abstract

Modeling Chromosomal Mosaicism During Early Human Embryogenesis on Microraft Array Platform

Ian Jan

Chair of the Supervisory Committee:

Nancy L. Allbritton

Department of Bioengineering

Aneuploidy and chromosomal mosaicism in human embryos complicate predicting pregnancy outcomes already plagued with frequent pregnancy losses. Given the rapid increase of assisted reproductive technology (ART) treatments, there is a critical need to better assess the developmental potential of embryo candidates, especially in patients with poor prognoses. Emerging evidence suggests that human mosaic embryos can selectively eliminate aneuploid cells for healthy development; however, the mechanisms mediating this embryonic self-correction have yet to be systematically studied in humans. Because both technical and ethical limitations restrict studying cellular processes during early human embryogenesis, I will develop a novel platform to quantitatively screen and sort gastruloids—an *in vitro* multicellular model recapitulating cell fate and signaling during gastrulation—comprised of euploid and aneuploid human pluripotent stem cells (hPSCs). Analyzing single gastruloids is challenging by most current technologies, which only allow for low-throughput sorting or bulk analyses. Thus, new tools are required to systematically study the heterogeneity among gastruloids undergoing dramatic changes during self-organization. The project was divided into three Aims. Firstly, I developed an automated system to perform image-based screens of single gastruloids by isolating individual colonies for downstream analyses. Secondly, the emergence of gastruloid heterogeneity derived from multiple aliquots of a single cell line was quantified by coupling both phenotypic and transcriptomic information. Low-dimensional latent representations were created from imaging time-series using deep learning (DL) of developing gastruloids derived from hPSCs

expressing a SOX2-mCitrine reporter to track SOX2 dynamics. Among single gastruloids across multiple experimental batches, simple-to-complex variability in patterning behavior were assessed. Endpoint RNA-sequencing (RNA-seq) data from individually isolated gastruloids also revealed distinct clusters associated with batch and subclusters within batches. Thirdly, I assessed the phenotypic and transcriptomic differences between euploid and mosaic (derived from 50% euploid and 50% aneuploid cells) gastruloids to demonstrate the potential of this platform for studying chromosomal mosaicism during early human embryogenesis. The platform will enable future research to elucidate mechanisms for aneuploidy depletion critical for overcoming error-prone development and to improve reproductive treatments for an increasing number of patients.

ACKNOWLEDGEMENTS

Challenging me as both a scientist and thinker, this doctoral thesis could not have been possible without the intellectual, emotional, and physical support from those close to me. Thank you to Dr. Nancy Allbritton for trusting me with this novel project and guiding me through all the trials and tribulations. Thank you to the rest of the Allbritton group who made the lab a welcoming place—with special thanks to Cody LaBelle, Belén Cortés-Llanos, and Yuli Wang for training me in the art of the microraft array. Thank you to my collaborators—Dr. Min (Mia) Yang and Dr. Neda Bagheri—for providing me the resources and inspiration to address complex biological questions. Thank you to my undergraduate mentors—especially Dr. Joseph Schulz (the Cone Master) and Dr. Chris Craney—for preparing me so well for graduate school and beyond. Thank you to my family and Gina for their love. Thank you to all my friends who made Seattle feel like home even during a global pandemic. Last but not least, thank you to my feathery friends who gifted me the love for birding, a sense of community, and the appreciation of all the small yet important things in life.

TABLE OF CONTENTS

CHAPTER 1. INTRODUCTION

Human reproduction has a high failure rate, as only a third of conceptions result in live birth.[1] Error-prone and chaotic, early embryogenesis can give rise to mosaic embryos with both normal and aneuploid cells.[2–7] Chromosomal abnormalities exist in nearly half of miscarriages, which affect nearly 15% of pregnancies.[1] However, pregnancy failures are still poorly understood and challenging to predict. This further complicates assisted reproductive technology (ART) treatments that have doubled over the past decade.[8,9] Misdiagnoses by pre-implantation genetic testing for aneuploidy (PGT-A) are common and can have detrimental consequences, including embryo wastage and financial losses.[9–15] Mosaic embryos with low levels of aneuploidy—a likely common feature of early human embryogenesis—possibly have comparable reproductive potential and clinical outcomes as euploid embryos.[10–13,16–18] Moreover, success rates of mosaic embryo transfers vary between the different types of mosaicism distinguished by how the chromosomes are affected.[10,12,13] There is an urgent need to more accurately assess developmental potential and evaluate the heterogeneity of mosaic embryos.

Although mammalian pre-implantation models of mosaicism have demonstrated the selective elimination of aneuploid cells, a systematic study elucidating the mechanisms underlying this depletion in human post-implantation embryos is lacking.[16,19,20] My collaborator, Dr. Min Yang (UW Department of Obstetrics & Gynecology), revealed that human pluripotent stem cell (hPSC) colonies called two-dimensional (2D) gastruloids (or “gastruloids” for the rest of this dissertation) with sufficient euploid cells undergo bias of cell fate and culling of aberrant cells for the recovery of healthy development. However, the precise relationship between the proportion of aneuploid cells and patterning behavior, in addition to pathways involved in post-implantation aneuploidy depletion, are still largely unknown. Demonstrated in mouse and human pre-implantation models, complex aneuploidy induced autophagy and p53-mediated apoptosis in specific cell types.[19–21] Interestingly, the cell lineages eliminated differed between species, as differentiated cells in humans are more sensitive to aneuploidy than in mice.[19–21] Dr. Yang similarly observed greater aneuploidy-induced apoptosis in the differentiated germ layers; however, her study did not compare the levels of autophagy between the embryonic and trophectoderm lineages.[16] Although the depleted aneuploid cells displayed enhanced autophagy in both mouse and human pre-implantation models, her

preliminary results indicate that upregulating autophagy in post-implantation gastruloids instead helps preserve the embryonic fates. The dual role of autophagy in cell survival and death is highly context-dependent, like in human cancer,[22–24] thus I will assess the role of this process in aneuploidy depletion following human embryonic implantation.

To perform quantitative analyses of the dynamic cellular processes in chromosomally mosaic gastruloids, I will utilize a novel sorting platform capable of both high-throughput and -content imaging. Current technologies can neither feasibly monitor nor individually isolate whole colonies to study the heterogeneity among single gastruloids. The expected results of this proposed study will advance our understanding of the mechanisms underlying embryonic aneuploidy depletion, which is significant for clinical diagnosis of reproductive failure and has far-reaching implications for potential future fertility treatments. Moreover, my platform will support further research dissecting how normal embryo development overcomes frequent errors.[2,3,6] Chapter 2 will provide the areas of significance and innovation for this project in addition to necessary background information. In Chapter 3, I described the development of the automated screening and sorting platform for single gastruloids. The heterogeneity of single gastruloids was defined in both Chapters 3 (static imaging of endpoint gastruloids) and 4 (time-series imaging of developing gastruloids). In Chapter 4, I also investigated the role of autophagy in aneuploidy depletion. Chapter 5 discusses my contributions to projects with collaborators. Lastly, Chapter 6 provides conclusions to my research directions in Chapters 3 and 4.

CHAPTER 2. BACKGROUND

2.1. Early Human Embryogenesis

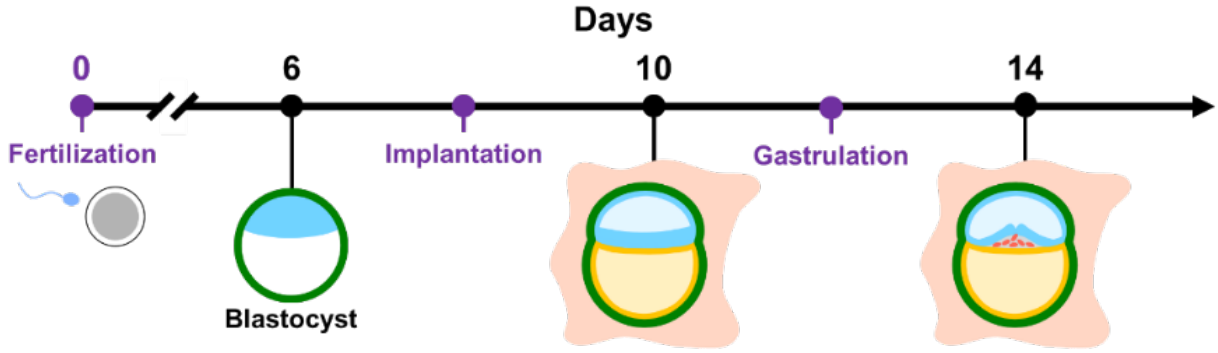

Fig. 2.1. Schematic of human embryogenesis timeline during first 2 weeks following fertilization.

The major events of the first three weeks of human embryo development include fertilization, implantation, and gastrulation [Fig. 2.1]. Undergoing cleavage or cell divisions following fertilization, the conceptus (encompasses the zygote and its surrounding membranes) becomes a 16-cell compacted structure called the morula.[25] Subsequently, the morula continues developing into a blastocyst consisting of the inner cell mass or embryoblast (eventually becomes the embryo) and the blastocoel (a fluid-filled cavity that will become the yolk sac) surrounded by the trophectoderm (later develops into structures for implantation and the placenta). The blastocyst will eventually adhere to the uterine lining by the second week. Specifically, the outer trophectoderm cells rapidly proliferate to form trophoblast cells that infiltrate the uterine lining [Fig. 2.2]. Cytotrophoblasts of the developing placenta differentiate into syncytiotrophoblasts. The syncytiotrophoblasts break down the endometrial cells of the uterine wall (forming a crypt) before firmly rooting the blastocyst. Additionally, the syncytiotrophoblasts form finger-like chorionic villi that interface the uterine arteries for the exchange of nutrients, gases, and waste. Blastocysts often fail to implant at this stage (50-75%) mainly because of the functional and morphological quality—which can be affected by karyotype variation—of the trophoblast

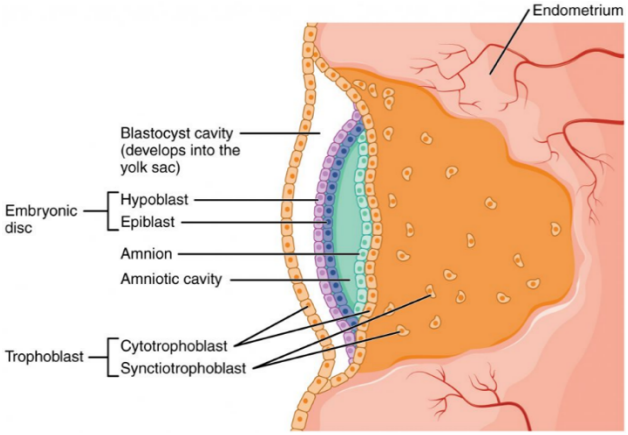

Fig. 2.2. Schematic displaying human blastocyst implanting into uterine lining. Reproduced from https://open.oregonstate.education/aandp/chapter/28-2-embryonic-development/.

cells.[1,25] Following implantation, the inner cell mass of the blastocyst forms a bilaminar or two-layered disk (the epiblast and the hypoblast).[25] The bilaminar disk is flanked by the amniotic cavity (eventually surrounds the embryo and later fetus in amniotic fluid as a form of protection) and the yolk sac (provides nourishment until the placenta replaces this function at approximately week 4). The dorsal and ventral axis is defined at this point where the dorsal and ventral side of the bilaminar disc contacts the amniotic cavity and the yolk sac, respectively. Furthermore, this bilaminar disk serves as the main stage of dramatic changes during the following developmental stage: gastrulation.

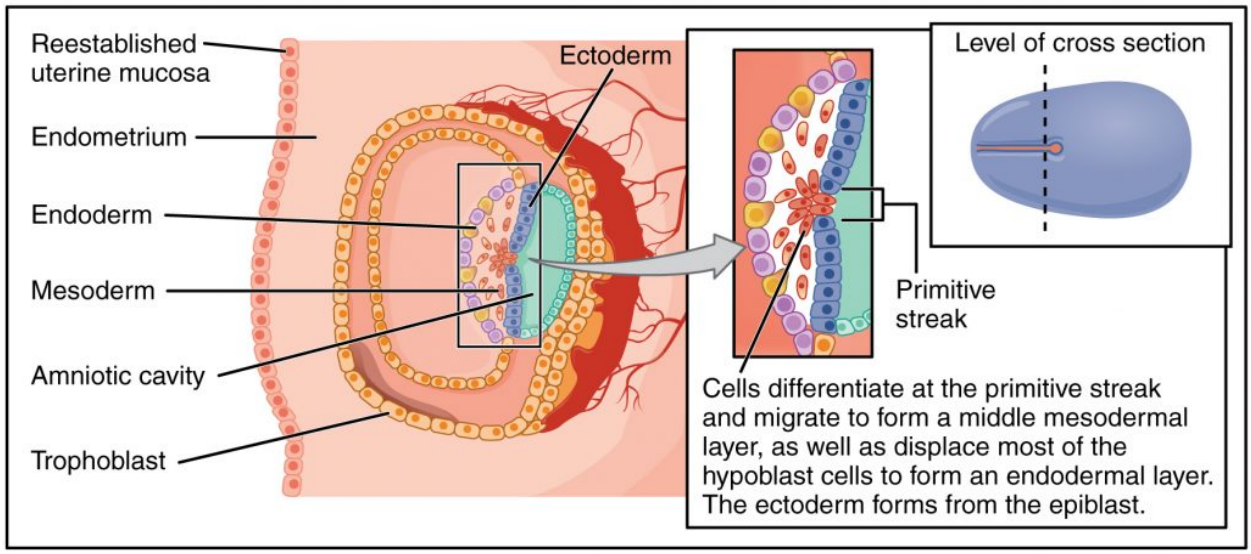

Fig. 2.3. Schematic displaying formation of germ layers at the primitive streak during human gastrulation. Reproduced and modified from https://open.oregonstate.education/aandp/chapter/28-2-embryonic-development/.

Gastrulation during the third week of development establishes the body axes and structural framework of the rapidly changing embryo [Fig. 2.3]. The primitive streak, an indentation along the longer axis of the now oval-shaped disk, develops from the caudal end to the cranial end (forms the primitive node) of the embryo.[25] This thereby creates the anterior-posterior axis. Epiblast cells undergo epithelial-to-mesenchymal transition (EMT) before migrating inward through the primitive streak to form the three germ layers: the endoderm (displaces the hypoblast and contacts the yolk sac), the mesoderm, and the ectoderm (cells that remain in the epiblast).[25,26] Each of the primary germ layers give rise to different organs.[25] The ectoderm forms organs including the nervous system and epidermis, the mesoderm develops into muscles and blood vessels, and the endoderm forms the gastrointestinal tract and the lungs. Notably, primitive streak formation varies greatly between vertebrates, thus species-specific differences must be carefully

considered in embryogenesis studies.[26] Conserved mechanisms include those involved in cell-cell and cell-matrix adhesion, chemotaxis and chemokinesis, and planar cell polarity. There is much yet to be understood about the complex and closely coordinated cellular dynamics that occur in early embryo development. Specifically, the key factors (like aneuploidy) that cause pregnancy losses present an important field of study.

2.2. Heterogeneity of Pluripotent Stem Cells

Possessing the ability to differentiate into any cell type, PSCs have been known to exhibit differences between cell lines, cells of the same line, and temporal states of single cells.[27] Both genetic and epigenetic factors that either are pre-existing or arise during cell culture drive this heterogeneity. Contributing to genetic variability are donor genetic background, specific clones with existing somatic mutations, and *de novo* mutations during PSC derivation. Culture conditions are also factors. Only for induced PSCs, the residual epigenetic characteristics of the original somatic cells and the reprogramming method contribute to the variability. Heterogeneity among cells in the same line can be caused by karyotypic changes, subchromosomal structural variants, and different stages in the cell cycle. Interestingly, PSCs fluctuate between different states at frequencies ranging from hours to days. For example, the important transcription factor for pluripotency maintenance, NANOG, is known to have dynamic expression levels throughout PSC populations. Tracking cells expressing live reporters, Nakamura et al. observed that cells produced sister cells with varying levels of NANOG expression independent of those of the mother cells.[28] Consequently, the temporal fluctuations of PSCs allow adaptability at the onset of differentiation.[27] These intrinsic dynamics can help explain the heterogeneities (emerging as early as the first cell divisions of embryogenesis) and have clinical implications for human reproduction.[29]

2.3. Chromosomal Mosaicism and Autophagy

The disruption of mechanisms regulating genome stability gives rise to aneuploidy. Monosomies result from the loss of single chromosomes from a diploid pair, while trisomies are caused by gaining an additional chromosome. Consequently, aneuploidy results in atypical relative copy numbers of genes on the affected chromosomes [Fig. 2.4].[7] Speculated as a fast but suboptimal mechanism for selective

advantages in extreme environments, aneuploidy is associated with general stress response-related phenotypes because of increased protein expression.[7,30] Features can include upregulation of immune response genes and downregulation of those involved in protein processing.[17,31,32] Most aneuploidies result in miscarriages or still births.[7] The exceptions include trisomy 21 (Down Syndrome) and aneuploidies related to the sex chromosomes.

Mosaicism can occur via mitotic error during early cleavage in euploid zygotes or by correction of aneuploid cells in blastomeres.[4] Moreover, there is a diversity of mosaicism categorized by the level of aneuploidy: simple (single chromosomal error), complex (more than one error), and chaotic (more than three chromosomally distinct cell populations).[33] The exact rate of mosaicism in embryos is unknown. But there is speculation that this is a common phenomenon in more than 70% of pre-implantation embryos.[5,17,18] Notably, PGT-A is plagued by limitations, including frequent misdiagnoses when sampling only a few cells from the embryo and interpreting results across multiple studies without standardization of practice.[10–13]

Accurately assessing developmental potential of embryos that may exhibit chromosomal abnormalities remains challenging. Multiple clinical studies observed healthy births following mosaic embryo transfers (METs); however, success rates vary depending on the different subgroups of mosaicism.[10,12,13] Mosaic embryos with low segmental chromosomal abnormalities have implantation rates of approximately 50% and ongoing pregnancy or birth rates of over 40%, while those with high-level complex mosaicism have much lower rates.[34] For reference, euploid embryos have implantation and ongoing pregnancy or birth

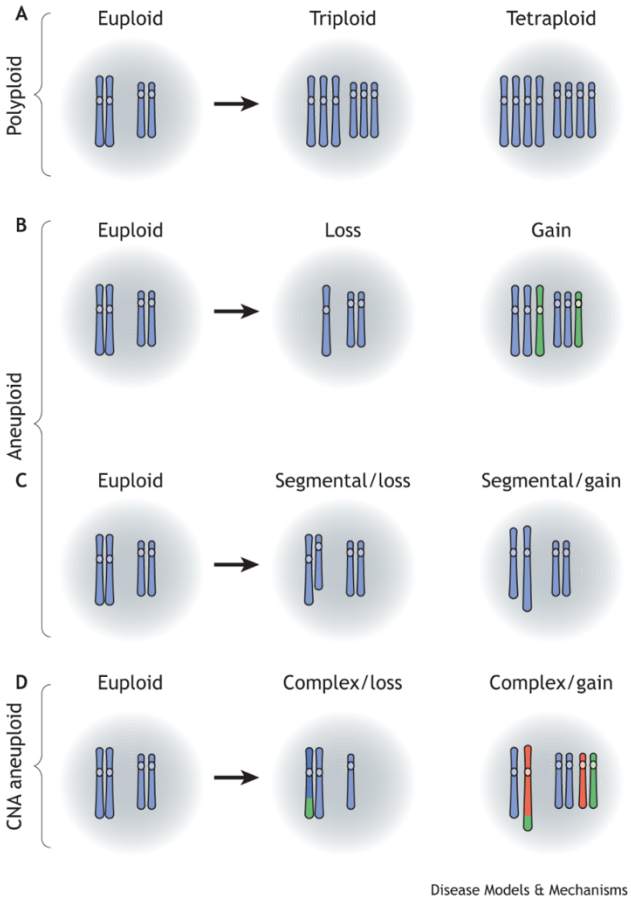

Fig. 2.4. Schematic visualizing polyploidy and aneuploidy. Copy number alteration (CNA). Reproduced from DOI: 10.1242/dmm.049673.

rates of 57.2% and 52.3%, respectively. Conflicting results from *in vitro* fertilization (IVF) reports call for further research to better understand the variable outcomes for mosaic embryos. Notably, proteomic analyses of poor-quality embryos show heterogeneity even among those derived from the same patient couples.[35] Comprehensive characterization of this variability can help establish a hierarchy of which embryo candidates to prioritize in poor prognosis patients without available euploid embryos.[10,12] These patients are characterized by advanced maternal age, multiple failed IVF cycles, low prior pregnancy rates, and high miscarriage rates. In a cohort study involving embryos deemed abnormal by PGT-A, 8 out of 19 clinical gestations resulted in live births of mainly euploid individuals.[10] Thus, such transfers are still feasible options.

	Mouse (pre- & post-implant)	Human (pre-implant)	Human (post-implant)
Depleted cell type	Embryonic	Trophectoderm	Embryonic
Pluripotency of depleted cell type	Yes	No	No
Autophagy levels in depleted cell type	Upregulated	Upregulated	**Unknown (possibly downregulated)**

Table 2.1. Comparison of aneuploidy depletion models in mice and humans.

Spatially confined into sub-millimeter-sized flat circles, gastruloids pattern embryonic (ectoderm, mesoderm, and endoderm) and trophectoderm-like lineages.[36] Yang et al. developed a self-organizing and tractable platform by treating RUES2 (NIHhESC-09-0013) hPSCs with 0.5 μM reversine (a small molecule inhibitor that disrupts chromosome segregation by inhibiting the spindle assembly checkpoint)[37] before seeding the cells onto arrayed circular micropatterned extracellular matrix (ECM).[16] Aneuploidy depletion can occur following implantation, so this gastrulation model serves as a biologically relevant platform.[5,16,38] Mainly, she revealed that the aneuploid cells bias toward a trophectoderm fate, which exhibited greater survivability to aneuploidy.[16] Measuring the cell death marker, CASP3, Yang et al. observed a disproportionate increase in apoptosis of aneuploid cells in the post-gastrulation embryonic lineages. Thus, this might explain the reduction of mosaicism post-implantation and confined placental mosaicism (CPM), which converts the majority of surviving mosaic embryos to euploid ones.[5,16] Since the placenta has a temporary function, the trophectoderm might tolerate aneuploidy more readily without causing harm to the developing embryo.[5,39] Utilizing an innovative approach (nuclear DNA labeling via mRNA electroporation, light-sheet live imaging, and semi-automated deep learning-based segmentation), Abdelbaki et al. revealed chromosome segregation errors in placental cells of preimplantation blastocysts.[40] Gastruloids are a relatively simple developmental model with limited structural and advanced development; however, this 2D system is highly reproducible and readily compatible with high-throughput technologies.[41]

Other mammalian aneuploidy models have demonstrated the depletion of selective cell types and the involvement of autophagy.[19–21] Studies conducted on mouse and human pre-implantation embryos reveal critical differences in embryogenesis between species, such as the aneuploidy-induced responses among cell lineages (embryonic vs trophectoderm) and the lower occurrence of aneuploidy in mouse embryos [Table 2.1].[20,21,42] Autophagy levels of human post-implantation embryos have yet to be studied. Moreover, analysis of human embryos exhibiting more defined aneuploidies (trisomy 15, trisomy 21, monosomy 21, and trisomy 16) demonstrated perplexing differences among the aneuploidy types, like the frequency of developmental arrest.[43] The study could not track the elimination of aneuploid cells but implied heterogeneity in the cellular responses to chromosomal abnormalities. Importantly, this can be modeled by complex aneuploidy. A novel image-based technology to assess large numbers of diverse colonies and to track aneuploid/euploid cells within their corresponding tissues of origin can address these important lingering questions.

Four hypothesis have been proposed to explain the depletion of aneuploid cells throughout early embryonic development: selective embryonic death, cell selection (or clonal depletion), cell correction, and preferential allocation.[4,5] Cell selection (specific cell types are depleted in favor of others) is related to selective embryonic death based on the proportion of abnormal cells within the population.[4,5] Meanwhile,

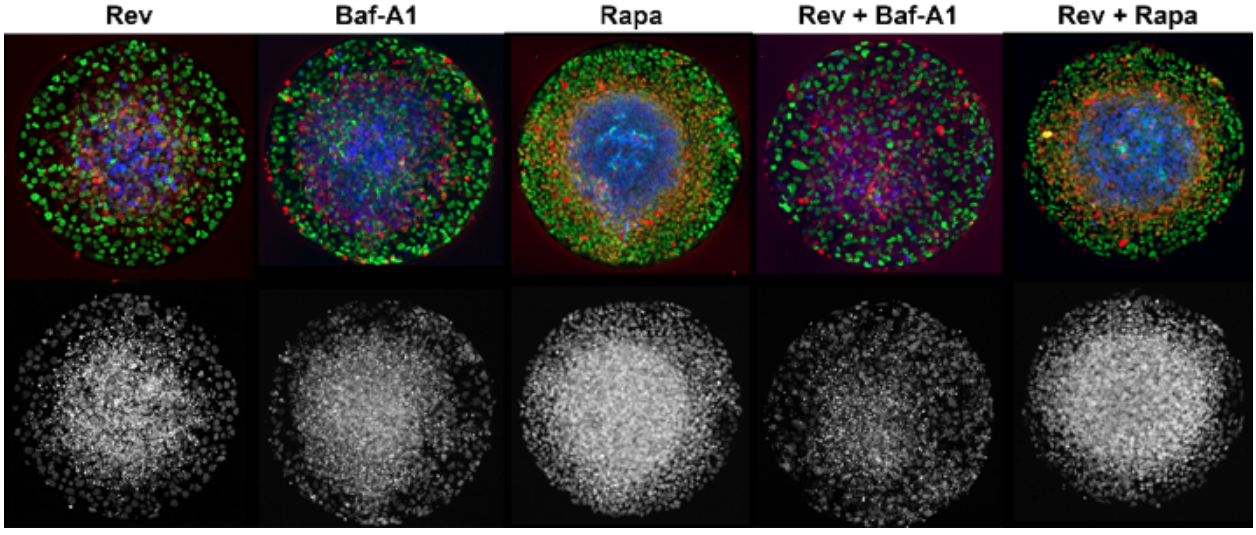

Fig. 2.5. Aneuploid (reversine-treated) or euploid gastruloids treated with bafilomycin A1 (Baf-A1) or rapamycin (rapa). Aneuploid gastruloids were derived from hPSCs treated with reversine. Treatments were concurrent with BMP4-induced differentiation; therefore, aneuploidy induction by reversine (rev) occurred after BMP4 signaling. SOX2 (blue), Brachyury (BRA) (red), and GATA3 (green) stained to indicate ectoderm, mesoderm, and trophectoderm, respectively.

cell correction (conversion from aneuploidy to diploidy via mitotic chromosome loss or gain) and preferential allocation (aneuploidy is resisted in the inner cell mass and enriched in the placental linages) are less supported theories than the first two.[4,5] The diverse types of cells in a post-implantation embryo are likely responding differently to the stresses introduced by chromosomal abnormalities.

Designed to limit cell death and tissue damage, the traditional inhibitory crosstalk between autophagy and apoptosis may be utilized to distinguish between non-lethal/lethal stress levels.[22] Cytoprotective autophagy occurs at lower stress levels, while higher stress levels lead to the subversion of these protective mechanisms. Notably, the complex role of autophagy in cell survival or death is highly context-dependent.[22,24,44] Autophagy can both deter and promote tumorigenesis and metastasis via the same machinery in human cancer. The mouse and human pre-implantation embryo with aneuploidy studies showed heightened levels of autophagy in the selectively depleted cell lines.[19,21] Singla et al. used bafilomycin A1 (Baf-A1)[42] and Atg5 siRNA[45] to disrupt autophagy, which decreased cell death in the inner cell mass of mouse embryos.[21] On the other hand, the authors used rapamycin[46] to induce autophagy by inhibiting mTOR but did not find a significant difference in the number of dying cells.[21] Singla et al. concluded that autophagy is required but not sufficient for aneuploid depletion.[21] However, preliminary studies by Dr. Yang using autophagy-deficient gastruloids treated with Baf-A1 showed loss of the embryonic fates [Fig. 2.5]. Autophagy-upregulated gastruloids treated with rapamycin instead demonstrated recovery. Reconciling these antithetical results is that autophagy often precedes—but not necessarily directly induces—apoptosis.[22] Moreover, Regin et al. clearly demonstrated that human embryos have different downstream responses to the same pathways as mouse embryos.[19] The role of autophagy in aneuploidy depletion has yet to be studied in human post-implantation embryos, which can be modeled by gastruloids.

2.4. Stem Cell-Based Embryo Models

Because of technical and ethical limitations, *in vitro* models derived from hPSCs have been developed to recapitulate key aspects of early embryonic development. “Stem cell-based embryo models (SCBEMs)” has been the more widely accepted term over other terms such as “artificial embryos” or “synthetic embryos” by the field for scientific accuracy and clarity for the public.[47,48] Mimicking biological processes from pre- to post-gastrulation, SCBEMs can be generally categorized into non-integrated

(recapitulate specific aspects of embryogenesis and typically lack extraembryonic cell types) or integrated (consist of both embryonic and extraembryonic lineages) models.[49,50] Non-integrated models include three-dimensional (3D) systems [e.g., peri-gastrulation trilaminar embryonic disc (PTED) embryoid, post-implantation amniotic sac embryoid (PASE), and neuronal gastruloid] and the 2D gastruloid (further discussed in detail in "2.5. Two-Dimensional Gastruloids").[49] Induced by chemical and physical triggers, non-integrated models are typically derived from a single PSC type prompted to undergo self-organization and differentiation. On the other hand, integrated models (e.g., blastoid, E-assembloid, bilaminoid) reach more advance stages of development than their non-integrated counterparts.

Although the most complex integrated models have yet to reach functional equivalence to *in vivo* embryos, SCBEMs have provided already important insights into the fundamental developmental processes [Fig. 2.6].[49] SCBEMs serve as important tools for translation research on studying diseases and disorders, assaying teratogens, and improving ARTs. However, given the complexity of human embryogenesis, these models are imperfect replicas. Each have their distinctive advantages and limitations. For instance, off-target differentiation, unclear cell type compositions, and disorganized tissue

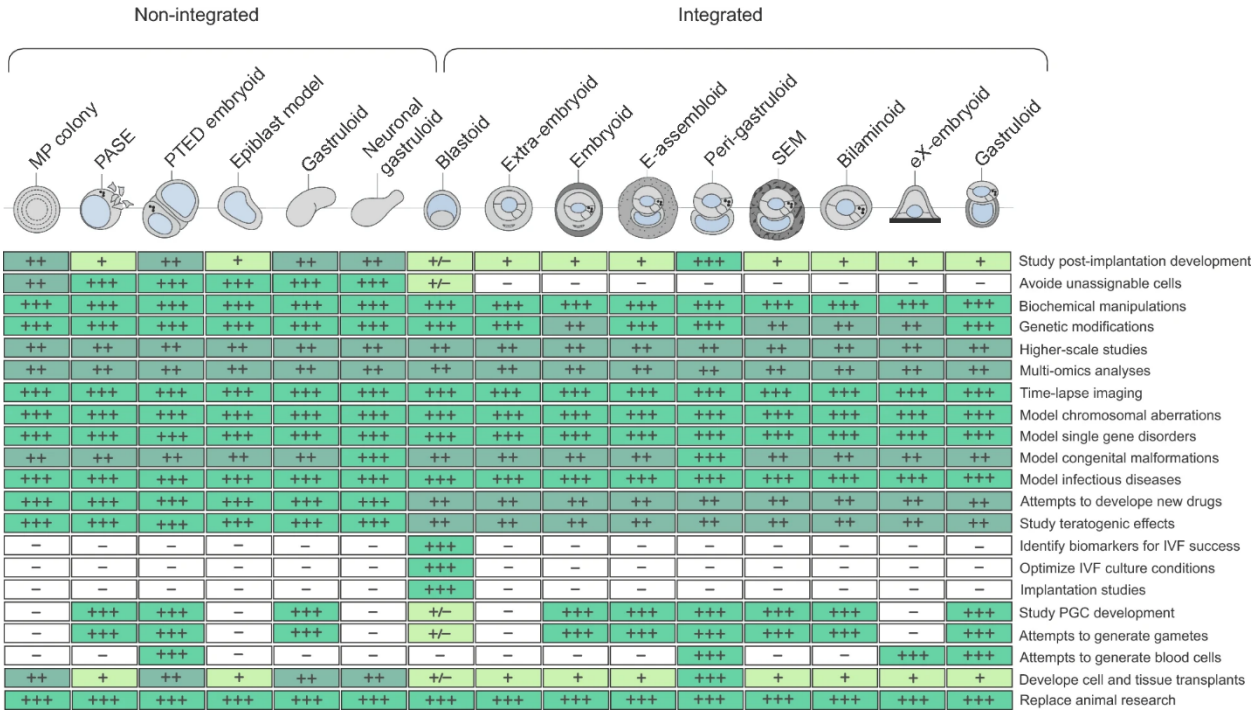

Fig. 2.6. Summary of applications of non-integrated and integrated SCBEMs. +, ++, +++ indicate increasing levels of applicability; +/- indicates only specific instances of model can be used; - indicates lack of usability. Reproduced from DOI: 10.1186/s13287-025-04581-2.

structures are current challenges plaguing SCBEMs. Importantly, the reproducibility of stem cell-based embryo models beyond their original report is a key issue, since model variability can exist between methods, batches, and even within the same batch.[49,51] There is an pressing need to evaluate the suitability of each model thoroughly during experimental design. Suggested benchmarking criteria include the cellular composition and states, spatial organization, morphology of the complete structures, spatiotemporal sequence of morphogenetic events, and correlation to developmental stages to target of modeling.[52] Standardized characterization of SCBEMs not only improves reproducibility of *in vitro* experiments but also guides regulatory oversight, which in turn helps foster public trust in developmental biology research.[47,52,53]

2.5. Two-Dimensional Gastruloids

To explore the spatial patterning that occurs during human gastrulation, Warmflash et al. developed a model system of 2D circular micropatterned (geometrically confined) colonies, called gastruloids.[36] They cultured the hPSCs onto micropatterned glass coverslips coated with Matrigel at full confluency before introducing homogenous BMP4 into the media. Notably, the self-organization of these gastruloids is induced via the interplay of BMP, Wnt, and Activin/Nodal signaling originating from the colony border. In comparison to standard hPSC cultures with variable morphologies, the micropatterned culture produced fairly consistent circular colonies with radially symmetric tissue regions [SOX2+ ectoderm, Brachyury+ (BRA) mesoderm, and CDX2+ trophectoderm-like] [Fig. 2.7]. Additionally, SOX2 is a pluripotency marker. The BRA+

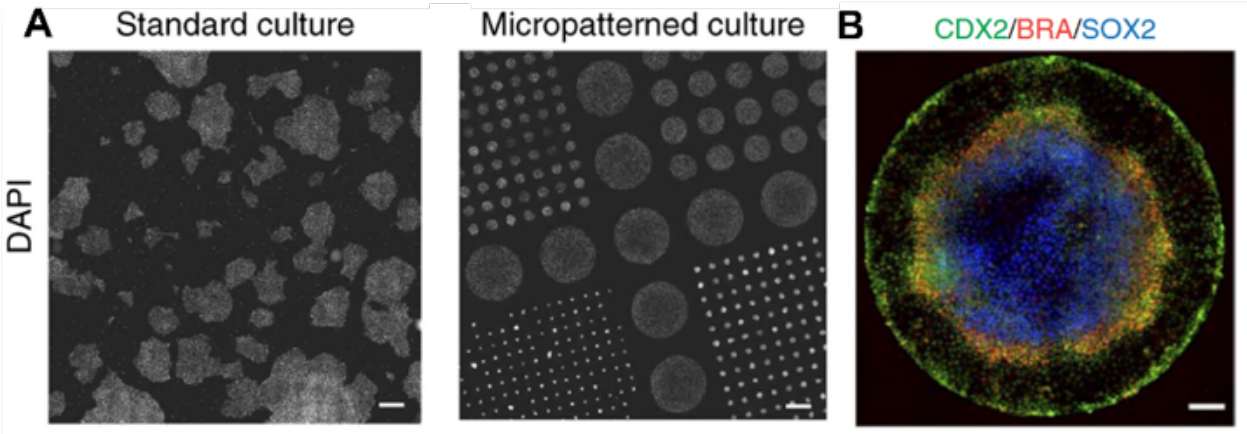

Fig. 2.7. hPSCs in micropatterned cultures undergo self-organization. (a) Stitched scans of RUES2 hPSCs grown in standard and micropatterned cultures. Scale bars, 500 μm. (b) Single gastruloid stained for germ layer (SOX2-ectoderm, BRA-mesoderm) and trophectoderm (CDX2) markers. Scale bar, 100 μm. Reproduced and modified from DOI: 10.1038/nmeth.3016.

mesoderm region of the gastruloids underwent EMT (similar to the epiblast cells migrating into the primitive streak) as demonstrated by upregulated pERK and SNAIL, and downregulated E-cadherin and EpCAM. This resulted in a multi-layered primitive streak-like region as the middle ring of the gastruloid. Inhibiting Activin/Nodal signaling downstream of BMP signaling via SB431542, Warmflash et al. noted the loss of the mesoderm region. This demonstrated the power to manipulate distinct populations within the gastruloids. Interestingly, gastruloids confined within microwells restricting the diffusion of signaling molecules showed inhibited mesodermal and endoderm differentiation, indicating the key role of diffusible signaling molecules for spatial patterning. The gastruloids importantly help elucidate specific details of self-organization during early human embryonic development otherwise inaccessible *in vivo* via the precise geometric control of hPSC cultures.

Chhabra et al. demonstrated the immense quantitative power of gastruloids by modeling the BMP-Wnt-Nodal signaling cascade underlying the spatial patterning [Fig. 2.8].[54] During the first 12 h of the BMP4 treatment, widespread BMP signaling became restricted to the gastruloid edge via receptor localization and NOGGIN (BMP antagonist) expression. Subsequently, dynamic Wnt and Nodal signaling established the mesoderm. Inconsistent with the popular diffusion-drive Turing instability model, the inward waves of Wnt and Nodal signaling created a homogenous final state derived solely from boundary effects and not a stable

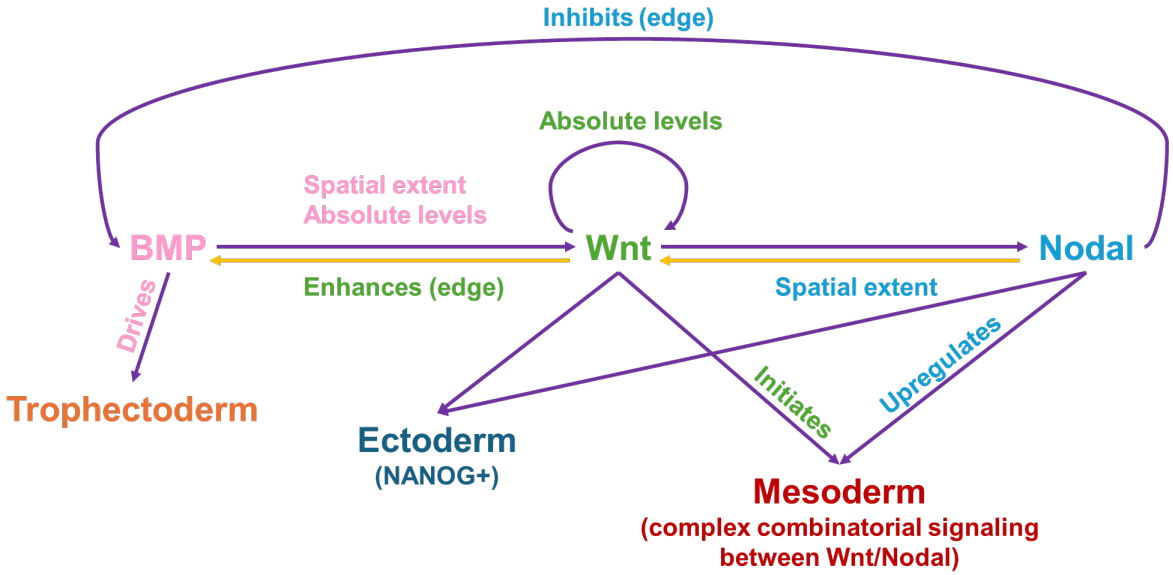

Fig. 2.8. Schematic of the BMP-Wnt-Nodal signaling cascade underlying patterning of the trophectoderm, ectoderm, and mesoderm.

gradient. Wnt and Nodal signaling triggered mesoderm differentiation in a middle ring-like region. The expression of NANOG (pluripotency marker found in the ectoderm) was high at the center of the gastruloid. Meanwhile, BMP4-induced BMP signaling drove trophectodermal differentiation at the edge, revealed by comparing the transcriptomes of these cells with those of pre-implantation human embryos. BMP controlled the spatial extend and the absolute levels of Wnt; however, Wnt and Nodal mutually controlled only the spatial extent of each other. Lastly, Wnt enhances while Nodal inhibits BMP at the edge of the gastruloid. Chhabra et al. summarized their data by devising a simple model for signaling dynamics and cell fate patterning that accounts for not only size but also shape of the micropatterned colony.

Although this simplified system has limited morphogenesis and lacks most 3D structures of a human embryo, gastruloids exhibit quantitative self-organization and spatial patterning. For example, this micropatterned model system has been used as a high-throughput platform to screen multiple hPSCs lines to determine biases for lineage specification.[55] Specifically, Nodal expression acts as a switch for gastrulation- or preneurulation-associated gene profile expression. But current analytical technologies severely limit the throughput and sample size of studies, which typically perform bulk analyses concealing the differences between individual gastruloids. In contrast, I expect intrinsic heterogeneity among the gastruloids even under homogeneous culture conditions because of well-documented fluctuations on the single-cell level and the stochastic seeding of cells.[27,56,57] Cell density affects receptor relocalization within gastruloids, thus micropatterns with greater cell density result in an enlarged ectodermal layer.[58,59] Gastruloid heterogeneity is masked by pooling gastruloids as biological replicates or bias from manually selecting seemingly representative gastruloids. Consequently, there is a need for technological innovations to study the diversity of single gastruloids.

2.6. Microraft Array for Novel Screening and Sorting of Gastruloids

The systematic sorting of gastruloids has yet to be demonstrated. Moreover, manipulation methods for heterogeneous microtissues, especially adherent cultures, are a relatively understudied area since most sorting is performed to enrich specific sample types.[60] Single-cell sorting techniques would require dissociation and disrupting the adherent gastruloids. Current methods for isolating multicellular structures can be tedious, complex, and or similarly disruptive. Importantly, an automated system that can both screen

and sort heterogeneous gastruloids feasibly will empower quantitative studies of early human embryogenesis.

As a novel high-throughput sorting method for 2D adherent microtissues, the microraft array provides unique advantages over current technologies [Fig. 2.9]. The polydimethylsiloxane (PDMS) microwell array comprises of hundreds of uniform and releasable polystyrene "microrafts," which can culture distinct colonies.[61–63] Superparamagnetic beads embedded in the microrafts enable the precise release and collection of individual microrafts by a thin needle and magnetic wand, respectively, for downstream analyses like RNA sequencing (RNA-seq). This allows for gentle cell sorting. The technique does not require detaching the cells, and the microraft manipulation tools do not directly contact the biological cargo. Furthermore, the automated imaging and sorting system developed for the microraft arrays eliminates laborious and variable manual processing. The microraft array technology has been proven in a myriad of applications, from single pancreatic cancer cells to multicellular intestinal organoids.[64,65] Notably, Cortés-Llanos et al. provides a comprehensive review of this platform.[62]

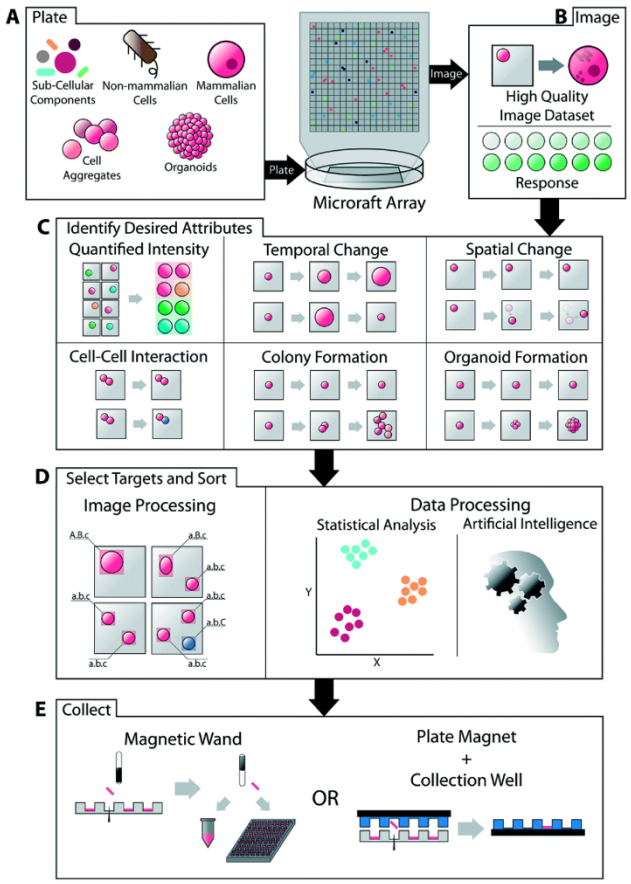

Fig. 2.9. Schematic overview of microraft array workflow. Reproduced from DOI: 10.1039/D1LC00506E.

To perform large-scale screens with gastruloids based on complex dynamic phenotypes, I designed a novel microraft array suitable for the high-throughput screening of individual gastruloids. There are multifaceted innovations in my work. I mated surface patterning technologies with the microrafts for gastruloid formation. Subsequently, I implemented the high-throughput platform to image arrays of gastruloids and quantitatively assess the various phenotypes present. To analyze gene expression dynamics, I incorporated transcriptomic assays for single isolated gastruloids. This platform enables assays

of statistically significant numbers of the gastruloids to better understand their physiology and variability. I investigated the mechanisms, such as autophagy, underlying distinct patterning behavior.

2.7. Deep Learning for Microscopy Image Analysis

Machine learning (ML) is a powerful mathematics-based tool to extract insights from large and complex datasets to make decisions or predictions. The algorithms are designed to solve problems without explicit instructions. But, human engineering is crucial to collect and organize the data, make critical assumptions about the problem, optimize the type and parameters of the algorithm, and validate the final solution.[66] There are two main types of problems to solve: classification (categorizing data into discrete classes) and regression (mapping data to a continuous output). In essence, ML is an optimization problem. When fitting ML models to data, the algorithms are optimizing the objective function, which is generally the sum of the training error (penalties for wrong predictions) and the regularizer function. The regularizer is designed to prevent the model from overfitting to the training data (model performs well on the training data but poorly on new data). On the other hand, underfitting is where the model is too general and did not gain any meaningful information from the training data. Training is an iterative process to achieve the most optimal parameter of the objective function. Because ML is limited to only linear functions, analyzing more complex data can be difficult.

In response, deep learning (DL) is a subset of ML and is based on neural networks (NNs) that model non-linear functions for more flexibility.[66] The basic unit of a NN is a neuron, which consists of weights and a non-linear activation function. The pre-activation value is determined by applying the weights to the input and passed through the activation function to produce the final output. NNs are constructed from multiple neurons arranged in both parallel and series. Each sequential neuron is called a layer, and a single layer can consist of multiple parallel neurons. Even though theory serves as the foundation for designing NNs, empirical testing is necessary to tailor NNs for solving diverse sets of problems. Hence, DL is a constantly evolving field with important applications from text processing to image analysis.

Recent efforts have been focused on developing DL for biomedical research, especially to process microscopy images for large-scale screens. Convolutional layers that apply sliding matrices called filters

(performs mathematical transformation) are used to detect features such as shape or texture.[66,67] Hence, the output of convolutional layers are termed feature maps.[67] Downsampling (reducing data) and upsampling (increasing data) are performed to distill or expand information from the images, respectively. To translate images to non-image outputs, fully connected layers (each neuron is connected to every neuron in the previous layer) are used to convert feature maps into values for classification or regression. These tools serve as important building blocks for NN architectures.

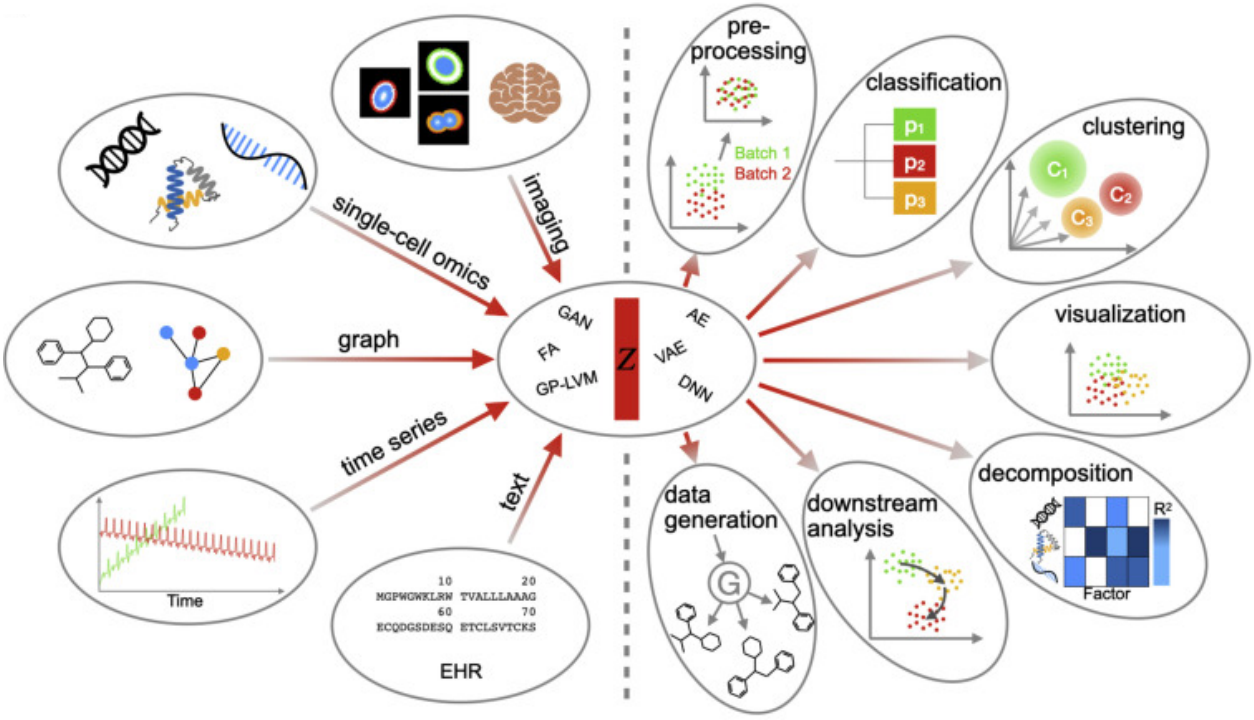

Fig. 2.10. Schematic overview of LRL applications in biomedical research. Reproduced from DOI: 10.1016/j.patter.2021.100198.

There are a wide range of image analysis tasks, including object segmentation, denoising, and latent representation learning (LRL). LRL, or also latent variable modeling (LRM), involves extracting latent features (that constitute latent representations or embeddings) from empirical measurements in an unsupervised manner [Fig. 2.10].[68] For LRL, using DL instead of manually extracting features can reduce human bias and uncover nuanced patterns. Some patterns are difficult to easily interpret or quantify with simple metrics. Latent representations can handle high levels of abstraction ideal for high-dimensional and complex data. Moreover, latent representations are also important assets for downstream analyses, such as clustering or classification.

One powerful DL approach for LRL is the autoencoder (AE) (characterized by its symmetrical architecture shape) that compresses the data through a bottleneck, thereby creating the latent representation used to reconstruct the input data [Fig. 2.11].[67,68] For example, Chen et al. utilized an autoencoder-based framework to model dynamics of human embryoids from a dataset of over 3,600 fluorescent images.[69] Distilling information from the images to low-dimensional latent representations, Chen et al. determined the minimum number of dimensions to capture essential features. The embeddings also allowed the generation of artificial embryoid images at a finer temporal resolution than that of the experimental dataset. Alternatively, the variational autoencoder (VAE) maps the latent representation as a distribution defined by a mean and standard deviation [Fig. 2.11].[68,70] VAEs provide benefits by modeling the distribution of the input data, such as allowing interpolations within the latent space and producing realistic synthetic reconstructions.[70] In contrast, AEs are simpler, less computationally intensive, and better suited for tasks where the generated reconstructions are not essential. Both have the potential of discovering hidden patterns in the training data when prior knowledge is not readily available.

DL has great potential for solving difficult problems; however, there are crucial considerations because of its high complexity and resource demands (e.g., data, computational hardware, etc.).[66,67] No single universal algorithm exists for all problems.[66] Thus, model design requires careful assessment of key assumptions to tailor the model specifically for particular sets of problems. Another aspect of human

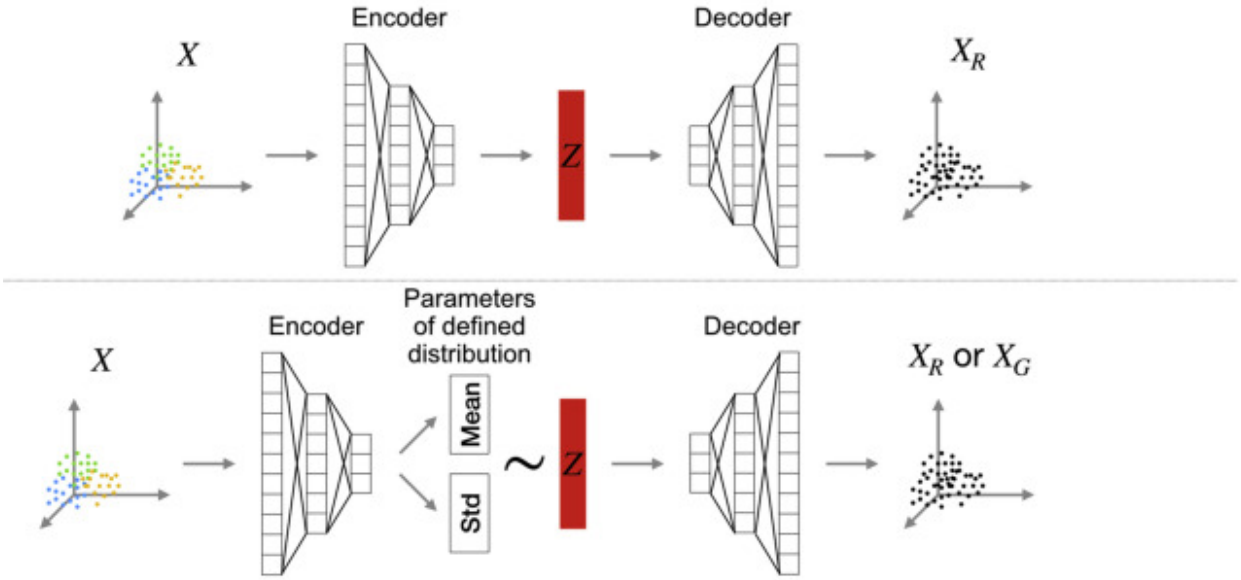

Fig. 2.11. Schematic visualization of autoencoder (AE) (top) and variational autoencoder (VAE) (bottom) for LRL. Reproduced from DOI: 10.1016/j.patter.2021.100198.

engineering is interpreting NNs.[67,68] Gradient- and/or perturbation-based methods can be used to trace latent representation dimensions to physical features.[67] Gradient-based methods involve visualizing gradients, or changes, to the weights of the NN typically via heatmaps. Perturbation-based methods involved perturbing, or modifying, specific features in a model to observe human-interpretable changes in the output. NNs can also be forced to encode biologically disentangled representations that correspond to highly distinct features for straightforward interpretation. Generating exaggerated counterfactual explanations by perturbing individual latent dimensions, Rotem et al. identified size and trophectoderm quality as key features correlated with embryo quality for IVF.[71] Notably, the researchers revealed blastocoel density, which is difficult to explicitly quantify, as a novel feature that was not previously known by expert embryologists.[71] ML and DL approaches are invaluable for LRL for their immense flexibility, including handling beyond single modalities.

The emerging trend of integrating multiple data types, especially imaging and multi-omics, for comprehensive analyses of biological samples confronts the challenge of handling high dimensional information.[70] Integration can be performed in different ways: early (modalities are concatenated as a single input), intermediate (modalities are kept as separate inputs but either passed through an integrated model or shared latent space), or late (separate models for each modality but predictions are combined into final aggregated result).[70] For instance, chromatin images and spatial transcriptomics were jointly used to reveal distinct subpopulations among naïve CD4+ T-cells and to identify biomarkers for Alzheimer's disease.[72,73] A clinically useful application is predicting spatial transcriptomics from histological images as a more cost-effective and accurate technique to study the spatial variation within tissue.[74–76] As a nondestructive way to evaluate hPSC culture quality, morphological latent representations extracted from phase-contrast imaging of hPSCs were used to predict gene expression of reprogramming-related genes.[77] These applications are mainly motivated by the use of high-throughput imaging to acquire information that can only be provided by more costly or destructive downstream assays.

In Chapter 4, LRL was performed using time-series widefield imaging of gastruloids derived from hPSCs expressing a fluorescent germ layer reporter (SOX2) to assess the reproducibility of the model system. Furthermore, the relationship between imaging and sequencing data was evaluated for both

euploid and mosaic (consisting of 50% euploid and 50% aneuploid cells) gastruloids. This integrated workflow for single gastruloid analysis serves as a powerful tool to probe the complex and subtle processes underlying early human embryonic development.

CHAPTER 3. DEVELOPMENT OF LARGE SCALE GASTRULOID ARRAY TO IDENTIFY ABERRANT DEVELOPMENTAL PHENOTYPES

Chapter 3 has been adapted from the following: Jan, I., Cearlock, A., Yang, M. & Allbritton, N. L. Development of large-scale gastruloid array to identify aberrant developmental phenotypes. APL Bioengineering 9, 026121 (2025).

3.1. Introduction

Models of human embryogenesis have enabled detailed investigations into early human embryo development as well as translational research into the mechanisms of pregnancy failure and formation of congenital defects. Often derived from human pluripotent stem cells (hPSCs), these models recapitulate specific stages of embryo development with both three-dimensional (3D) and two-dimensional (2D) multicellular structures.[41,78] In particular, 2D gastruloids are an elegant model developed to recapitulate the cell fate decisions and spatial patterning that occur in early embryogenesis.[36] For simplicity, this report will refer to 2D gastruloids as “gastruloids.”[78] Despite lacking a complex 3D structure, gastruloids have led to many breakthroughs, from detailed models of the signaling cascade that occurs during gastrulation to discovering that early stages of Huntington’s disease can occur within the first two weeks of development.[54,79] Gastruloids are formed by culturing on and confining hPSCs to a flat extracellular matrix (ECM)-coated surface of 0.5-1 millimeter in size. Addition of bone morphogenic protein 4 (BMP4) to the circular, confluent cell colony triggers a signaling cascade initiated at the gastruloid edges and sweeping across the cells to the innermost regions.[54] Utilizing key signaling pathways such as the BMP, Wnt, and Nodal, the colony self-patterns to form concentric rings of the three germ layers (ectoderm, mesoderm, and endoderm) and the extraembryonic trophectoderm-like cells.[54] Receptor localization and expression of noggin (NOG), a BMP antagonist, restrict the initial widespread BMP signaling to the edge of the gastruloids.[54] Comparative transcriptomic analysis has revealed that cells at the gastruloid edge resemble trophectoderm-like cells, which contribute in forming the placenta.[54] Specifically, BMP-treated cells display an upregulation of both preimplantation trophectoderm markers (such as CDX2, GATA3, and keratin 7 (KRT7)) and post-implantation cytotrophoblast markers (including TFAP2A and SPINT1).[54] The cell lineages of the germ layers are later formed in the gastruloids via the combinatorial signaling of Wnt and

Nodal.[54] Although gastruloids have limited morphogenesis, this efficient system with a short induction time has the potential to form hundreds to thousands of microtissues exhibiting quantitative self-organization and consistent spatial patterning for large-scale, fast screens.[41] A recent powerful application of gastruloids is studying the effects of aneuploidy (possessing abnormal numbers of chromosomes) during early embryo development.[16] The fate of aneuploid cells in gastruloids is biased towards the extraembryonic trophectoderm lineage, while euploid cells give rise to the germ layers and trophectoderm to accomplish normal embryonic patterning.[16] How the self-organization of gastruloids differs with the presence of aneuploid cells is not fully understood. During normal patterning, NOG acts as an inhibitor of BMP signaling and is upregulated at the colony center, thereby restricting BMP signaling at the colony edges.[54,58] Reversine is an easy way to model aneuploidy *in vitro,* as the small molecule induces heterogeneous aneuploidy by inhibiting monopolar spindle 1 (MPS1) kinase during mitosis and thereby disrupts chromosome segregation.[37] However, current analytical technologies are unable to sort single gastruloids feasibly and dissect the heterogeneity of this multicellular model of human embryogenesis undergoing complex cellular processes.

Studying heterogeneity on a multicellular level, akin to the heterogeneity observed among single cells, can shine light on complex biological processes. The ongoing development of powerful single-cell screening technologies has been driven by the ability to characterize phenotypically distinct cells within a diverse population.[80] Because the development of organized multicellular entities requires concerted interactions between multiple cell types, the resulting diversity between seemingly identical microtissues is a rich area of study. A variety of high-throughput screens have been conducted on small model organisms or microtissues—including the nematode, fruit fly, and zebrafish—and human multicellular cultures.[60,81–83] For sorting worms, macro-scale flow cytometry and microfluidic-based methods are used depending on whether throughput or information content are prioritized.[81–83] Microfluidics are also used to sort fruit fly embryos, which are important for studying genetics and developmental biology.[82] In addition to phenotypic screening in microtiter plates of zebrafish embryos or larvae, flow cytometry and microfluidic devices are also used albeit with challenges stemming from the larger size of zebrafish embryo/larvae compared to worms or fruit fly embryos.[81,82] Human multicellular cultures can also be sorted with hydrodynamic techniques, including microfluidic chips and pipetting-based systems that release cells by scraping and

aspirating adherent cell colonies.[60] While scraping could offer the flexibility of isolating specific gastruloids, the method is slow, tedious, and disrupts the structure of single colonies. Hydrodynamic tools apply fluidic forces that can perturb delicate structures within colonies and cause cell damage, a significant shortcoming for delicate structures.[60,81,83] Microfluidic systems often require complex control systems and can be difficult to use in biological investigations. As a result, current biological sorting technologies still face challenges such as sorting based on multiple parameters, easy integration with downstream applications like transcriptomic analysis, and handling surface-adherent entities with complex spatial organization. An example entity lacking a compatible high-throughput sorting platform are the large-sized gastruloids grown on a flat patterned surface. The systematic sorting of gastruloids has yet to be demonstrated, as the colonies are either manually isolated in small numbers or pooled in bulk analyses that blur inherent colony heterogeneity. Manipulation methods for heterogeneous microtissues, especially adherent cultures, are a relatively underdeveloped area since most traditional sorting is performed to enrich specific sample types.[60] An automated system that can both screen and sort gastruloids would empower quantitative studies of early human embryogenesis.

The microraft array platform provides unique advantages over current technologies as a novel high-throughput sorting method for 2D adherent microtissues.[62] The polydimethylsiloxane (PDMS) microwell array comprises of hundreds of uniform and releasable polystyrene “microrafts,” which support distinct cell colonies. Superparamagnetic beads embedded in the microrafts enable the precise release and collection of individual microrafts by a thin needle and magnetic wand, respectively. This permits gentle cell sorting since the technique does not require cell detachment and the microraft manipulation tools do not directly contact the biological cargo. Furthermore, the automated imaging and sorting system developed for the microraft arrays eliminates laborious and variable manual processing. The microrafts have been used in large-scale screens for a diverse range of applications, from pancreatic cancer cells to intestinal organoids.[62] Welch et al. sequenced single drug-resistant pancreatic cancer cells isolated from a heterogeneous population based on phenotypes such as cell surface markers and cell proliferation in response to cytotoxic drug treatment.[64] The drug-resistant cells displayed gene expression changes in genes involved in active cell growth and endoplasmic reticulum stress response.[64] To address challenges in T-cell-based cancer immunotherapy development, LaBelle et al. performed robust time-lapse imaging to

measure temporal cellular metrics and sorted single helper T cells (CD4+ T lymphocytes) undergoing different rates of proliferation when stimulated by feeder cells presenting cancer-antigens.[84] Gracz et al. assayed 3D intestinal organoids derived from intestinal stem cell and niche cell co-cultures to understand the self-renewal and differentiation of somatic stem cells.[65] Notably, the intestinal organoids formed two distinct morphologies and corresponding gene expression profiles.[65] The microraft array platform has demonstrated immense adaptability to sort a myriad of heterogeneous biological cargo—adherent or suspended cells, single cells or multicellular colonies, robust or fragile cell types—while maintaining high post-collection viability and purity.[62] Furthermore, the ability to probe both functional and transcriptomic heterogeneity is an useful asset to understand the complex mechanisms involved in crucial biological processes.

In this work, the microraft arrays were developed for the screening and sorting of adherent, patterned microtissues such as gastruloids. Enhancements in the microraft fabrication and isolation process were implemented to accommodate enlarged microraft geometries compared to prior work.[62,64,65,84–87] The size and flatness of the microrafts were optimized for the near-millimeter-sized gastruloids with modification of the fabrication workflow. To accomplish micropatterning of the surface of every microraft on an entire array, a novel photopatterning approach was developed to center circular ECM islands for cell adhesion. Quality control of the geometry and patterning of the microraft-based gastruloids was performed by comparison to gastruloids cultured on flat multi-well plates. Previous iterations of this technology with small (sides measuring <200 μm) and concave microrafts were not compatible with the near-millimeter-sized gastruloids. An automated imaging system was optimized for the large microrafts, and a novel computational pipeline was devised to classify normally or abnormally patterned gastruloids. An experimental workflow was developed to scan an entire array of gastruloids and identify colonies with specific morphological features for sorting prior to downstream analysis. Target microrafts were isolated with an automated release and collection process customized for the very-large sized microrafts. The capabilities of the modified platform were demonstrated by sorting gastruloids derived from euploid or aneuploid hPSCs based on the DNA content normalized to the total gastruloid area. Moreover, the expression of NOG (inhibitor of BMP signaling critical in spatial patterning)[54] and KRT7 (preimplantation trophectoderm marker)[88] in euploid and aneuploid gastruloids was assessed. The straightforward

integration of image-based phenotyping and gene expression analysis of single gastruloids empowers future studies of thousands of gastruloids to explore the heterogeneity of both this model system and early human embryonic development.

3.2. Methods

3.2.1. Microraft Array Fabrication

Microraft arrays were fabricated using modified protocols previously described [Fig. 3.1].[61,84] The master templates were fabricated from 1002F-100 negative photoresist (custom-made according to protocols described by Pai et al.)[89] using a photomask with 800 μm x 800 μm openings spaced by 100 μm in a 23 x 23 grid via photolithography. The square features of the master templates to form the microwells possessed an average height of 104±3 μm and width of 777±7 μm with an average gap of 107±3 μm between the features (N=5 templates) [Fig. 3.2]. Subsequently, the 300 μm thick arrays were replica molded in polydimethylsiloxane (PDMS) (#2065622, Dow Silicones Corp., Midland, MI) to form 529 square microwells by soft lithography. A solution of 2.5% superparamagnetic γ-Fe_2O_3 beads (#MC3000-10, Ocean NanoTech, San Diego, CA) in gamma butyrolactone (GBL) (#B103608, Sigma-Aldrich, St. Louis, MO) settled evenly within the microwells as the arrays continuously swirled at 8.5 rad/s for 10 min. Subsequently,

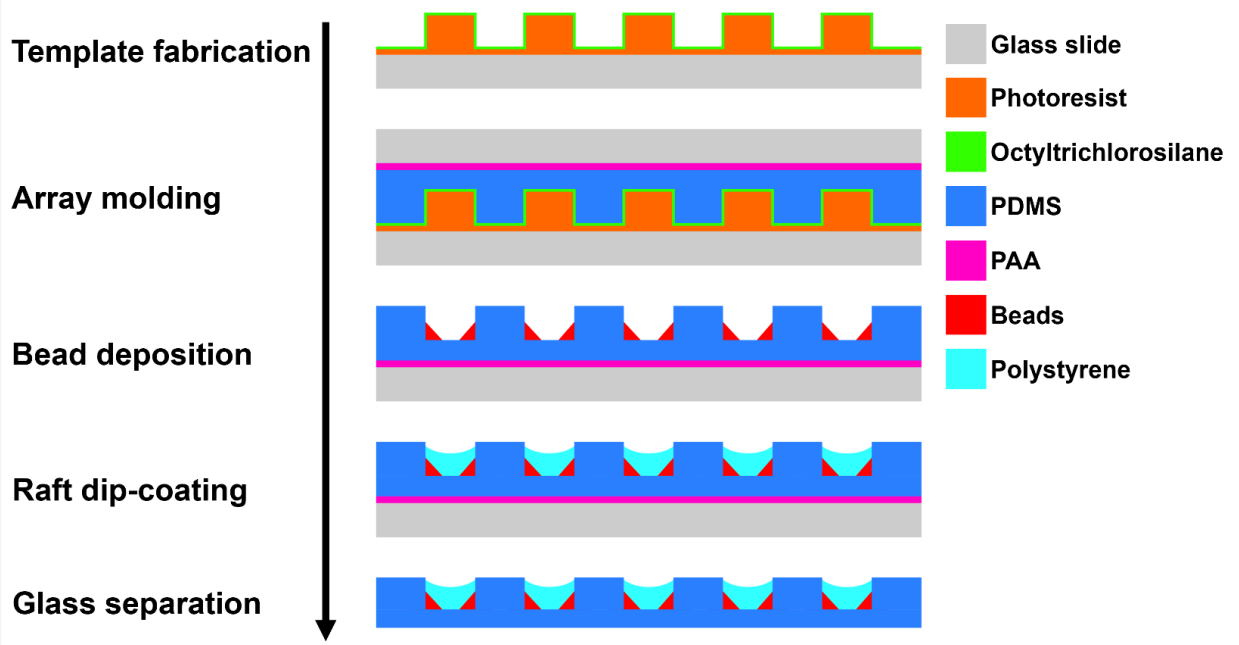

Fig. 3.1. Schematic of microraft array fabrication. Array is flipped 180° following the array molding step.

the arrays were incubated at 95°C for 30 min to evaporate the GBL, during which the beads were drawn to the microwell corners because of surface tension. Dip-coated in a 20% poly(styrene-co-acrylic-acid) solution in GBL [plastic petri dishes (#353001, Falcon, Corning, NY) dissolved in GBL], the arrays were baked at 95°C overnight to evaporate the solvent and form solidified polystyrene microrafts. The fluorescent microrafts were fabricated using a polystyrene solution containing 0.004% rhodamine-B (#02558, Sigma Aldrich, St. Louis, MO). The arrays were glued with PDMS to acrylic cassettes at 70°C for 3 h to form the completed unit that held culture media. Normalized bead area and bead distribution were calculated by segmenting the microrafts from transmitted light images and auto-fluorescent beads from the fluorescent images.

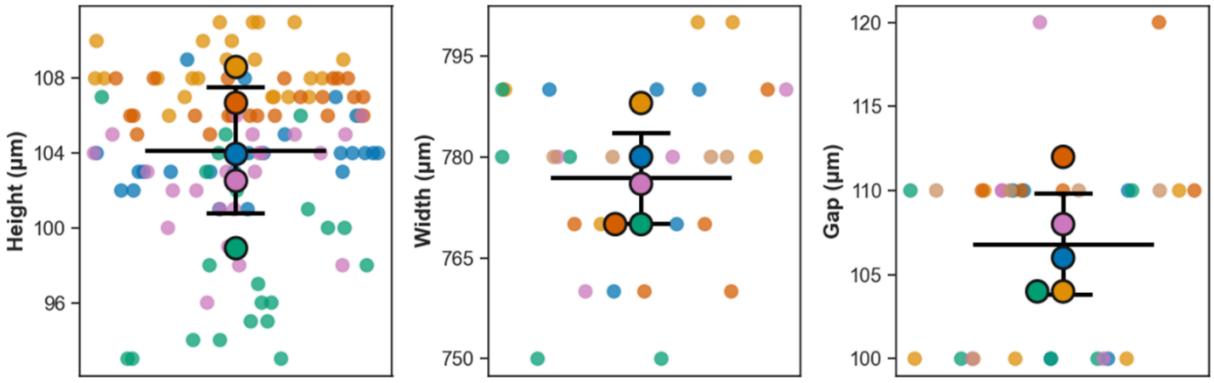

Fig. 3.2. Dimensions of master template features. Height and width of features and the gap width between features were measured via profilometry. Hues correspond to individual templates. Outlined circular data markers represent means, while smaller markers represent individual features. Mean crossbars and standard deviation error bars calculated from replicate-level means. N=5 templates, n_{height}=23 features, n_{width}=n_{gap}=5 features.

3.2.2. Microscopy Setup

Transmitted light and fluorescence images of each microraft array were mainly captured by the automated microscopy system described previously modified to accommodate the large microraft dimensions.[84] Briefly, the automated platform consisted of an inverted Olympus MVX10 MacroView fluorescence microscope (Evidence Scientific Inc., Waltham, MA), motorized H112A microscope stage (Prior Scientific Inc., Rockland, MA), and ORCA-Flash4.0 V.3 digital CMOS camera (Hamamatsu Corp., Bridgewater, NJ)—all controlled by custom MATLAB (MathWorks, Natick, MA) code with a Micro-Manager (Open Imaging, San Francisco, CA) core. The MVX10 microscope was equipped with a 2x wide-field

objective with a 0.25 numerical aperture (NA). Excitation light from a Lumen 200 mercury lamphouse (Prior Scientific Inc., Rockland, MA) was passed through an electronically controlled excitation LB10-NWIQ filter wheel with SmartShutter and an emission LB10-NWE filter wheel (Sutter Instrument, Novato, CA) arrayed with the 8900 – ET – Sedat Quad filter set (Chroma Technology Corp, Bellow Falls, VT). The automated microscopy system performed raster scans with overlaps between images of at least 900 µm (sum of the width of a single microraft and a single gap between microrafts). These images were acquired at 5x magnification, resulting in a pixel size of 1.3 µm per pixel. Additional images were captured on an inverted Fluoview 3000 (Evident Scientific Inc., Waltham, MA) equipped with 405, 488, 561, and 640 nm laser diodes and a TE2000-U inverted microscope (Nikon Instruments Inc., Melville, NY) outfitted with a Photometrics CoolSNAP HQ2 CCD camera (Teledyne Technologies, Thousand Oaks, CA).

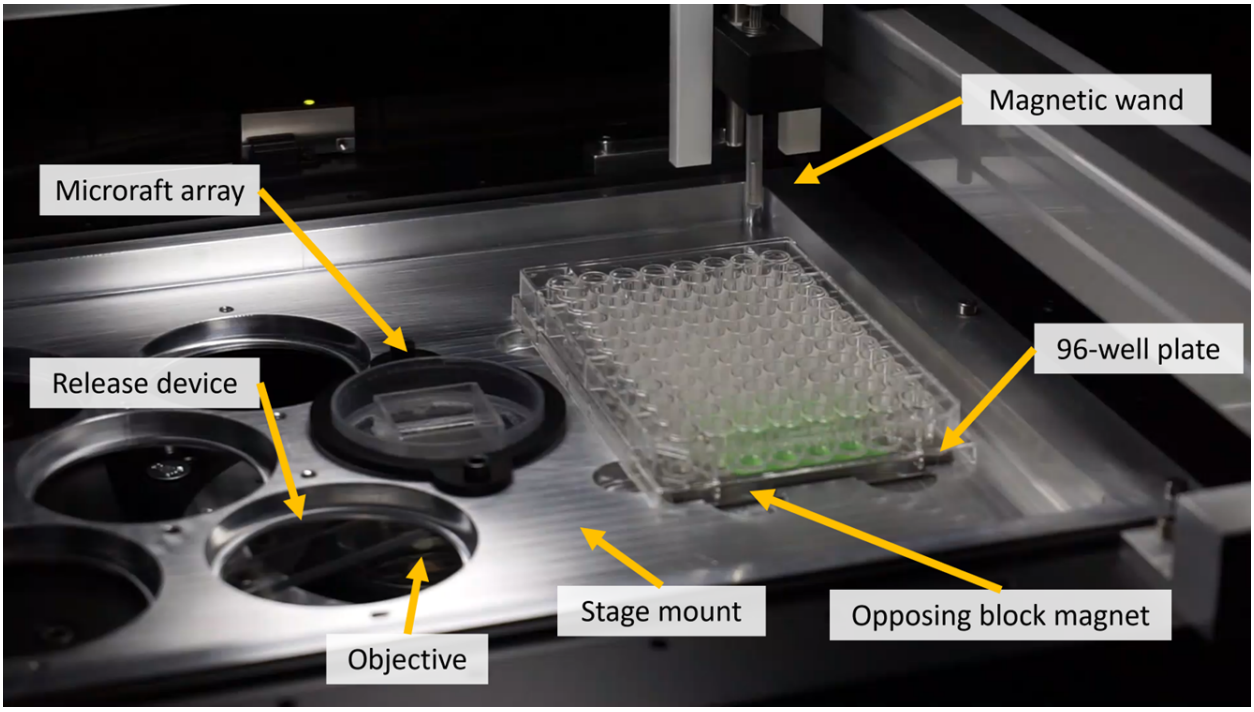

Fig. 3.3. Video of microraft release and collection. The target microraft was positioned via a motorized stage above the needle of the release device. Subsequently, the release device actuated continuously to eject the target microraft, which was collected by a magnetic wand controlled by a pick-and-place device. The target microraft was transferred and deposited in a 96-well plate as the magnet within the wand was repelled upward by an opposing block magnet under the 96-well plate. Surface tension of the collection media pulled the microraft off the magnetic wand. 800% video playback speed.

3.2.3. Microraft Isolation

Microrafts were isolated by the sorting system described previously [Fig. 3.3].[84] Individual microrafts were centered above and ejected by a microneedle—actuated by a release device mounted above the microscope objective—that pierced through the array backing. As the microrafts shifted within the surrounding microwells during the release step, an image-guided algorithm retargeted the release needle for consecutive actuations [Fig. 3.4 and Fig. 3.5]. Transmitted light images captured before and after each needle actuation until a maximum of 8 attempts were segmented to evaluate the proportion of the microraft remaining in the microwell [Fig. 3.4]. The PDMS array self-sealed after needle withdrawal, effectively containing the culture media. Subsequently, the 3-axis pick-and-place device, which was installed on the motorized microscope stage, positioned the magnetic wand directly over the released microraft for collection. Captured microrafts were deposited into an adjacent multi-well plate secured on the microscope stage as an opposing block magnet below the plate repelled the freely moving magnet within the wand.

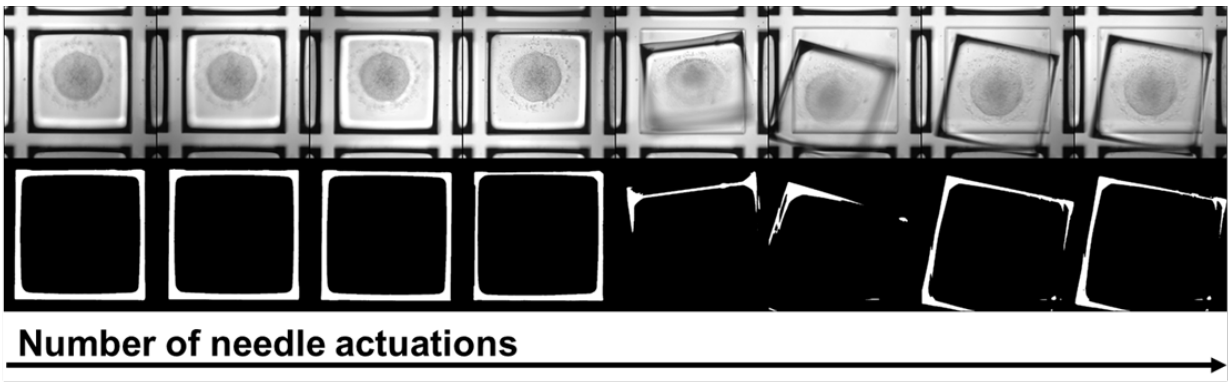

Fig. 3.4. Automated targeting and release of enlarged microrafts. Sequential transmitted light images (top row) and segmented masks (bottom row) of target microraft were generated after each needle actuation. The image-guided needle algorithm targeted the microraft corners (top left, top right, bottom right, and bottom left for the first four actuations) before the microraft center within the microwell for a maximum of 8 needle actuations per microraft.

3.2.4. Micropatterning via Deep UV

Multi-well plates and microraft arrays were plasma treated at 30W for 5 min and coated with a 0.1 mg/mL poly(l-lysin)100-grafted-poly(ethylene glycol)114-methoxy (PLL-g-PEG) (100 repeating units, 5000 Da, 20%; #11354, Nanosoft Polymers, Winston-Salem, NC) solution in phosphate buffer solution (PBS) (#46-013-CM, Corning Inc., Corning, NY) at 4°C overnight. Rinsed four times with deionized water, the substrates were air purged dry. A quartz photomask with circular openings was gently placed on top of a small volume of deionized water on the substrates, which were exposed to deep UV (254 nm) for 20 min via the HELIOS UV Ozone Cleaner (UVFAB, Walnut Creek, CA) to ablate circular regions in the PLL-g-PEG coating. The ablated substrates were rinsed four times with deionized water. Stored in PBS at 4°C to delay hydrophobicity recovery, the substrates were aspirated and immediately incubated in 1% Matrigel Matrix (#354234, Corning Inc., Corning, NY) diluted in Advanced Dulbecco's Modified Eagle Medium (DMEM)/F12 (#12634-010, Gibco, Waltham, MA) media supplemented with 0.1 mg/mL gentamicin sulfate (#30-005-CR, Corning Inc., Corning, NY) at 37°C for 1 h. The diluted Matrigel solution was stained with 947 nM Alexa Fluor 647 N-hydroxysuccinimide ester (NHS) ester (#16820, Lumiprobe, Hunter Valley, MD) at 4°C overnight before coating to visualize the patterning. The micropatterned substrates were washed five times with Advanced DMEM/F12 while ensuring the arrays remained covered in media to prevent drying out the Matrigel coating. Three more partial washes with PBS were performed for the NHS ester-stained Matrigel to reduce background signal from the array. Although a similar protocol had been developed on flat coverslips independently by Heemskerk et al.,[90] the process delineated here was tailored for the unique microraft array platform.

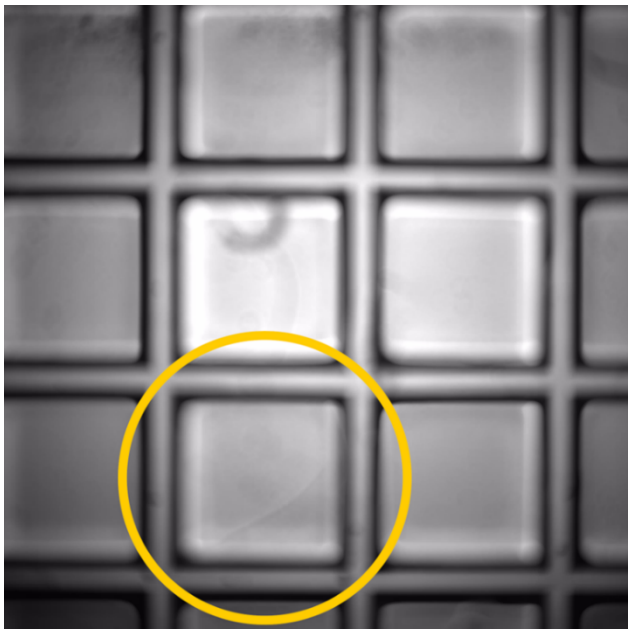

Fig. 3.5. Video of targeted needle release of single microraft. The target microraft (marked by the yellow circle) was repositioned above the needle (dark circular dot at the center of the deformation near the bottom of view that appears throughout video). The actuated needle contacts the microraft corners before the microraft center within the microwell. The release algorithm determined that this specific microraft was fully released from the microwell after the 7th needle actuation.

3.2.5. Cell Culture

RUES2 human pluripotent stem cells (hPSCs) (NIHhESC-09-0013) were routinely passaged using Accutase (#07920, STEMCELL Technologies, Vancouver, Canada) and grown in mTeSR Plus (#100-0276, STEMCELL Technologies, Vancouver, Canada) at 37°C and 5% CO2 on tissue culture-treated plates coated with 1% Matrigel. Reversine-treated cells were incubated in 0.5 μM reversine (#10004412, Cayman Chemicals Co., Ann Arbor, MI) in mTeSR Plus for 48 h with a medium change after 24 h.

3.2.6. Gastruloid Formation

Gastruloids were formed according to protocols adapted from those described previously [Fig. 3.6].[59] Pre-treated with 10 μM Rho-associated kinase (ROCK) inhibitor Y-27632 (#B1293, APExBIO Technology LLC, Houston, TX) at 37°C and 5% CO2 for 1 h, RUES2 cells were washed with PBS and incubated in Accutase at 37°C for 5 min. The suspended cell solution was washed with DMEM/F12 and centrifuged at 300 g for 4 min, after which the supernatant was discarded. Fresh mTeSR Plus supplemented with 10 μM Y-27632 was added to form a single-cell suspension. 1.8×10^6 cells were counted manually with a hemocytometer and seeded in mTeSR Plus with 10 μM Y-27632 onto each micropatterned microraft array. Following 2 h incubation at 37°C and 5% CO_2, the culture medium was replaced with mTeSR Plus containing 50 ng/mL bone morphogenetic protein 4 (BMP4) (#314-BP-010, R&D Systems, Minneapolis,

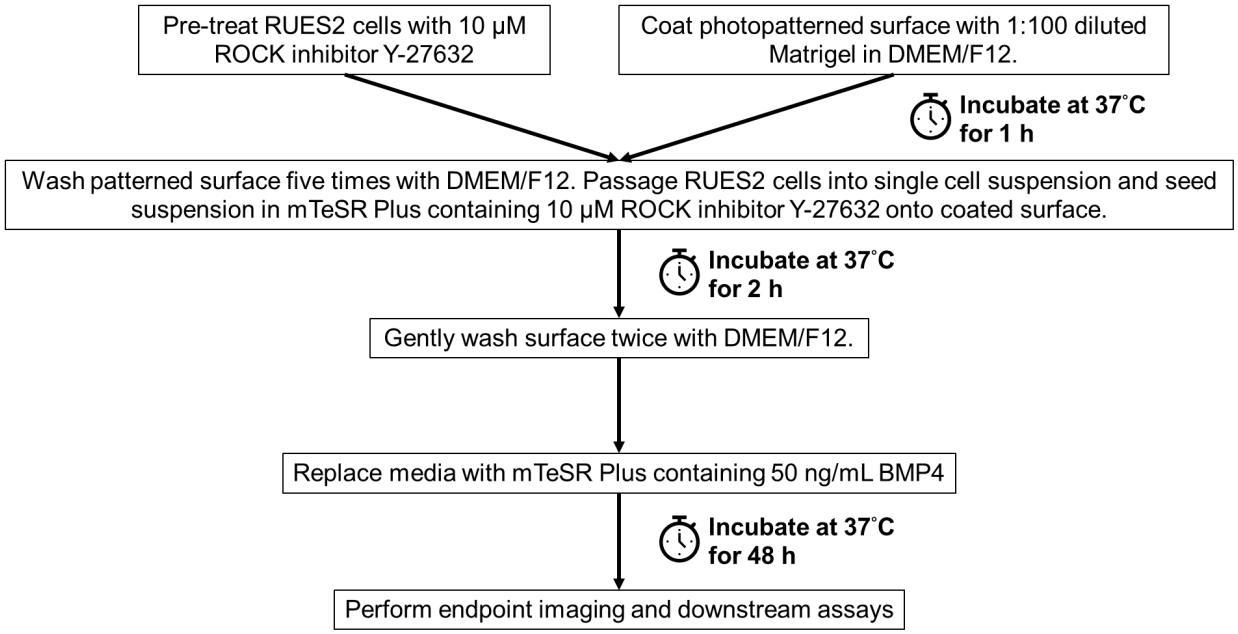

Fig. 3.6. Schematic of gastruloid formation.

MN) following two gentle rinses with DMEM/F12. The patterned cells were incubated at 37°C and 5% CO_2 for 48 h to induce gastruloid differentiation.

3.2.7. Immunofluorescence

For fixed confocal imaging, gastruloids were washed once with PBS, fixed in 4% paraformaldehyde (#P6148, Sigma-Aldrich, St. Louis, MO) at room temperature for 30 min, and washed three times with PBS. The samples were blocked and permeabilized in blocking solution [3% Normal Donkey Serum (NDS) (#017-000-121, Jackson ImmunoResearch, West Grove, PA) and 0.3% Triton-X (#93443, Sigma-Aldrich, St. Louis, MO) in PBS] at room temperature for 30 min. Incubated in primary antibodies (1:300 goat SOX2, R&D Systems, Minneapolis, MN; 1:300 rabbit BRA, R&D Systems, Minneapolis, MN; 1:300 GATA3, Invitrogen, Waltham, MA) diluted in blocking solution at room temperature for 2 h, the gastruloids were washed three times with washing solution (0.3% Triton-X in PBS). Secondary antibodies (1:1000 donkey, Invitrogen, Waltham, MA; anti-goat Alexa Fluor 555, anti-rabbit Alexa Fluor 488, anti-mouse Alexa Fluor 647) diluted in blocking solution were added at room temperature for 30 min before three washes with PBS. Samples were stained with 5 µg/mL DAPI (Invitrogen, Waltham, MA) for 30 min and washed three times with PBS.

For fixed imaging with the automated microraft system, gastruloids were rinsed twice with PBS, fixed in 4% paraformaldehyde at room temperature for 15 min, and rinsed three times with PBS. Incubated in glycine blocking solution [50 mM glycine (#G7126, Sigma-Aldrich, St. Louis, MO) diluted in 0.1% sodium azide (#S1002, Sigma-Aldrich, St. Louis, MO) in PBS] for 20 min, the fixed gastruloids were treated with permeabilization solution [0.5% Triton-X 100 (#X100, Sigma-Aldrich, St. Louis, MO) in PBS] for 20 min, washed twice with PBS, and blocked with 1% bovine serum

Imaging	Antibody	Reagent	Vendor	Catalog Number	Dilution/Concentration
Fixed (confocal)	Primary	SOX2 (Goat)	R&D Systems	AF2018	1:300
Fixed (confocal)	Primary	Brachyury (Rabbit)	R&D Systems	MAB20851	1:300
Fixed (confocal)	Primary	GATA3 (Mouse)	Invitrogen	MA1-028	1:300
Fixed (confocal)	Secondary	Donkey Anti-goat Alexa Fluor 555	Invitrogen	A21432	1:1000
Fixed (confocal)	Secondary	Donkey Anti-rabbit Alexa Fluor 488	Invitrogen	A21206	1:1000
Fixed (confocal)	Secondary	Donkey Anti-mouse Alexa Fluor 647	Invitrogen	A31571	1:1000
Fixed (confocal)	n/a	DAPI	Invitrogen	D1306	5 µg/mL
Fixed (microraft system)	Primary	SOX2 (Rabbit)	Cell Signaling	3579	1:200
Fixed (microraft system)	Primary	Brachyury (Goat)	R&D Systems	AF2085-SP	1:200
Fixed (microraft system)	Primary	CDX2 (Mouse)	Abcam	Ab157524	1:50
Fixed (microraft system)	Secondary	Donkey Anti-rabbit Alexa Fluor 488	Jackson ImmunoResearch	711-545-152	1:500
Fixed (microraft system)	Secondary	Donkey Anti-goat Alexa Fluor 555	Jackson ImmunoResearch	705-565-147	1:500
Fixed (microraft system)	Secondary	Donkey Anti-mouse Alexa Fluor 647	Jackson ImmunoResearch	715-605-150	1:500
Living, Fixed	n/a	Hoechst 33342	Invitrogen	H3570	10 µg/mL
Living	n/a	Calcein AM	Invitrogen	65-0853-39	1 µM

Table 3.1. Immunofluorescence staining reagents for gastruloids.

albumin (BSA) (#BP1600, Fisher Bioreagents, Waltham, MA) in wash solution [0.1% BSA, 0.2% Triton-X 100 and 0.05% Tween-20 (#P1379, Sigma-Aldrich, St. Louis, MO) in 0.05% PBS-azide] at room temperature for 1 h. The fixed cells were incubated with primary antibodies (1:200 rabbit SOX2, Cell Signaling, Danvers, MA; 1:200 goat BRA, R&D Systems, Minneapolis, MN; 1:50 CDX2, Abcam, Cambridge, United Kingdom) at 4°C overnight and rinsed with wash solution three times. Subsequently, the fixed cells were incubated with secondary antibodies (1:500 donkey, Jackson ImmunoResearch, West Grove, PA; anti-rabbit Alexa Fluor 488; anti-goat Alexa Fluor 555; anti-mouse Alexa Fluor 647) at room temperature for 1 h before three washes with PBS. Samples were stained with 5 μg/mL Hoechst 33342 for 15 min and washed three times with PBS.

For live imaging, gastruloids were stained with 10 μg/mL Hoechst 33342 (Invitrogen, Waltham, MA) at 37°C for 2 h and 1 μM calcein AM (Invitrogen, Waltham, MA) at 37°C for 30 min in the same differentiation media containing BMP4. Three washes with PBS were performed before mTeSR Plus containing 10% fetal bovine serum (FBS) (#10438026, Gibco, Waltham, MA) was added for microraft isolation.

Staining reagents used are listed in Table 3.1.

3.2.8. Automated Image Processing and Analysis of Fixed Gastruloids

Images of the fixed gastruloids (stained with Hoechst 33342 and antibodies for CDX2, BRA, and SOX2) captured by automated microscopy system were analyzed using automated pipelines in both MATLAB (MathWorks, Natick, MA; ver. 9.5.0.1586782 (R2018b) Update 8) and Python (ver. 3.12.3). The transmitted light images were processed in parallel in MATLAB during the scan to locate and index individual microrafts after flat-field correction, Otsu's thresholding, and morphological filtering.[91] After the scans, a separate pipeline in Python i) stitched composite images of the entire array from the section images and ii) cropped images of each microraft for gastruloid segmentation. Composite images of the arrays were stitched from flat-field corrected images of the array sections using the stage coordinates for each image. Flat-fields were approximated by Gaussian filtering the images with a sigma value of 30. The Python pipeline defined the region-of-interest (ROI) for each gastruloid before extracting features [Fig. 3.7]. The image of the Hoechst 33342 stain of each gastruloid was segmented by a static manual threshold to create

a binary mask. Morphological closing with a 5-pixel radius disk was performed, objects smaller than 25000 square pixels were removed, and the convex hull of the resulting mask was generated. The final ROI mask was used to assess whether the microraft contained a centered gastruloid. Microrafts without a gastruloid, containing a gastruloid with low stain signal below a minimum value, or containing a gastruloid contacting the microraft edge were excluded from further analysis [Fig. 3.8]. Images for the BRA and CDX2 stains were background subtracted via the rolling ball algorithm with a 50-pixel radius and Gaussian filtered with a sigma value of 2. All the fluorescence images were segmented by Otsu's thresholding before the ROI mask was applied to remove segmented cells outside of the gastruloid.[91] Fluorescence area, eccentricity, and radius (averaged from the lengths of the major and minor axes) were measured from the final processed mask for each stain. The ratio of the fluorescence area of each mask across all fluorescence channels to the ROI area was calculated for each gastruloid.

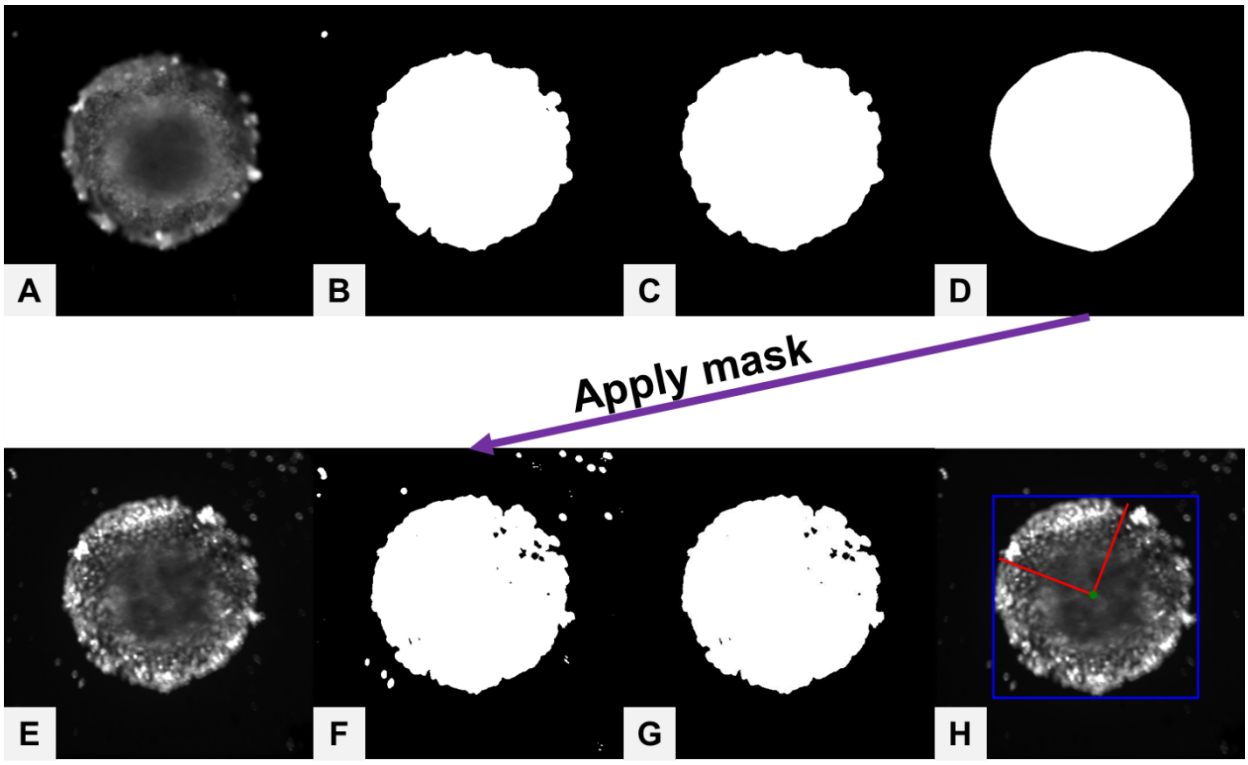

Fig. 3.7. Gastruloid analysis on microrafts. (a) For each gastruloid, the computational pipeline performed (b) segmentation, (c) morphological closing, and size-based filtering before (d) determining the convex hull to produce the final ROI mask. Subsequently, (e) all fluorescence images were (f) segmented and processed via morphological filters. (g) The ROI mask was applied to each resulting mask to eliminate cells or debris outside the gastruloid border. (h) The processed mask for each fluorescence image was measured for features including the fluorescence area, fluorescence area normalized to the ROI area, eccentricity, and radii.

3.2.9. Automated Image Processing and Analysis of Living Gastruloids

Images of the living gastruloids (stained with calcein and Hoechst 33342) were processed in a similar manner to their fixed counterparts with the following exceptions. The images of the calcein stain were segmented by Li's thresholding to define the ROI mask, while those of the Hoechst 33342 stain were segmented by a static manual threshold.[92] The Python pipeline measured the fluorescence area, eccentricity, and radius of the ROI mask and the fluorescence area of the mask corresponding to the Hoechst 33342 stain. The fluorescence area of the mask from the Hoechst 33342 stain was normalized to the ROI area to determine the normalized Hoechst 33342 area (normalized DNA content) within each gastruloid. Detecting living gastruloid location on arrays was characterized by 99.4±0.4% sensitivity and 100±0% specificity (N=12 arrays) when using manual inspection as the "gold standard."

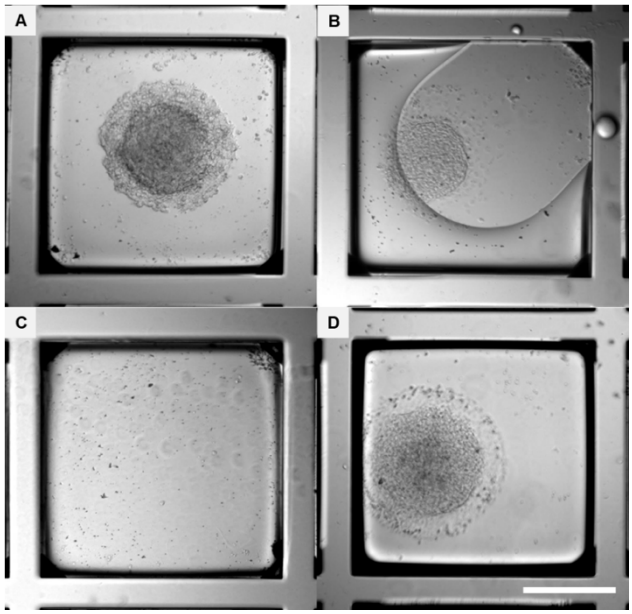

Fig. 3.8. Classifying quality of gastruloid placement. Transmitted light images of a (a) microraft with centered gastruloid, (b) missing or malformed microraft, (c) microraft without gastruloid, and (d) microraft with gastruloid contacting microraft border. Scale bar, 300 μm.

3.2.10. RT-qPCR

Properly aligned and developed gastruloids were randomly selected for isolation based on their measured normalized DNA content and human visual inspection of the corresponding fluorescence images. Ejected microrafts were collected into individual wells of a non-binding 96-well plate (#655901, Greiner Bio-One, Monroe, NC) for RNA isolation using the Taqman Cells-to-CT Express Kit (#A57985, Invitrogen, Waltham, MA). The manufacturer's protocol was followed, except the collection plate containing the Express Lysis Solution was placed on an orbital shaker at room temperature for 30 min. cDNA synthesis was performed using a mini16 thermal cycler (miniPCR bio, Cambridge, MA). Expression of glyceraldehyde-3-phosphate dehydrogenase (GAPDH), noggin (NOG), and keratin 7 (KRT7) were quantified by TaqMan Gene Expression Assays (#4331182, Applied Biosystems, Waltham, MA): GAPDH

(HS109999905_m1), NOG (Hs00271352_s1), and KRT7 (Hs00559840_m1). Each PCR reaction was prepared in a final volume of 20 µL on a QuantStudio 5 Real-Time PCR System (Applied Biosystems, Waltham, MA) set on the fast mode with the following thermocycling protocol: 50°C for 2 min to activate uracil-N glycosylase and 95°C for 20 sec to activate the AmpliTaq Fast DNA Polymerase followed by 40 cycles of denaturation at 95°C for 1 sec and annealing/extension at 60°C for 20 sec. Reactions for NOG and KRT7 were performed in duplicates, while reactions for GAPDH were conducted in quadruplicates. No-template controls for all assays were included. Data was analyzed via the QuantStudio 5 Design and Analysis software (Applied Biosystems, Waltham, MA) and Microsoft Excel (Microsoft Corporation, Redmond, WA).

3.2.11. Statistics

Measurements are reported as the means with one standard deviation unless otherwise noted. Python and Microsoft Excel were used for the statistical analyses. SuperPlots were generated by pooling means of technical replicates followed by an unpaired, two-tailed t-test to determine statistical significance.[93] The Pearson's correlation coefficient was calculated to assess the correlation between relative mRNA expression levels and normalized DNA content. For statistical comparisons, p-values are represented by the following: n.s. (not significant) for $p>0.05$, * for $p\leq0.05$, ** for $p<0.01$, and *** for $p<0.001$.

3.3. Results and Discussion

3.3.1. Design Overview and Specification

The microraft array technology was developed for the screening and sorting of 2D gastruloids. Large near-millimeter-sized square microrafts with low concavity in the center were required for consistent photopatterning of 500 µm-diameter circular patches of basement matrix across the entire array. The circular ECM patches must be surrounded by a surface coating that deters cell adhesion such that cells would be geometrically confined within the islands of ECM. Notably, the microrafts were designed with 800 µm side dimensions to ensure distancing of the ECM patches from the microraft edges so that the diffusion of signaling molecules from the gastruloid edges (required for self-patterning) would not be disrupted.[36,54] For image-based screening, the microrafts must be optically clear yet sufficiently paramagnetic to enable

collection and transfer with a magnetic wand once released. The microrafts should dislodge consistently from the PDMS mold during release without damage to either the microraft itself or the cell cargo when using the needle-based microraft ejection. Importantly, both the accuracy of the microraft releases and collections were prioritized so that individual gastruloids displaying different phenotypes could be compared without the loss of gastruloids. Additionally, any form of automation was desired to minimize the time and labor of manual collection and to support systematic isolation of many individual colonies. The above requirements necessitated key innovations to the microraft array platform including greatly enlarged microraft dimensions, novel micropatterning protocols, and automated microraft sorting enhancements to support the screening and sorting of high-quality gastruloids.

3.3.2. Fabrication and Patterning of Large-Sized Microrafts

To fabricate the very large-sized microrafts, a modified fabrication process was employed with optimization of the different steps including the photolithographic steps forming the mold, magnetic bead placement via surface tension forces at the corners of the microwells, and dip coating to form the final magnetic microrafts [Fig. 3.9(a), Fig. 3.9(b), and Fig. 3.1].[62] The consistency of the microraft arrays at both the middle regions (central 19 x 19 grid within 23 x 23 array) and periphery (first two rows from each array edge) were evaluated by imaging microrafts containing 0.004% rhodamine-B [Fig. 3.9(c) and Fig. 3.10]. The average dimensions of the microrafts were 789±2 μm; however, there was more variability in the microraft size at the peripheral array (789±4 μm) than at the middle array (789±1 μm) (N=3 arrays, n=5 microrafts at each array location) [Fig. 3.9(d)]. The thicknesses of the microraft center (36±2 μm) and edges (106.4±0.6 μm) were also uniform across the array (N=3 arrays, n=5 microrafts at each array location) [Fig. 3.9(e)]. Importantly, the microrafts across the entire array were flat for most of their top surface, as the average length of the flat surface normalized to the entire microraft side length was 0.9±0.0 (N=3 arrays, n=5 microrafts at each array location) [Fig. 3.9(f)]. The distribution of the magnetic beads within the microrafts was also assessed [Fig. 3.9(g)]. For unobstructed imaging of the gastruloids, the beads must be absent from the microraft center. All beads were located within 15 μm from the microraft edge (<2% of the microraft edge length) and occupied less than 3% of the microraft area on all microrafts (100±0%, N=3 arrays, n_{middle}=8 microrafts, $n_{peripheral}$=6 microrafts) [Fig. 3.9(h) and Fig. 3.11]. Even though the fabrication

process was originally designed for micron-level structures, these metrics indicated the near-millimeter-sized, flat microrafts were uniform in both dimensions and bead distribution throughout the entire array.

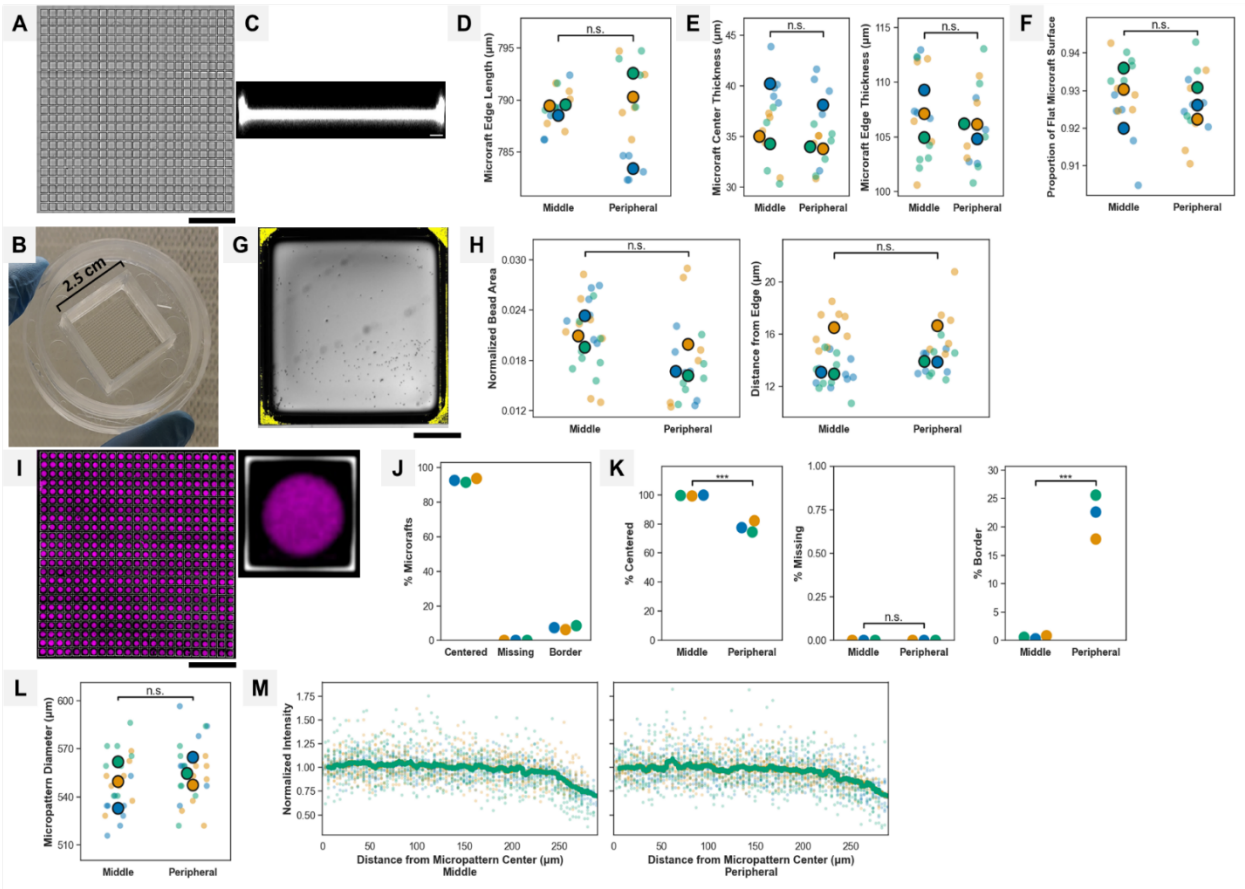

Fig. 3.9. Fabrication and patterning of large-sized microrafts. (a) Stitched composite transmitted light image of an empty microraft array with 529 total microrafts in a 23 x 23 grid. Scale bar, 5 mm. (b) Photograph of a fully assembled microraft array and cassette. (c) Confocal microscopy X-Z image of a microraft with 0.004% rhodamine-B. Scale bar, 50 μm. (d) Mean edge lengths (calculated from all four edges) of microrafts located at the middle and peripheral array. p=0.8. (e) Mean thickness or the Z depth for the central region of microrafts at the middle or peripheral array (left panel, $p_{\text{microraft central region}}$=0.6). Mean thickness of the Z depth for the outer region of microrafts located at the middle and peripheral array (right panel, $p_{\text{microraft outer region}}$=0.4). (f) Length of flat portion of microraft normalized to total length of microraft. p=1.0. For panels (d-f), N=3 arrays, n=5 microrafts at each array location, t-tests from replicate-level means. (g) Overlaid fluorescence and transmitted light image of a single microraft with superparamagnetic beads (yellow) located near the microraft edges. Scale bar, 200 μm. (h) Bead area normalized to the microraft area (left panel) and mean distance (right panel) of beads from the closest microraft edge. N=3 arrays, n_{middle}=8 microrafts, $n_{\text{peripheral}}$=6 microrafts, $p_{\text{bead area}}$=0.08 and $p_{\text{distance-from-edge}}$=0.07 when comparing measurements at the middle and peripheral array, t-tests from replicate-level means. (i) Stitched composite confocal image (maximum projection) of Alexa Fluor 647 NHS ester-stained micropatterned Matrigel on an array of microrafts containing 0.004% rhodamine-B. Magnified view of a single microraft next to composite. Scale bar, 5 mm. (j) Matrigel micropattern quality on microraft arrays (centered, missing, or contacting border). Percent of microrafts calculated by dividing by the total number of microrafts (529 microrafts) per array. N=3 arrays. (k) Matrigel micropattern quality on microrafts at the middle and peripheral array. Percentage of

microrafts calculated by dividing by number of microrafts at middle array (361 microrafts) and edge (168 microrafts). No micropatterns were missing across all arrays. N=3 arrays, $p_{centered}$=0.2 and p_{border}=0.2 when comparing percentage of microrafts at the middle and peripheral array, t-tests. (l) Micropattern diameter on microrafts at the middle and peripheral array. N=3 arrays, n=8 microrafts at each array location, p=0.3, t-tests from replicate-level means. (m) Relative intensity (normalized to the mean intensity within 10 μm from the micropattern center) of AF647-stained Matrigel from the micropattern center. Rolling average (50 sliding window size) displayed. N=3 arrays, n=8 microrafts at each array location. (d-f, h, j-m) Peripheral microrafts located within two rows from each array edge, while middle microrafts located within central 19 x 19 grid within the array. (d-f, j-m) Hues correspond to individual arrays. (d-f, h, l) Outlined circular data markers represent means, while smaller markers represent individual microrafts. (d-f, h, k-l) n.s. indicates no statistical difference.

To produce consistent gastruloids across the entire array, a photopatterning approach was developed using deep UV light to form circular Matrigel islands surrounded by poly(L-lysine)-graft-poly(ethylene glycol) (PLL-g-PEG) on each microraft [Fig. 3.9(i) and Fig. 3.12]. The microraft arrays were first coated throughout with PLL-g-PEG and then a circular region of the PLL-g-PEG on each microraft was ablated by exposure to UV light through a photomask. Deformations of a few microns within the elastomeric PDMS microarray, even with tensioning introduced during the fabrication process to deter deformation,[94] can present a challenge when aligning the photomask on an array of 529 microrafts. Thus, photomasks were designed with varying distances between the circular openings based on measurements from multiple arrays. Subsequently, the array was incubated with Matrigel to backfill the circular regions with Matrigel. Since the PDMS backing of the arrays was flexible, the arrays were placed on a temporary glass slide during the surface patterning process. The PEG side chains of the polymer coating deterred cell attachment while the Matrigel promoted cell adherence. All microrafts were patterned with Matrigel regions [Fig. 3.9(j)]. This ECM (Matrigel) was properly centered on 92.6±0.9% of the microrafts, while 7.4±0.9% of the microrafts possessed misaligned patterns (N=3 arrays) [Fig. 3.9(j)]. Moreover, patterns were significantly better aligned in the middle array (99.4±0.2% of microrafts in the array middle) than the peripheral array (78±3% of peripheral microrafts) (N=3 arrays, p=0.2) [Fig. 3.9(k)]. The consistency and evenness of the patterns across the array were assessed. The average diameter of

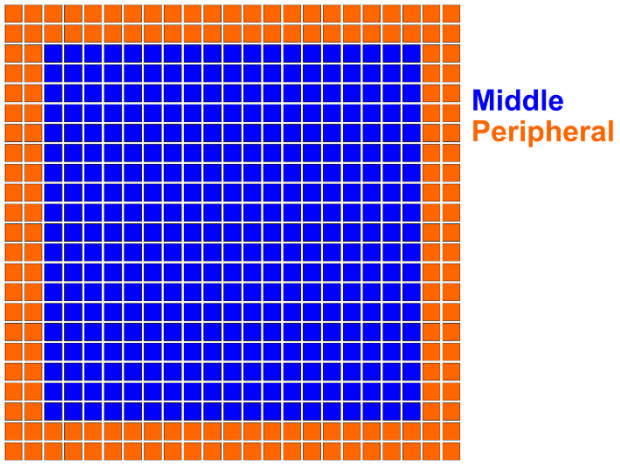

Fig. 3.10. Schematic of middle and peripheral regions of array. Each array contains 529 total microrafts: 361 middle and 168 peripheral microrafts.

the micropatterned ECM was 552±5μm and uniform across the array (N=3 arrays, n=8 microrafts at each array location) [Fig. 3.9(l)]. The normalized intensity of fluorophore-labeled Matrigel patches across the diameter of the micropatterns was similar from the middle to peripheral portions of the array. Though on average at 240 μm and 265 μm from the Matrigel patch center, the fluorescence was decreased by 10% and 20%, respectively (N=3 arrays, n=8 microrafts at each array location) [Fig. 3.9(m)]. Overall, the microraft arrays were properly patterned with ECM islands within the PLL-g-PEG coating, both of which are essential for gastruloid formation.

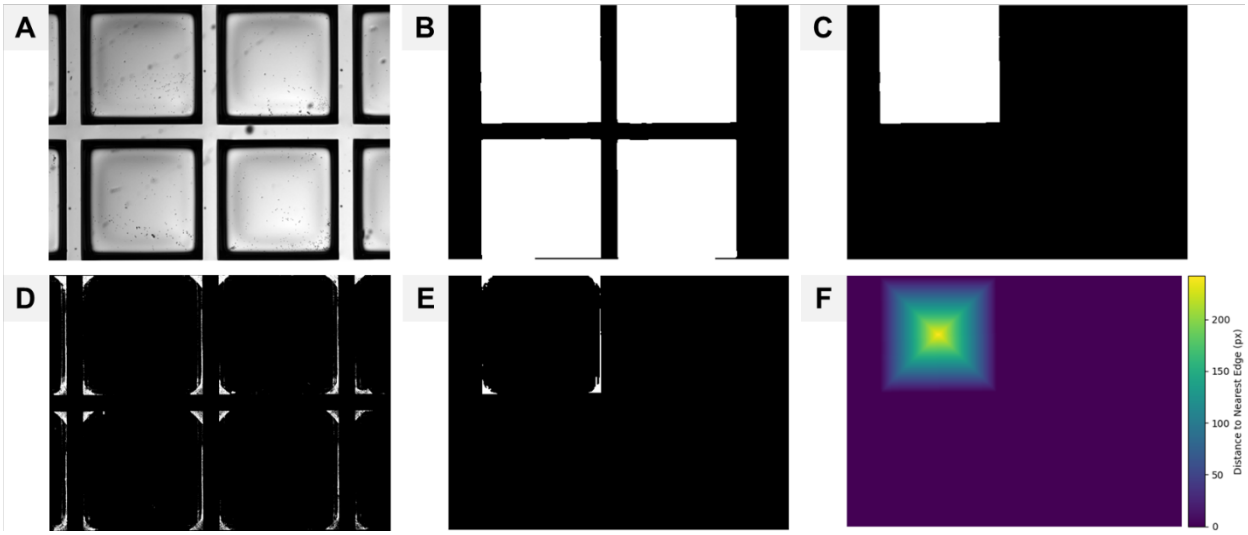

Fig. 3.11. Normalized bead area and distribution analysis. Otsu's thresholding was applied to (a) transmitted light images of the arrays to produce (b) binary masks, from which (c) individual microrafts were segmented. Manual thresholding was applied to the fluorescence images of the magnetic beads to create (d) binary masks. Subsequently, the individual microraft masks were (e) applied to the masks of the beads and (f) used to generate a distance gradient map to determine the distance of each pixel (which was above the empirically set threshold) to the nearest microraft edge. The fluorescent area of the beads was divided by the total area of the segmented microraft to determine the normalized bead area, while the mean distance to the closest edge was calculated for each bead pixel.

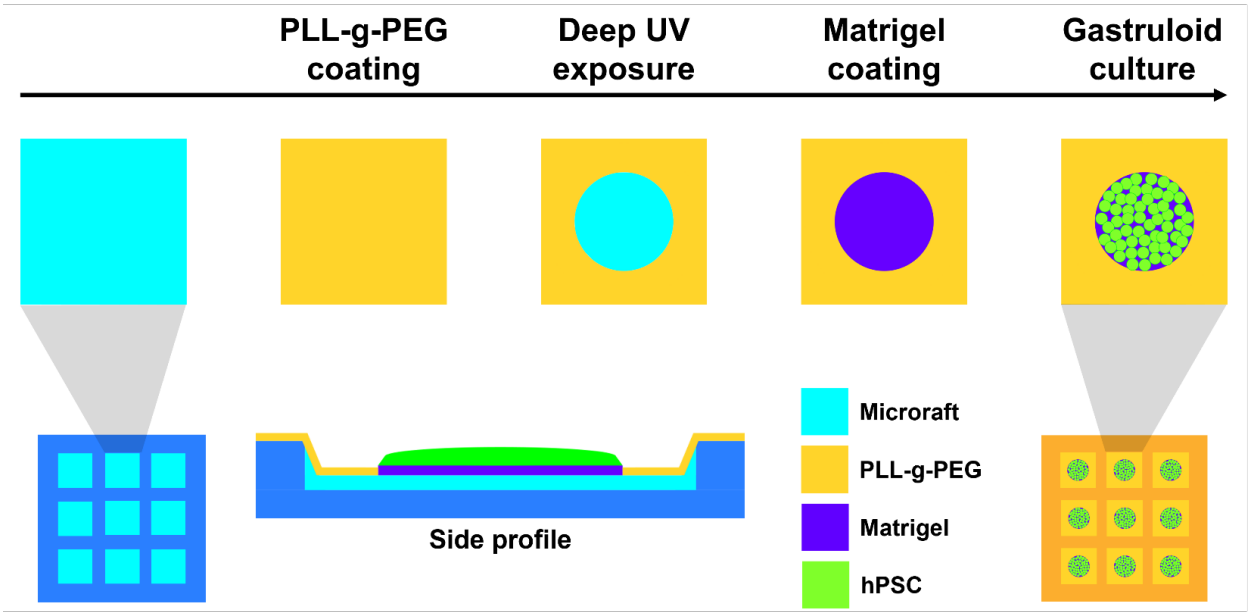

Fig. 3.12. Schematic of photopatterning. The upper row depicts the surface of a single microraft. The lower row displays: a top view of a 3 x 3 microraft section of an array, a side view of a single microraft after final patterning, and a legend.

3.3.3. Formation of Gastruloids on Microrafts

Gastruloids were formed by dissociating RUES2 hPSCs and plating them on a Matrigel-patterned surface on a polystyrene plate (control growth substrate) or the surface-patterned microrafts [Fig. 3.13 and Fig. 3.6]. After cells reached confluence on the circular Matrigel patterns, BMP4 was added to initiate gastruloid formation. Over a 48-h time, cells on both the polystyrene plate and microrafts developed a dark central zone by transmitted light microscopy, a feature characteristic of a mature, self-organized gastruloid [Fig. 3.13(a)]. At 48 h, the gastruloids were fixed and immunostained for GATA3, Brachyury (BRA), and SOX2 representing the trophectoderm, mesoderm, and ectoderm, respectively [Fig. 3.13(c) and Fig. 3.14]. The presence of the cell lineages was assessed following fixation and staining of the gastruloids. Although the detailed morphology of the cell types varied among the gastruloids, all the gastruloids (100±0%) displayed the three cell lineages with clear segregation between the lineages (N=3 replicates of each substrate type, n=16 gastruloids per array). Thus, the gastruloids similarly developed on both the control polystyrene plate and microrafts.

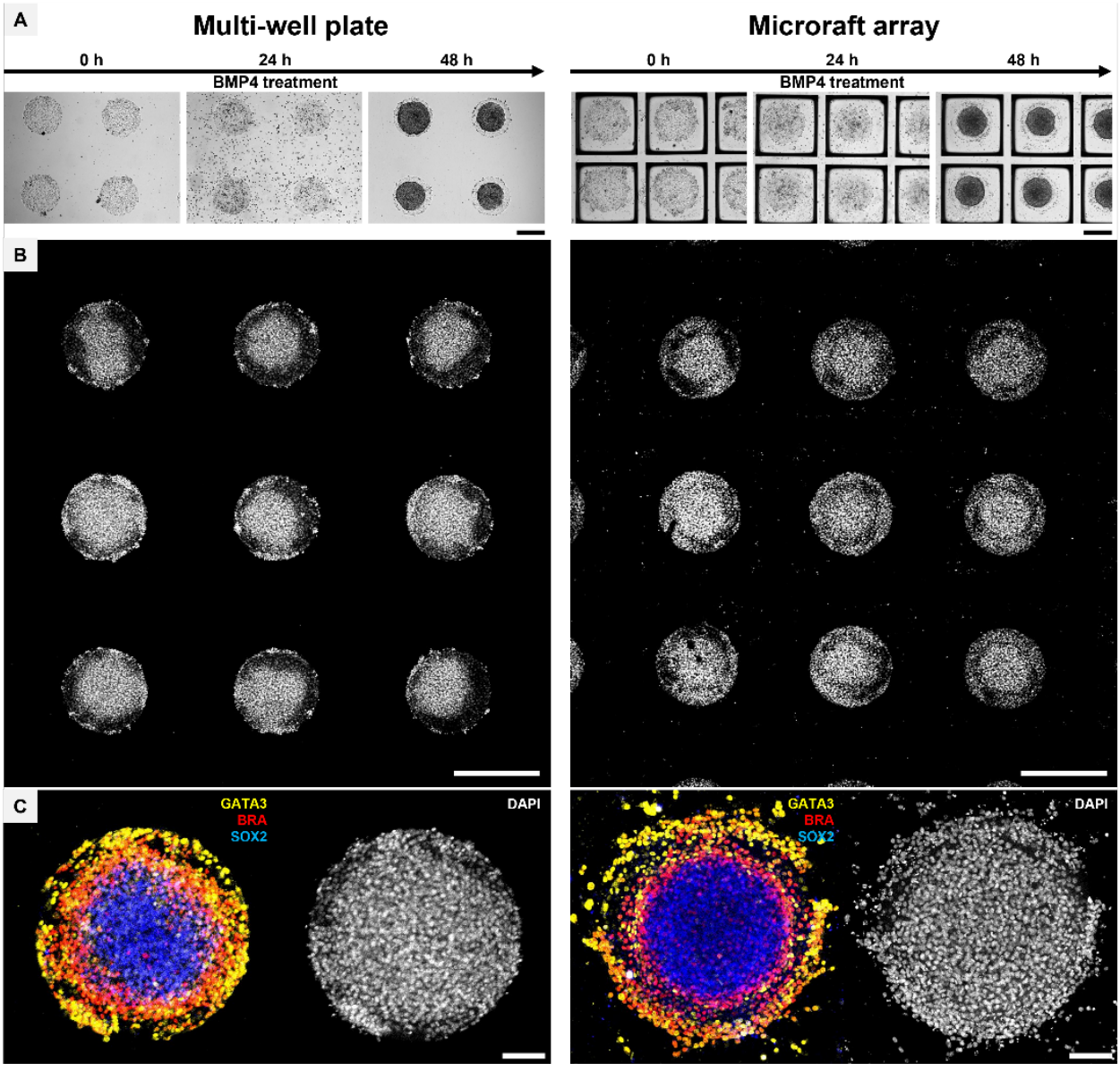

Fig. 3.13. Gastruloids on microrafts are comparable to those on polystyrene multi-well plates. (a) Transmitted light image time-series of 4 micropatterned gastruloids on a polystyrene multi-well plate or microraft array. Scale bars, 400 μm. (b) Confocal fluorescence images (maximum projection) of 9 DAPI-labeled gastruloids. Scale bars, 500 μm. (c) Overlaid confocal fluorescence images (maximum projection) of a single gastruloid immunostained for GATA3, Brachyury (BRA), and SOX2 (representing the trophectoderm, mesoderm, and ectoderm, respectively) and the corresponding confocal fluorescence image of the gastruloids DAPI-labeled. Scale bars, 100 μm.

3.3.4. Automated Imaging

To enable large-scale screens of gastruloids, automated imaging and image analysis are crucial to measure features from many hundreds of gastruloids in a single experiment. Importantly, large sample sizes provided by the microraft array greatly enhance the robustness of statistical analyses. The microraft

system was controlled by a custom MATLAB program and graphical user interface (GUI) to scan the arrays of stained gastruloids followed by segmenting and indexing each existing microraft.[84,87] Each gastruloid was imaged at a spatial resolution of 1.3 μm/pixel. Subsequently, a standalone computational pipeline in Python processed the gastruloid images by defining a region-of-interest (ROI) (to omit cell debris or cells outside of the centered gastruloids) and measuring features of fluorescence stains [Fig. 3.7]. Notably, the pipeline was tailored to grading and extracting features from the gastruloids on the indexed microrafts. The ROI was also used to assess the presence (a single adequately sized object should be present following the segmentation process) and centering (whether the ROI contacts any microraft edge) of the gastruloid on each microraft (see "3.2. Methods"). 85±16% of microrafts across the entire array displayed properly aligned ("centered") gastruloid placement (N=15 arrays) [Fig. 3.15(a) and Fig. 3.8]. Microrafts that were missing from the array ("missing," 0.4±0.5%), without gastruloids ("empty," 3±4%), or had gastruloids contacting the microraft edges ("border," 12±20%) were computationally excluded from further analysis (N=15 arrays) [Fig. 3.15(a) and Fig. 3.8]. Excluded microrafts were not disproportionately located at either the middle or peripheral array (N=15 arrays) [Fig. 3.15(b)]. The diffusion of signaling molecules from the edge of the colony is required for self-organization in gastruloids; therefore, the gastruloid must have ample space between the edges of the colony and microwell wall surrounding the microraft.[36,54] When compared to manual identification, the imaging pipeline determined gastruloid placement on the fixed arrays with 100±0% sensitivity and 99.7±0.2% specificity, where true positives were centered gastruloids and true negatives were excluded misplaced gastruloids (N=3 arrays). Notably, the image analysis pipeline not only accurately but also systematically screened all 529 gastruloids on each microraft array.

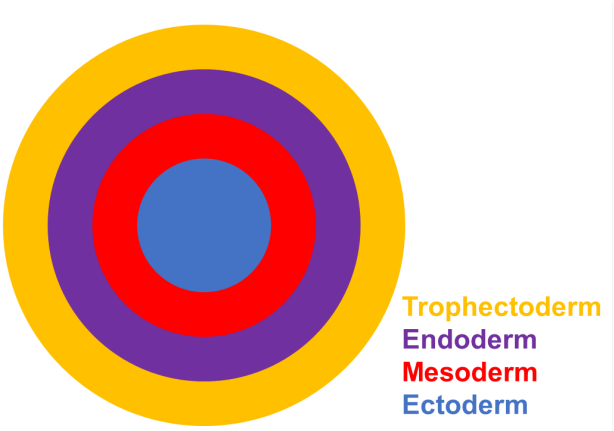

Fig. 3.14. Schematic of fully developed gastruloid.

3.3.5. Systematic Imaging and Analysis of Fixed Gastruloids

Fixed gastruloids were stained with Hoechst 33342 to label DNA while immunostaining was performed for SOX2, BRA, and CDX2 marking the ectoderm, mesoderm, and trophectoderm, respectively [Fig. 3.16(a)]. Both GATA3 and CDX2 are equivalent markers of trophectoderm-like cells,[88] while both DAPI and Hoechst 33342 stain DNA. Subsequently, the entire array was imaged by the automated microraft system, requiring on average 16.59±0.04 min across all 5 channels per array (transmitted light and 4 immunofluorescence stains) (N=3 arrays). Each gastruloid image was processed by the computational pipeline, which measured features of each fluorescent stain including total fluorescence area, fluorescence area normalized to the ROI area, eccentricity, and radius [Fig. 3.16(b)]. The mean radius of fixed (251±4 μm) gastruloids was smaller than that of the Matrigel micropatterns (276±2 μm) (N_{fixed}=3 arrays, $N_{pattern}$=3 arrays). Instead, the mean gastruloid radius matched more closely with the distance from the center of the micropatterns by which the relative intensity of the stained Matrigel decreased by 10-20% (between 240-265 μm). This suggests the effective radius of the micropatterns for cell adhesion was smaller than the total radius. Although the means for each feature are similar, the individual data points revealed variability even

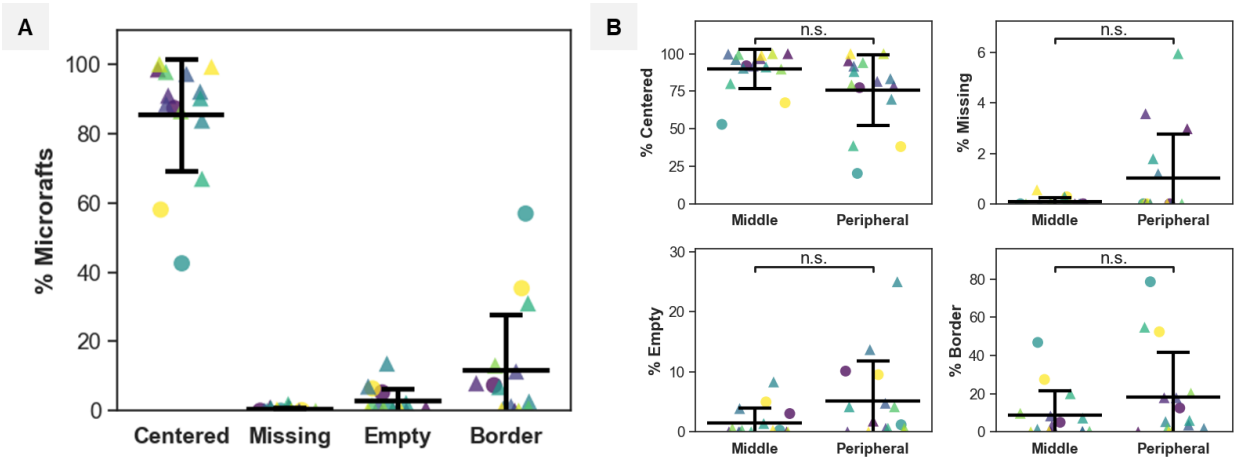

Fig. 3.15. Automated assessment of gastruloid placement on microrafts. (a) Gastruloid micropatterning quality on microraft arrays (raft with centered gastruloid, missing microraft, empty microraft without a gastruloid, or microraft containing gastruloid contacting border). Percentage of microrafts calculated by dividing by the total number of microrafts (529 microrafts) per array. (b) Gastruloid micropatterning quality on microrafts at the middle (central 19 x 19 grid within array) and peripheral (first two rows from each array edge) array. Percentage of microrafts calculated by dividing by the number of microrafts at the middle (361 microrafts) or peripheral (168 microrafts) array. $p_{centered}$=0.06, $p_{missing}$=0.05, p_{empty}=0.07, and p_{border}=0.2 when comparing the percentage of microrafts at the middle and peripheral array, t-tests. (a-b) Hues correspond to individual arrays. Mean crossbars and standard deviation error bars displayed. Circles and triangles represent fixed and living arrays, respectively. N_{fixed}=3 arrays, N_{living}=12 arrays. n.s. indicates no statistical difference.

within the same array [Fig. 3.16(b)]. These features form a basic subset demonstrating the power of this platform for future quantitative studies.

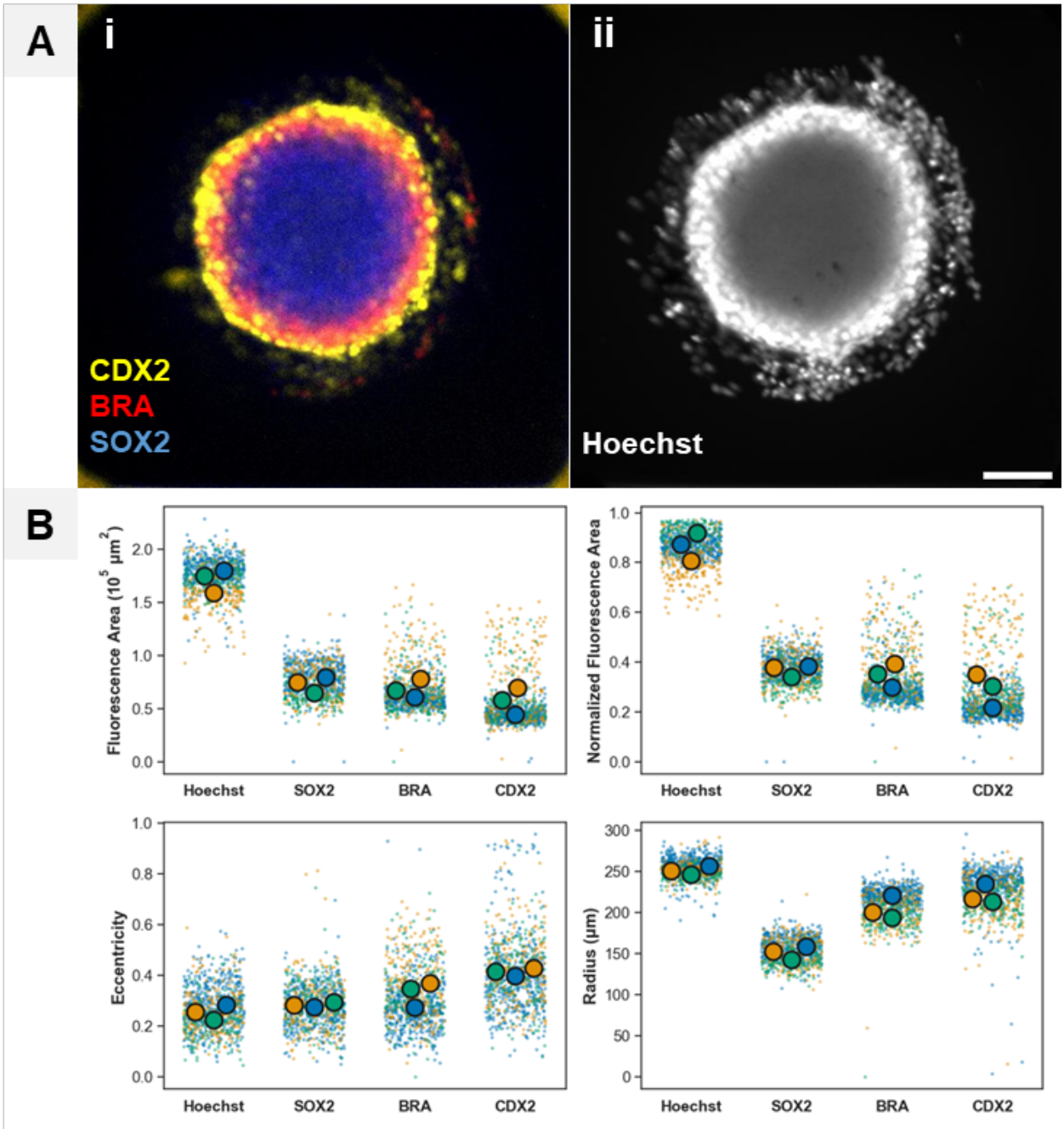

Fig. 3.16. Systematic imaging and analysis of immunostained gastruloids. (a) Widefield microscopy images of a fixed gastruloid displaying i) merged CDX2, BRA, and SOX2 immunostaining to mark the trophectoderm, mesoderm, and ectoderm, respectively, and ii) Hoechst 33342 staining. Scale bar, 100 µm. (b) Germ layer features (fluorescence area, fluorescence area of staining mask normalized to area of ROI mask, eccentricity, and radius) of euploid gastruloids fixed in 4% paraformaldehyde (PFA) following 48 h BMP4 treatment. N=3 arrays (n≥159 microrafts each). Only microrafts containing centered gastruloids with adequate immunostaining were analyzed. Hues correspond to individual arrays. Outlined circular data markers represent means, while smaller markers represent individual micropatterns.

3.3.6. Microraft Release and Collection

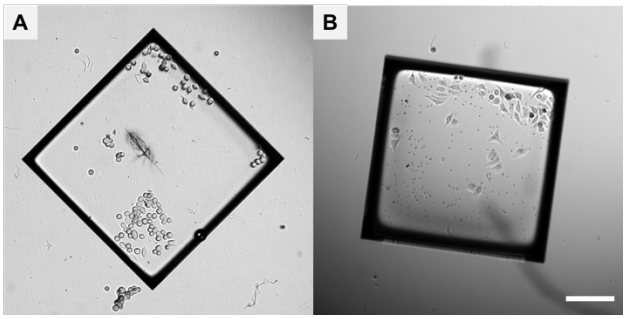

Fig. 3.17. Thicker microrafts resist cracking. Transmitted light images of a (a) thinner (60 μm edge thickness) and (b) thicker (100 μm edge thickness) iteration of the large-sized microrafts following isolation. Scale bar, 300 μm.

For downstream assay performance, the large-scale microrafts must be individually releasable and collectable in an automated manner. Release and collection were performed as described previously with modifications to accommodate the challenges incurred by the low-aspect ratio, large-sized microrafts [Fig. 3.3].[84] The major challenges presented by the large-sized microrafts were cracking of the polystyrene matrix upon contact with the needle, failure of release from within the surrounding PDMS microwell, and a failure to capture the large microraft by the magnetic collection wand. Fracturing of the microraft was eliminated by increasing the microraft thickness from 60 to 100 μm edge thickness with 0% (n>100 microrafts) of the thicker microrafts cracking [Fig. 3.17]. The automated microraft release system was originally designed for small microrafts with sides measuring 100 μm with a much higher aspect ratio than the gastruloid microrafts.[84] Although the smaller microrafts were released with high efficiency by a needle impact located at the microraft center, the large microrafts (789 x 789 μm) when impacted at only their centers were freed from their PDMS microwells <80% of the time. The microrafts that were not released often appeared to be attached to the array by one or more of their corners. For this reason, the release algorithm was modified to target the microraft corners before the center for a maximum of 8 needle attempts [Fig. 3.4 and Fig. 3.5]. Each microraft required an average of 8±0 needle actuations requiring 2.1±0.0 s per actuation to release (N=3 arrays, n=32 microrafts each). Even though this new approach required more needle actuations than those needed for the small microrafts (6±2 needle actuations), the approach resulted in a release efficiency of 98±4% for the large microrafts (N=3 arrays, n=32 microrafts each).[84] A pick-and-place assembly equipped with a magnetic wand then collected, transferred, and deposited each released microraft into individual wells of a multi-well plate. The magnetic wand was designed for the small microrafts demonstrated nearly 100% collection efficiency with these small objects containing 1% γ-Fe_2O_3 beads but <95% efficiency with the large objects containing 2.5% beads.[84] To enhance large-raft collection and deposition efficiency, the wait durations of the wand after placement

above the microraft array (after microraft release) and during deposition of the microraft in the multi-well plate were increased to 15 s (from 8 s) and 12 s (from 3 s), respectively.[84] Consequently, the combined collection/deposition efficiency was increased to 99±2% (N=3 arrays, n=32 microrafts each). The total time from microraft targeting to collection/deposition was 90±1 s per microraft (N=3 arrays, n=32 microrafts each); therefore, the fully automated system could sort 96 microrafts to fill one microwell plate without human intervention in 2.4 h. These metrics indicate that the microraft array platform can efficiently sort large numbers of fixed gastruloids for high-throughput screens. Given that the system was housed in a CO_2 and temperature-controlled housing, sorting of living gastruloids is also enabled but only for gastruloid behaviors with a time constant of 3 h or greater.

3.3.7. Systematic Imaging, Selection, and Analysis of Euploid and Aneuploid Gastruloids

The innovative capabilities of the microrafts to screen and sort single gastruloids were demonstrated with euploid and aneuploid gastruloids. I hypothesized that NOG would be upregulated in the euploid gastruloids relative to aneuploid gastruloids because normal gastruloids contain germ layer lineages requiring the inhibition of BMP signaling at the colony center.[54] KRT7 is a preimplantation trophectoderm marker expressed in the outer edges of normal gastruloids; therefore, I hypothesized that KRT7 would be upregulated in the aneuploid gastruloids relative to euploid gastruloids since aneuploid gastruloids primarily consist of trophectoderm cells.[16,88] To form euploid and aneuploid gastruloids, hPSCs were either untreated or treated with 0.5 μM reversine before being seeded onto the micropatterns. Subsequently, the living gastruloids were stained with calcein (cell viability marker) and Hoechst 33342. Given the inherent heterogeneity at the single-cell level, gastruloids are fundamentally diverse at the multicellular level [Fig. 3.13(b)]. The gastruloids derived from reversine-treated cells with diverse karyotypes are even more likely to exhibit heterogeneity between each gastruloid. Since both the euploid and aneuploid gastruloids possess a wide spectrum or distribution of properties, assaying individual gastruloids becomes critical as bulk analyses would overlook fundamental differences at the single-gastruloid level.

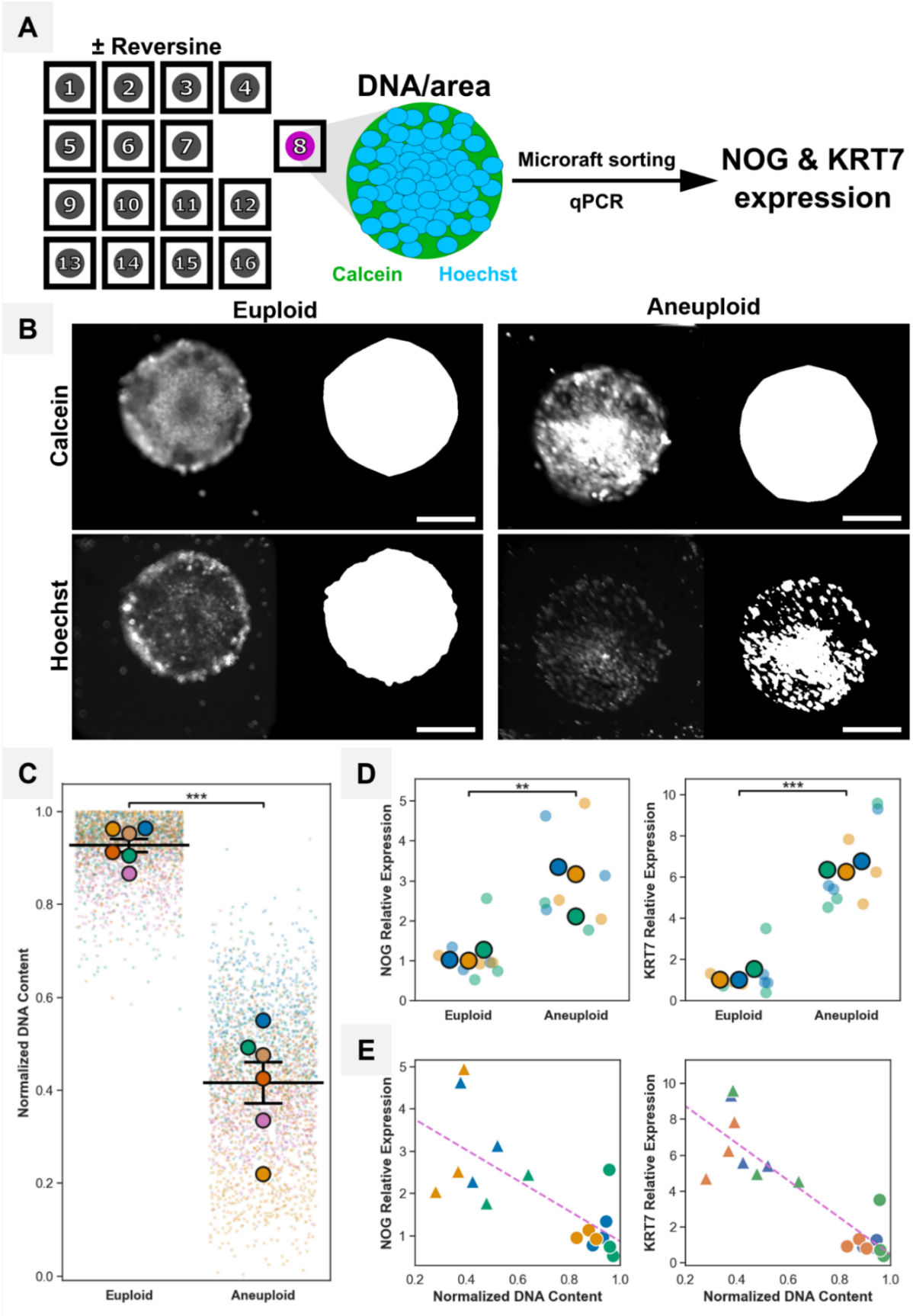
A
± Reversine
1
2
3
4
5
6
7
8
9
10
11
12
13
14
15
16
DNA/area
Calcein
Hoechst
Microraft sorting
qPCR
NOG & KRT7 expression
B
Euploid
Aneuploid
Calcein
Hoechst
C
***
Normalized DNA Content
1.0
0.8
0.6
0.4
0.2
0.0
Euploid
Aneuploid
D
**
NOG Relative Expression
Euploid
Aneuploid
***
KRT7 Relative Expression
Euploid
Aneuploid
E
NOG Relative Expression
Normalized DNA Content
KRT7 Relative Expression
Normalized DNA Content

Fig. 3.18. Aneuploid gastruloids display lower normalized DNA content and greater NOG and KRT7 expression levels than euploid gastruloids. (a) Overview of gastruloid assay workflow. Reversine-treated or untreated hPSCs were seeded on micropatterned microraft arrays to form gastruloids via a 48-h BMP4 treatment before live staining (calcein and Hoechst 33342) and imaging. Indexed microrafts with centered gastruloids displaying adequate stain signal were screened for DNA content within the gastruloids (fluorescence area of Hoechst staining normalized to area of ROI mask) before select microrafts were isolated onto a 96-well plate. Subsequently, KRT7 expression was measured in the isolated colonies via RT-qPCR. (b) Original fluorescence images and corresponding segmented masks for a single euploid and a single aneuploid gastruloid. Scale bars, 200 μm. (c) Normalized DNA content of euploid or aneuploid gastruloids calculated from calcein and Hoechst 33342 staining. N=6 arrays for each euploid and aneuploid condition (n≥354 microrafts each). $p<<0.001$, t-test. Mean cross bars, standard error bars, and t-test were calculated from replicate-level means. (d) NOG and KRT7 mRNA expression normalized to GAPDH mRNA expression for euploid and aneuploid gastruloids. N=3 arrays for each condition, n=3 gastruloids per array (except for the final replicate of aneuploid NOG expression where n=2 gastruloids). $p_{NOG}=0.01$, $p_{KRT7}<<0.001$, t-tests from replicate-level means. For panels (c-d), outlined circular markers represent means, while smaller markers represent individual samples. (e) Correlation between relative expression and normalized DNA content in euploid (circles) and aneuploid (triangles) gastruloids. Dotted line indicates line of best fit. N=3 arrays for each condition, n=3 gastruloids per array (except for the final replicate of aneuploid NOG expression where n=2 gastruloids). $r_{NOG}=-0.7$ ($p_{NOG}=0.001$), $r_{KRT7}=-0.9$ ($p_{KRT7}<<0.001$), Pearson's correlation. (c-e) Hues correspond to individual arrays. (d-e) Outlier GAPDH CT values and CT values exceeding 38 were excluded from the analysis.

Living gastruloids were screened and sorted based on the fluorescence area of the Hoechst 33342 stain normalized to the ROI area [Fig. 3.18]. This ratio or normalized DNA content then acted as a surrogate for the amount of DNA per unit area of each gastruloid [Fig. 3.18(a) and Fig. 3.18(b)]. Aneuploid gastruloids were observed to have fewer cells than euploid gastruloids.[16] Thus, aneuploid gastruloids were expected to display a lower normalized DNA content compared to that of their euploid counterparts. Imaging the living arrays took an average of 10.9±0.7 min per array for transmitted light and both fluorescence wavelengths (calcein and Hoechst 33342) (N=12 arrays). The computational pipeline revealed a clear phenotypic difference between the euploid and aneuploid gastruloids, where the aneuploid gastruloids displayed a significantly lower normalized DNA content (N=6 arrays for each euploid and aneuploid condition) [Fig. 3.18(b) and 3.18(c)]. There was no significant difference in the mean total areas of both euploid and aneuploid gastruloids (N=6 arrays for each condition, p=0.2) [Fig. 3.19]. Interestingly, there was greater variability in the normalized DNA content among the aneuploid (0.42±26%) than euploid (0.93±4%) gastruloids, which is likely explained by the heterogenous aneuploidy induced by reversine (N=6 arrays for each condition) [Fig. 3.18(c)]. Given the ability of the microraft array platform to screen individual indexed gastruloids, outliers for both conditions were manually inspected [Fig. 3.20]. The three euploid gastruloids with the lowest normalized DNA content possessed a sufficiently low content (~0.6) so as to be similar to

that of the aneuploid gastruloids [Fig. 3.20]. Some gastruloids comprised solely of euploid cells likely failed to develop into "normal" gastruloids. The three aneuploid gastruloids with the highest normalized DNA content (0.8-0.9) were non-circular colonies with densely packed nuclei and appeared to adopt a 3D structure [Fig. 3.20]. The three aneuploid gastruloids with the lowest normalized DNA content (≤0.01) displayed low Hoechst 33342 signal [Fig. 3.20]. Although the gastruloids for each condition developed under the same culture conditions, there is clear technical and biological variability in morphology, supporting the importance of single gastruloid analysis.

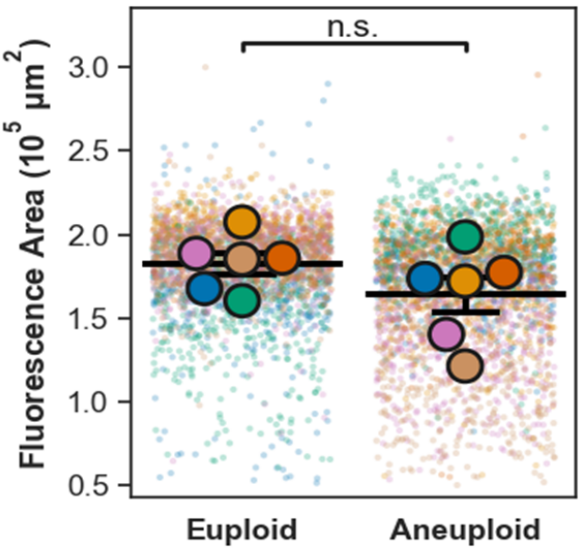

Fig. 3.19. Euploid and aneuploid gastruloids are similarly sized. ROI area for euploid and aneuploid gastruloids. Hues correspond to individual arrays. Outlined circular markers represent means, while smaller markers represent individual samples. N=5 arrays for each condition (n≥354 microrafts each), p=0.2, t-test. Mean cross bars, standard error bars, and t-test were calculated from replicate-level means. n.s. indicates no statistical difference.

Isolated gastruloids were individually assayed for their NOG and KRT7 mRNA expression levels [Fig. 3.18(d) and Fig. 3.18(e)]. Representative gastruloids with varying normalized DNA content (3 gastruloids per array) were released and collected. For each isolated gastruloid, the mRNA expression of NOG and KRT7 normalized to glyceraldehyde 3-phosphate dehydrogenase (GAPDH) mRNA expression was calculated via real-time quantitative polymerase chain reaction (RT-qPCR). Aneuploid gastruloids had greater relative expression levels of both NOG and KRT7 than euploid gastruloids (N=3 arrays each for each condition, p_{NOG}=0.01, p_{KRT7}<<0.001) [Fig. 3.18(d)]. The mean relative expression of NOG was 1.1±0.1 and 2.9±0.5 in euploid and aneuploid gastruloids, while the mean relative expression of KRT7 was 1.2±0.2 and 6.5±0.2 in euploid and aneuploid gastruloids, respectively (N=3 arrays for each condition). Although the relative expression of both genes for each condition did not greatly vary between replicates, the relative expressions from a few gastruloids deviated from their corresponding condition-specific means. For example, an euploid gastruloid had at least a two-fold greater relative expression of NOG (2.6) and KRT7 (3.5) than the means of each gene for euploid gastruloids. An aneuploid gastruloid had almost a two-fold

lower relative expression of NOG (1.8) than the mean for aneuploid gastruloids. Notably, identifying gastruloids with unique gene expression levels would not have been possible without the power to isolate and assay single gastruloids. NOG upregulation in the aneuploid gastruloids did not support our hypothesis. mRNA levels do not always predict translated protein levels, since genes such as transcription factors and signaling genes (like NOG) can produce unstable mRNA and correspondingly little protein.[95] Other factors such as translational or post-translational regulation can also play a role.[96] Future work integrating downstream protein-level assays, such as Western blotting or enzyme-linked immunosorbent assay (ELISA), can be easily performed with the isolated gastruloids to compare the gene expression and protein levels of both NOG and KRT7. One major advantage of the microraft array technology is the ability to connect image-based phenotype information and qPCR-based RNA expression data directly. There were strong negative correlations between normalized DNA content and the relative expression of both NOG (Pearson's coefficient: -0.7, $p=0.001$) and KRT7 (Pearson's coefficient: -0.9, $p<<0.001$) (N=3 arrays each for each condition) [Fig. 3.18(e)]. This suggests that gastruloids with less DNA appear to exhibit upregulated NOG and KRT7. These data demonstrate that the microraft array platform can identify and isolate gastruloids with a heterogeneous multicellular morphology from the same culture for downstream analyses.

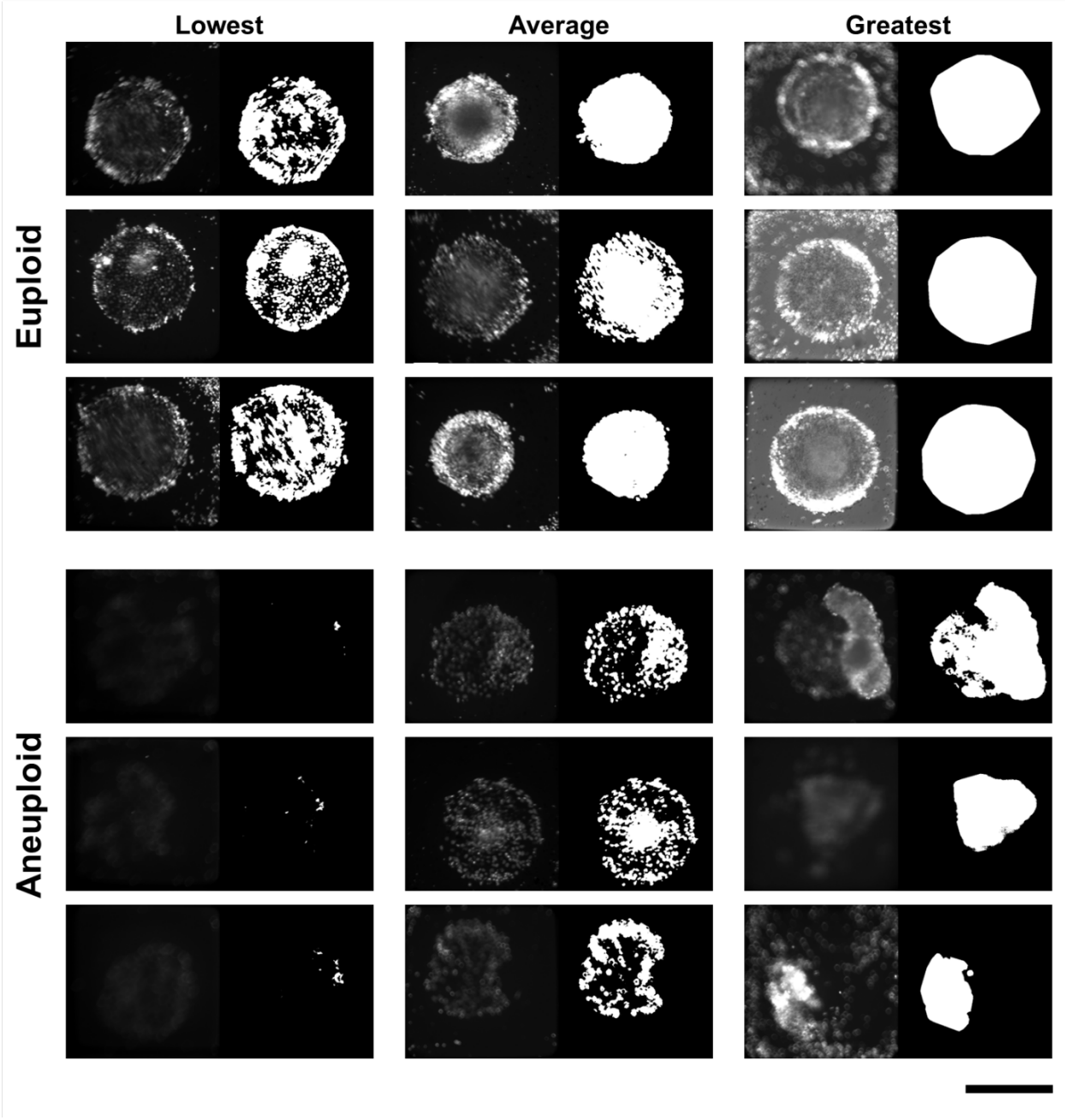

Fig. 3.20. Heterogeneous morphology of gastruloids with varying normalized DNA content. Widefield fluorescence images of Hoechst 33342-labeled gastruloids with corresponding segmentation masks for euploid (top) and aneuploid (bottom) gastruloids with the lowest, average, and greatest normalized DNA content. Scale bar, 400 μm.

CHAPTER 4. HETEROGENOUS PATTERNING BEHAVIOR EMERGES FROM HUMAN STEM CELL-BASED EMBRYO MODEL

Chapter 4 has been adapted from the following: Jan, I., Evarts, J. I., Cain, J.Y., Chiu P., Yang, M., Bagheri, N. & Allbritton, N. L. Heterogeneous Patterning Behavior Emerges from Human Stem Cell-Based Embryo Model. Under review in APL Bioengineering (2026).

4.1. Introduction

Human embryogenesis involves the complex yet concerted organization of multiple cell types. Consequently, heterogeneity can arise among developmental processes and pregnancy outcomes. Observed as early as the first cell fate decision, heterogeneity has major implications for reproduction, as only a third of human conceptions result in live birth.[1,29] Studying the developmental trajectories of early embryos has the potential to improve our understanding of the mechanisms of early pregnancy loss. Given technical and ethical limitations surrounding human embryos, human stem cell-based embryo models (SCBEMs) are crucial for both the fundamental understanding of healthy embryonic development and the development of reproductive treatments.[49,50,78] While animal models have led to our improved understanding of embryogenesis, these models do not fully mimic the human process. For these reasons as well as ethical and cost concerns, national agencies such as the National Institutes of Health (NIH) and the U.S. Food and Drug Administration (FDA) have proposed to phase out animal models.[97,98] An example of a human SCBEM is the two-dimensional (2D) gastruloid, termed “gastruloid” in this report. To create these entities, human pluripotent stem cell (hPSC) colonies are cultured in geometrically confined spaces coated with extracellular matrix (ECM).[36] After cell attachment, the mature gastruloid is formed upon treatment with bone morphogenetic protein 4 (BMP4). Gastruloids display the self-patterning of an extraembryonic trophectoderm-like region and the germ layers (endoderm, mesoderm, and ectoderm) that give rise to the different organs within the embryo. This model system has been proven invaluable for both fundamental studies and to reveal clinical insights. In addition to elucidating the complex signaling cascade (consisting of the BMP, Wnt, and Nodal pathways) underlying gastrulation, gastruloids have been used to model the depletion of aneuploid cells possessing abnormal sets of chromosomes.[16,54] Gastruloids can be cultured as scalable arrays and formed in 48 h, thus gastruloids are an ideal embryo model to capture

dynamic processes at scale via quantitative and high-dimensional measurements.[36,54,99] Even when derived from the same cell line, the individual multicellular entities exhibit significant heterogeneity across different experiments as well as within the same experiment.[51,100,101] Furthermore, individual hPSCs within a single population display substantial variability, which has been hypothesized to provide hPSCs the flexibility for diverse lineage specification.[27,56] Currently, no high-throughput or high-content analytical technologies can quantify the emergence of heterogeneity among developing gastruloids to better understand the experimental impact of this heterogeneity.

Comprehensive characterization of the gastruloid model system calls for novel tools to connect information across multiple modalities, such as morphology and gene expression levels. Studying the complex dynamics of self-patterning during early embryonic development also requires noninvasive image-based tracking of the lineage specification within the gastruloids. The conventional approach to image analysis using human-led feature extraction can introduce bias and miss multi-dimensional features that are difficult to quantify by simple metrics.[68,69,71] In response, deep learning has been used to identify cell density and SOX2 (marker for pluripotency and the ectoderm) stability as key parameters to distinguish phenotypes—including gastrulation failure modes—of endpoint, fixed gastruloids[102] This strategy created latent representations, or embeddings, derived from intensity measurements of different cell lineage markers along the radius of each gastruloid and did not include transcriptomic data. Connecting gene expression to image features would support a deeper understanding between patterning and the underlying signaling dynamics. The recent adaptation of the microraft platform to gastruloids has opened the door to couple high-resolution imaging followed by sorting and gene expression assay on the imaged gastruloids.[63] Further development of the innovative microraft platform to connect time-series imaging and endpoint gene expression data on single gastruloids would empower detailed studies of gastruloid heterogeneity.

For the high-throughput screening and sorting of gastruloids, arrays containing hundreds of gastruloids as described previously were utilized.[63] On these arrays, each gastruloid is positioned on an optically clear, releasable carrier or microrafts. These microrafts are uniform in dimensions with large, central, flat regions suitable for ECM placement and gastruloid formation. The microrafts possess embedded superparamagnetic beads at their edges, enabling collection by a magnetic wand upon

dislodgement from the array.[63,103] Gastruloids formed from RUES2 hPSCs on both the microraft arrays and the gold-standard flat polystyrene multi-well plates displayed clearly segregated tissue zones corresponding to three tissue layers (ectoderm, mesoderm, and trophectoderm).[63] Gastruloids on the microrafts and polystyrene plates also closely resembled each other in overall size of the cell lineage regions. Thus, microraft arrays are an excellent culture surface for gastruloids, compatible with high-quality microscopy, and offer the potential for gastruloid sorting.

Here, an integrated suite of tools (from imaging to mechanical sorting) was developed to characterize gastruloid heterogeneity and address fundamental biological questions regarding early embryogenesis. Time-series imaging across 48 h of living gastruloids developing on microrafts was performed. A single array possessed 529 microrafts each carrying an individual gastruloid derived from cells expressing fluorescent reporters for germ layer markers. Low-dimensional latent representations were constructed from high-throughput imaging of the SOX2 reporter to identify potentially novel gastruloid phenotypes. Directly creating the embeddings from the images requires minimal prior knowledge (thereby reducing bias), allows for fast hypothesis generation, and captures rich spatiotemporal information. Visual inspection of latent dimensions using perturbation-based methods revealed the main morphological features describing the variability among gastruloids from multiple batches. The microraft array platform also supported the isolation of single gastruloids after imaging for downstream gene expression analysis via bulk RNA sequencing (RNA-seq). RNA-seq library preparation of single gastruloids (each with ~1000 cells) enabled the analysis of transcriptomic variability across gastruloids between experiments and within a single experiment, revealing surprising heterogeneity despite all gastruloids being derived from thawed aliquots of a single cell line.

4.2. Methods

4.2.1. Microraft Array Fabrication

Microraft arrays formed on a polydimethylsiloxane (PDMS) (#2065622, Dow Silicones Corp., Midland, MI) template possessed 529 polystyrene microrafts (789 x 789 μm x 100 μm, L x W x H dimensions) and were fabricated using methods previously described.[63]

4.2.2. Cell Culture and Gastruloid Formation

RUES2 human pluripotent stem cells (hPSCs) (NIHhESC-09-0013) expressing a SOX2-mCitrine reporter were cultured in mTeSR Plus medium (#100-0276, STEMCELL Technologies, Vancouver, Canada) at 37°C and 5% CO_2 on multi-well plates coated with 1% Matrigel (#354234, Corning Inc., Corning, NY) [104]. The cells were detached for subculture using Accutase (#07920, STEMCELL Technologies, Vancouver, Canada) and replated in mTeSR Plus containing 10 μM Rho-associated kinase (ROCK) inhibitor Y-27632 (#B1293, APExBIO Technology LLC, Houston, TX) for 24 h. Aneuploidy was induced by treating cells with 0.5 μM reversine (#10004412, Cayman Chemicals Co., Ann Arbor, MI) for 24 h.

Gastruloids were formed on micropatterned microraft arrays as previously described.[63] Briefly, poly(l-lysin)100-grafted-poly(ethylene glycol)114-methoxy (PLL-g-PEG) (100 repeating units, 5000 Da, 20%; #11354, Nanosoft Polymers, Winston-Salem, NC) was diluted in PBS (#46-013-CM, Corning Inc., Corning, NY) and grafted onto the surface of a microraft array at 4°C overnight. Circular patterns centered on each microraft and free of PLL-g-PEG were formed via photoablation by illuminating with UV light through a photomask. The circular regions were then backfilled by incubation with 1% Matrigel (#354234, Corning Inc., Corning, NY) diluted in Advanced Dulbecco's Modified Eagle Medium (DMEM)/F12 (#12634-010, Gibco, Waltham, MA) media supplemented with 0.1 mg/mL gentamicin sulfate (#30-005-CR, Corning Inc., Corning, NY) at 4°C overnight and 25°C for 1 h before use. hPSCs were incubated with 10 μM Y-27632 for 1 h, washed with PBS, incubated in Accutase at 25°C for 3 min, washed with DMEM/F12, and centrifuged at 200 g for 3 min. The cells were resuspended, and 1.8x106 cells were seeded in mTeSR Plus with 10 μM Y-27632 on the array. The cells were allowed to attach onto the array at 37°C and 5% CO2 for 2 h. Subsequently, the array was placed into mTeSR Plus containing 50 ng/mL bone morphogenetic protein 4 (BMP4) (#314-BP-010, R&D Systems, Minneapolis, MN), and the micropatterned cells were cultured for 37°C and 5% CO2 for 48 h.

Three frozen aliquots (A, B, and C) of the same RUES2 cell line subculture were thawed to form gastruloids on the micropatterned microrafts [Table 4.1]. Each experimental batch was defined as a technical replicate initiated on a single day. The number of subcultures, or passages, was limited to 5 for each thawed aliquot.

Aliquot	Batch	Passage Number
A	0609	79
A	0617	81
B	0623	77
B	0630	79
C	0715	77
C	0722	79
C	0729	81

Table 4.1. Experimental batches with number of subcultures (passage number) corresponding to three aliquots of single cell line.

4.2.3. Gastruloid Imaging and Sorting

The automated microscopy system described previously was used to acquire both transmitted light and fluorescence images of each microraft array.[63] Custom MATLAB (MathWorks, Natick, MA) code utilizing a Micro-Manager (Open Imaging, San Francisco, CA) core controlled the system. The platform consisted of the following components: an inverted MVX10 MacroView fluorescence microscope (Evident Scientific, Tokyo, Japan) equipped with a 2x wide-field objective (0.25 NA); a motorized H112A microscope stage (Prior Scientific Inc., Rockland, MA); an ORCA-Flash4.0 V.3 digital CMOS camera (Hamamatsu Corp., Bridgewater, NJ); a Lumen 200 mercury lamphouse (Prior Scientific Inc., Rockland, MA); a LB10-NWIQ filter wheel with SmartShutter and an emission LB10-NWE filter wheel (Sutter Instrument, Novato, CA) fitted with a 8907 ET - ECFP/EYFP/DsRed filter set (Chroma Technology Corp, Bellow Falls, VT). Time-series imaging of the microrafts was performed over 48 h at 6-h intervals using the 4x magnification (1.7 μm/pixel). During this time, the arrays was housed within an incubation chamber maintaining 37°C, 5% CO_2, and 55% humidity levels.

Single gastruloids were isolated with the automated sorting system previously described.[63] Microrafts were released via an automated release device consisting of a thin needle and transferred using a microwand collection assembly from the array into individual wells of non-binding U-bottom 96-well plates (#650901, Greiner Bio-One, Monroe, NC). During microraft collection, each plate well contained mTeSR1 (#85857, STEMCELL Technologies, Vancouver, Canada). The medium was removed after microraft collection and replaced with 5 μL RNase-free 1X PBS (#BM-220S-DR, Boston BioProducts, Milford, MA) on ice.

4.4.4. Feature Measurement from Endpoint Gastruloids

The eccentricity and radius were measured from manually drawn masks for the region-of-interest (ROI) surrounding each gastruloid and the SOX2+ region of each endpoint gastruloid. Only gastruloids with properly formed ectoderms and not contacting the border were analyzed.

4.4.5. Image Feature Model Training

To analyze the morphological variance over time, an autoencoder framework with a single encoder and two decoders was designed. This architecture processed individual images independently while extracting meaningful spatial (morphological) features with a temporal context. To mitigate uneven background illumination and improve contrast, the background of each image was removed by performing Gaussian blur (σ = 50) and subtracting the blurred image from the original image. The processed images were then normalized to train the model. The encoder consisted of a convolutional neural network (CNN), mapping an input image to a low-dimensional latent representation of 16 dimensions (16D). Subsequently, this vector was passed into the two decoders: a spatial decoder for image reconstruction and a temporal decoder for predicting the relative time point. The encoder comprised a series of convolutional blocks and max-pooling layers. The spatial decoder (architectural mirror of the encoder) used convolutional and upsampling layers to reconstruct the image. The temporal decoder was a shallow multi-layer perceptron (MLP). To balance model efficacy and parsimony, the latent space was set to 16D. Larger dimensions introduced diminishing returns in model performance with regards to the loss function.

Model training was achieved by minimizing the weighted sum of the two objective functions (one for each decoder) defined as the total loss, L_{total}:

$$L_{total} = \alpha L_{spatial} + (1 - \alpha) L_{time}. \quad (1)$$

In (1), $L_{spatial}$ is the pixel-wise Mean Squared Error (MSE) used for optimizing image reconstruction, and L_{time} is the cross-entropy loss applied to the discrete time point prediction. The hyperparameter α defines the prioritization of the latent representations encoding spatial or temporal information. The models were optimized using the Adam optimizer.[105] Key hyperparameters (including optimizer hyperparameters, α, and dimensionality) were determined through a grid search aiming to minimize the combined spatiotemporal

loss on a dedicated validation set. All complete imaging time-series (where an image of the microraft was detected and segmented at each time point) were included in the dataset. The dataset was partitioned into training (60%), validation (20%), and test (20%) sets, ensuring images from the same gastruloid remained within one set to prevent data leakage. Training procedures were performed using the PyTorch deep learning framework version 2.5.1.[106] Imaging latent representations from only the test subset were visualized in the dimensionality reduction plots.

4.2.5. Bulk RNA-seq

Cell pellets stored at -80°C were thawed, centrifuged briefly to collect contents, suspended in an additional 7 µL of ice-cold 1X PBS, and mixed by pipetting several times. Subsequently, 10 µL of each sample were transferred to wells on a 384-well source plate (#264574, Thermo Fisher Scientific, Waltham, MA) for bulk RNA-seq. The following steps used reagents supplied with the SMART-Seq Pro Application Kit – 2 Chip (#640257, Takara Bio USA, San Jose, CA). First, a 6X dispense master mix containing 2.4 U/µL RNase Inhibitor, 0.06% BSA, and 6X Second Diluent was prepared and 2 µL of this was added to each well on the 384-well source plate and mixed by pipetting. All samples were then immediately dispensed into a 5184-nanowell 350v Chip using the iCELL8 cx Single-Cell System such that each sample was dispensed into 12 replicate wells on the nanowell chip. All subsequent steps were conducted according to the manufacturer's instructions for the SMART-Seq Pro Application Kit. After extraction from the chip, libraries were quantified using the KAPA Library Quantification Kit for Illumina (#KK4824, Kapa Biosystems, Wilmington, MA). Library size was confirmed using a 4200 TapeStation (Agilent, Santa Clara, CA). The library was then sequenced on one lane of a NovaSeq X Plus 10B flow cell (#20085594, Illumina, San Diego, CA) using a paired-end 150 base-pair sequencing configuration. Median sequencing yield was 22.8M read pairs (range 0.5 – 60.7M).

Sequencing reads were aligned to the GRCh38.p14 human genome reference assembly (GCA_000001405.29), and per-sample gene expression counts were quantified using the STAR v2.7.11b aligner. Gene expression analysis was performed via the web application, iDEP (v2.4.2, South Dakota State University, Brookings, SD).[107] Raw gene counts were filtered for genes with counts per million (CPM) ≥ 0.5 in at least 1 sample and transformed to log-CPM values in edgeR using the $\log_2(\text{CPM} + c)$ function where

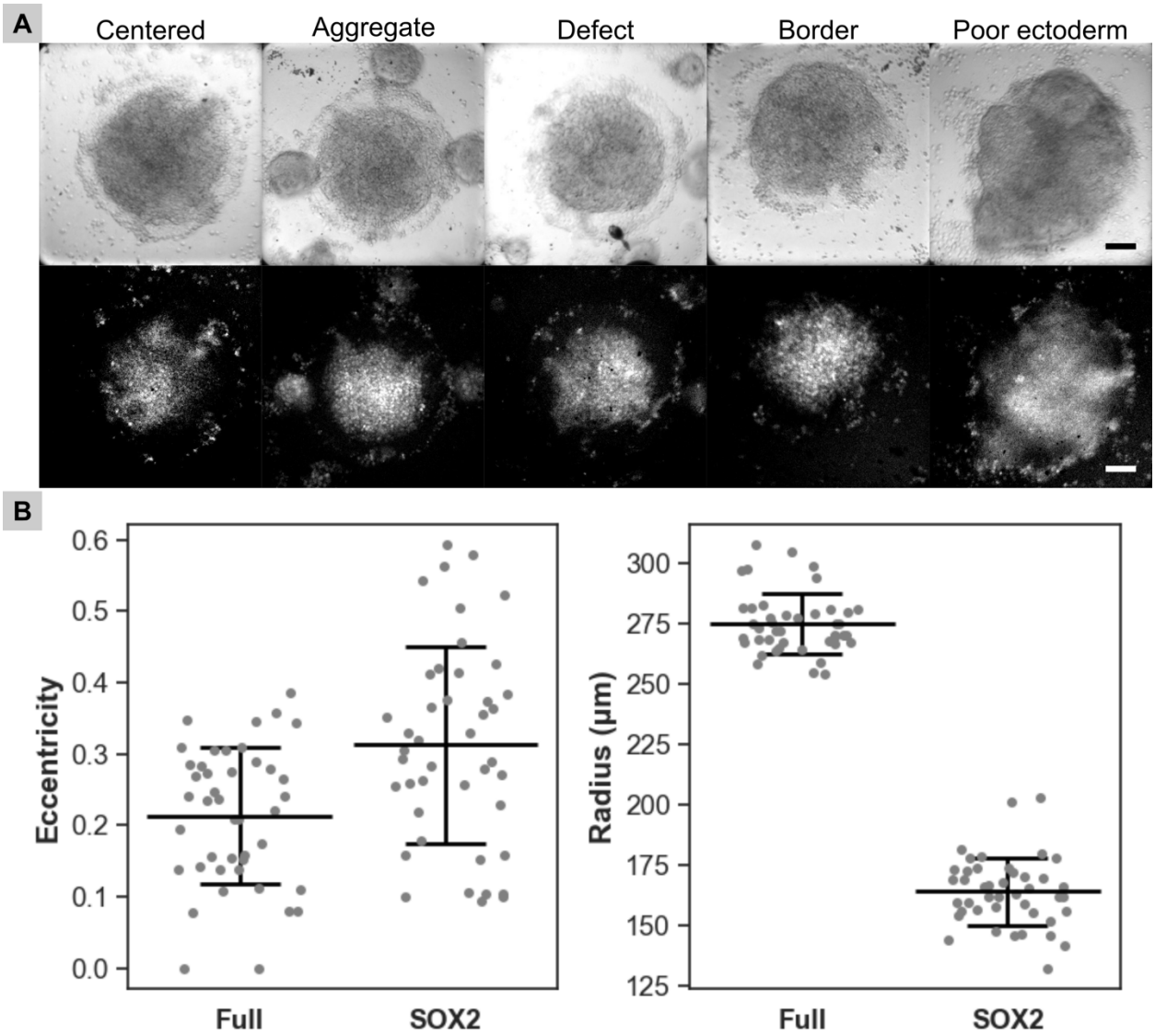

Fig. 4.1. Grading and simple feature measurements at the final time point of developed gastruloids derived hPSCs expressing a SOX2-mCitrine reporter. (a) Example transmitted light (top) and fluorescence (bottom) images of a microraft containing a centered gastruloid with a local, condensed SOX2+ region (centered); a microraft containing a gastruloid with adjacent cell aggregates (aggregate); a microraft with embedded superparamagnetic beads obscuring the view of the cultured gastruloid (defect); a microraft containing a gastruloid contacting the microraft edge (border); and a microraft containing a gastruloid with a irregularly shaped, dispersed SOX2+ region (poor ectoderm). Scale bars, 100 µm. (b) Eccentricity and radius values measured from manually drawn masks of the full gastruloid and SOX2+ region. N=1 batch, n=43 gastruloids.

pseudo-count c = 4. Missing values were calculated using the gene-wise median. For the heatmap visualizing highly variable genes, the processed gene counts were normalized by dividing the counts by the standard deviation for each gene. Differentially expressed genes (DEGs) were identified by comparing normalized gene expression levels from mosaic gastruloids to those of euploid gastruloids via the DESeq2 method with a False Discovery Rate (FDR) cutoff of 0.05 and a minimum fold-change threshold of 2. Independent filtering of low counts was performed.

4.2.6. Latent Dimension and Gene Expression Level Correlation

The similarity metric between each imaging latent dimension (*m*) and gene expression level (*n*) (both independently normalized between [-1, +1]) was calculated by:

$$Similarity = \begin{cases} -\left(1 - \left||m| - |n|\right|\right) \; if \; mn < 0 \\ \left(1 - \left||m| - |n|\right|\right) \; if \; mn \geq 0 \end{cases}. \quad (2)$$

The similarity metric was bounded by [-1, 1].

4.3. Results and Discussion

4.3.1. Gastruloids Consistently Develop on Microrafts

Because gastruloids derived from RUES2 hPSCs had been demonstrated previously on the microrafts, the platform was applied to a different hPSC line (RUES2 expressing SOX2-mCitrine reporter) for the live monitoring of SOX2 dynamics.[63] The SOX2-mCitrine reporter was employed to assess the consistency of gastruloid formation on the microrafts. Upon microscopy examination of the formed gastruloids on the microraft surface, every microraft (100%, n=50 gastruloids) contained a gastruloid. The majority of the gastruloids (92%) were properly aligned in the centers of the microrafts [Fig. 4.1]. A minority of the microrafts (12%) had defects, including embedded beads that blocked parts of the gastruloid and defects in the polystyrene. Most gastruloids (94%) had properly developed ectoderms indicated by a single localized, central SOX2+ region. Only 3 gastruloids exhibited dispersed or irregularly shaped ectoderm regions. Additionally, 24% of the gastruloids had adjacent cell aggregates, which formed from excess cells that detached from beyond the ECM patches. These cell aggregates did not obscure the imaging or greatly

affect the development of the gastruloids (only 1 gastruloid with poor ectoderm formation had adjacent aggregates). Previously, 90±20% of the stained (dyes and/or antibodies) gastruloids were reported to be properly aligned.[63] Gastruloid eccentricities were 0.2±0.1 and 0.3±0.1 for the full gastruloid and the SOX2+ region, respectively (n=43 gastruloids). The radius of the SOX2+ region (160±10 μm) was smaller than that of the full gastruloid (270±10 μm). These values are consistent with corresponding ones previously reported for eccentricity (0.3±0.0 for the full gastruloid and 0.3±0.0 for the SOX2+ region) and radius (251±4 μm for the ROI and 151±7 μm for the SOX2+ region).[63] These data suggested that the gastruloids derived from reporter cells were cultured with the same circular geometries and level of consistency as the gastruloids previously grown on the microrafts.

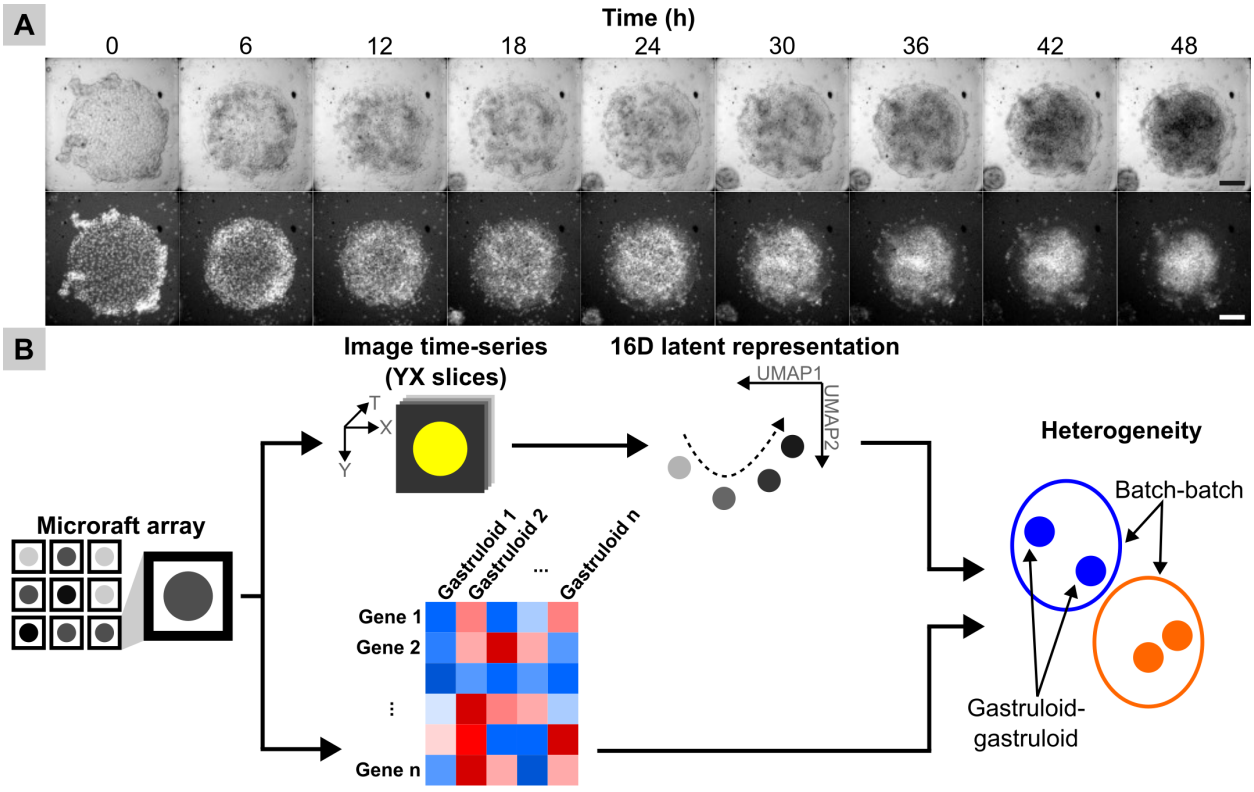

Fig. 4.2. Exploring single gastruloid heterogeneity. (a) Shown are sequential brightfield (upper row) and fluorescence (lower row) images using widefield microscopy of a single microraft possessing hPSCs expressing a SOX2-mCitrine reporter. BMP4 was added to the cultures at time 0 h to initiate gastruloid formation. Scale bar, 100 μm. (b) Schematic of the live time-series imaging and endpoint RNA-seq workflow. SOX2 dynamics and gene expression profiles of single gastruloids were acquired. 16D latent representations were formed from individual YX slices of imaging time-series (widefield microscopy) of each gastruloid and visualized via UMAP dimensionality reduction. Gastruloid heterogeneity across and within experimental batches was assessed using the image-based latent representations and sequence-based gene expression profiles.

4.3.2. Gastruloids Exhibit Remarkable Heterogeneity

Despite the similarities between gastruloids, this model system revealed morphological heterogeneity even within the same array. To examine the variability of the SOX2 signal during self-patterning, imaging time-series (9 YX images total with 6-h interval over 48 h) of gastruloids were captured from 7 batches derived from 3 aliquots (A, B, and C) of the same hPSC line [Fig. 4.2(a) and Table 4.1]. For each YX image slice, a 16D latent representation was generated via an autoencoder model in an unsupervised manner [Fig. 4.2(b)]. The embeddings were visualized by Uniform Manifold Approximation and Projection (UMAP) dimensionality reduction.[108] From the UMAP plot, the embeddings were grouped

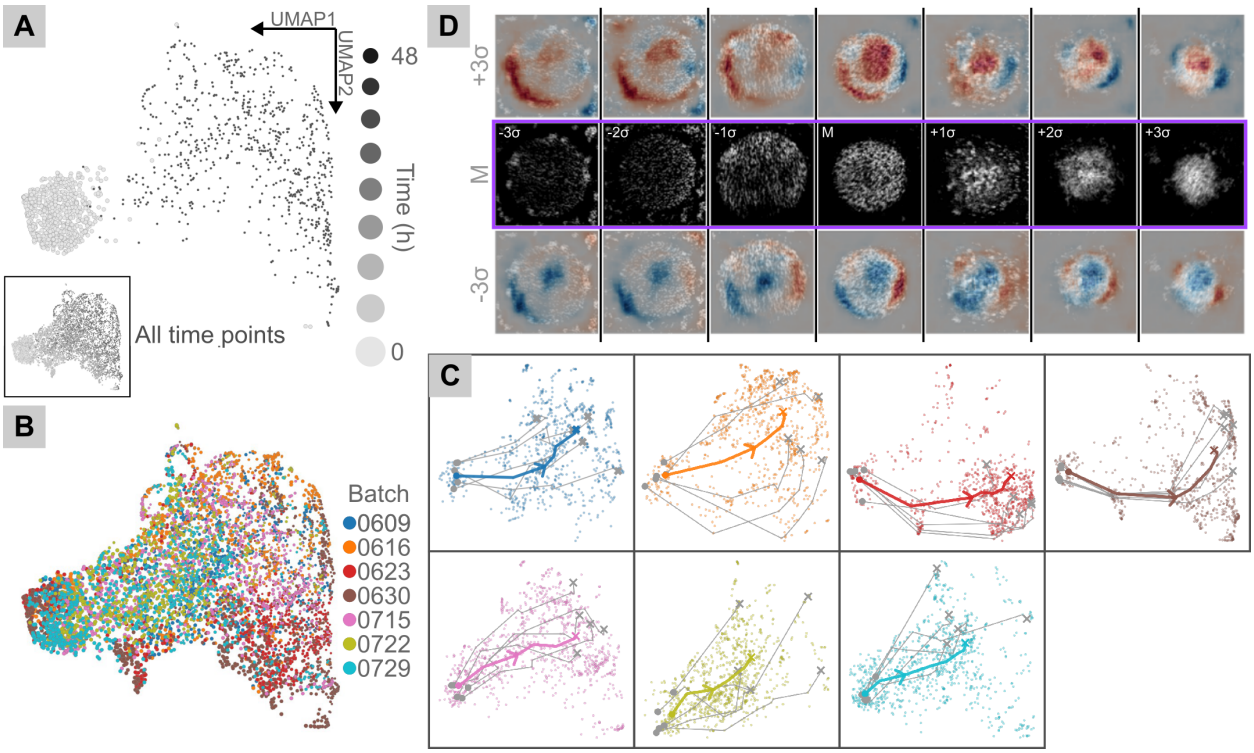

Fig. 4.3. Static latent representations learned from individual gastruloid images reveal heterogeneity. (a) UMAP plots visualizing 16D latent representations learned from individual static YX slices from imaging time-series of gastruloids. Main plot shows latent representations from initial and final time points (legend not to scale), while subplot shows latent representations from every time point. Shade within gradient corresponds to time point (6 h interval) during 48-h differentiation protocol. (b) UMAP plot visualizing latent representations from every time point where hue corresponds to batch. (c) UMAP plots for each batch visualizing average temporal trajectories of all batch-specific latent representations and trajectories of 5 randomly sampled gastruloids. The start (circle) and end points (x) for each trajectory were labeled. Hue corresponds to batch. For panels (a-c), N=7 batches. (d) Latent walk of latent feature #6. Along the middle row (purple), 7 example gastruloids with increasing latent feature #6 were ranked in the range of ±3 standard deviations (σ), including the median (M). For each column, visual counterfactual alteration of latent feature #6 in the range of ±3 standard deviations (σ), including the median (M), was displayed. Visual counterfactual alterations were normalized by the original example image, where red/blue indicate positive/negative changes in intensity, respectively.

together at the initial time point but dispersed by the final time point [Fig. 4.3(a)]. There was a general trend of the temporal trajectories of the latent representations towards the same direction along the UMAP1 axis. Notably, the latent representations dispersed along both UMAP1 and UMAP2 axes over time. Based on the spacing of latent representations at each time point, the morphology of the gastruloids was similar initially after seeding but deviated by the final time point at 48 h. Extracting latent features from thousands of gastruloid images across 9 time points revealed temporal dynamics of SOX2 expression in the developing gastruloids.

To understand the dispersion of latent representations in the UMAP plot, gastruloid images randomly sampled throughout the plot were visually inspected. Early-stage gastruloids (mainly represented by scattered dim SOX2 signal) were shifted toward higher UMAP1 values [Fig. 4.4]. On the other hand,

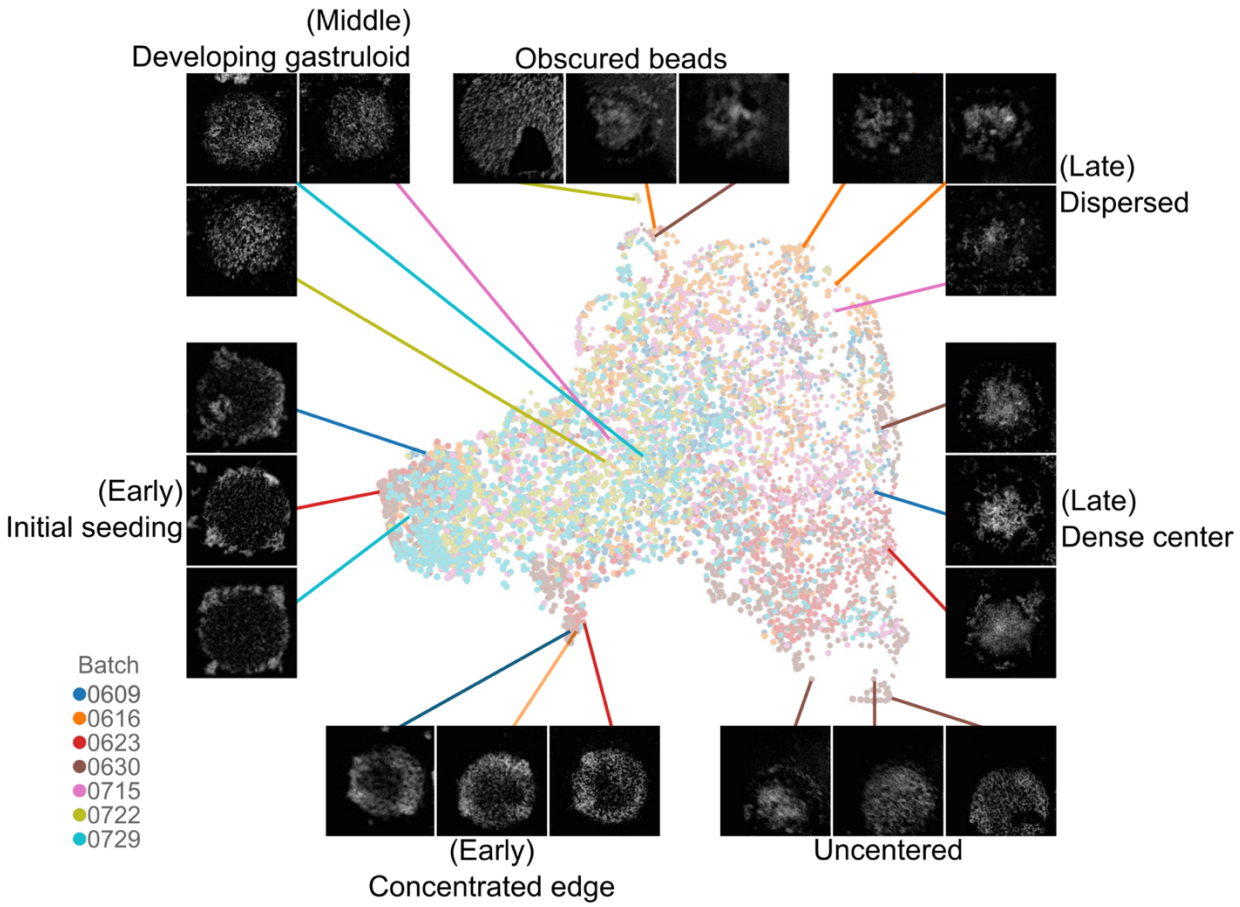

Fig. 4.4. Heterogeneous gastruloid morphology within latent space. Example gastruloids were randomly sampled from different regions of UMAP plot visualizing 16D latent representations created from individual static YX slices of imaging time-series at every time point. Hue corresponds to batch. N=7 batches.

late-stage gastruloids (either exhibiting dense central or dispersed SOX2 regions) were shifted toward lower UMAP1 values. Middle-stage developing gastruloids exhibited SOX2 regions more concentrated than those of early stage-gastruloids but less dense than those of late-stage gastruloids. There were outliers, such as early-stage gastruloids with concentrated SOX2 signal around the gastruloid edge. The experimental batch associated with each sampled latent representation and corresponding image was labeled, revealing latent representations from multiple batches were scattered throughout the plot. Interestingly, latent representations of uncentered gastruloids derived from a single batch were localized in the bottom right corner of the plot. Gastruloids are known to undergo complex multicellular processes and thereby reveal morphological differences throughout their development.[36,54,99] Both the developmental stage of the gastruloid as well as technical artifacts within the images appear to drive the remarkable heterogeneity of the latent representations.

4.3.3. Multiple Factors Support Gastruloid Variability

Experimental batch has been shown as a clear source of variability in multicellular model systems;[51,100,101] therefore, the role of batch in gastruloid heterogeneity was investigated. To observe batch-batch variability, the UMAP visualization of the latent space was dissected by batch [Fig. 4.3(b) and Fig. 4.3(c)]. The UMAP plot of the static latent representations revealed the scattering of latent representations associated with the different batches [Fig. 4.3(b)]. Importantly, the latent representations at each time point for a single gastruloid can be connected to trace a temporal trajectory describing the SOX2 dynamics during the gastruloid development. Separated by individual batches, the UMAP subplots displaying the average temporal trajectory exhibited clear batch effects [Fig. 4.3(c)]. The subplots for Batches 0623 and 0630 showed latent representations that were concentrated in the bottom right corner (low UMAP1 and high UMAP2 values). Dissecting the composite UMAP plot with all batches revealed variability by both cell culture aliquot (A, B, and C) and passage number (77, 79, and 81) [Fig. 4.5]. Specifically, both Batches 0623 and 0630 were the only batches derived from Aliquot B, which uniquely produced latent representations localized in the bottom right corner. Regardless, the average trajectories follow a general trend toward lower UMAP1 values [Fig. 4.3(c)]. Although the gastruloids were derived from cells of multiple thawed aliquots of a single cell line, technical variables (such as experimental batch, cell culture aliquot,

and number of passages in culture) introduced variability throughout the self-patterning. In addition to capturing the heterogeneity of the SOX2 signal at each time point, the latent representations assist in describing the complex temporal changes of single gastruloids between batches.

Pooled analyses of single gastruloids can easily overlook the heterogeneous dynamics at the single gastruloid level. Consequently, the trajectories of individual gastruloids were randomly sampled for each batch [Fig. 4.3(c)]. The sampled trajectories started in similar areas of the subplots and followed the general trend of the batch-specific averaged trajectory. However, the sampled trajectories generally deviated within the first 24 h and ended in diverse regions. Some trajectories started and ended in similar places (as shown in Batches 0623 and 0630), while others started in similar regions before ending in different areas (as shown in Batches 0609 and 0729). For some batches, the sampled trajectories appeared to even follow different sets of paths. The sample trajectories sometimes followed similar paths as the corresponding batch-specific

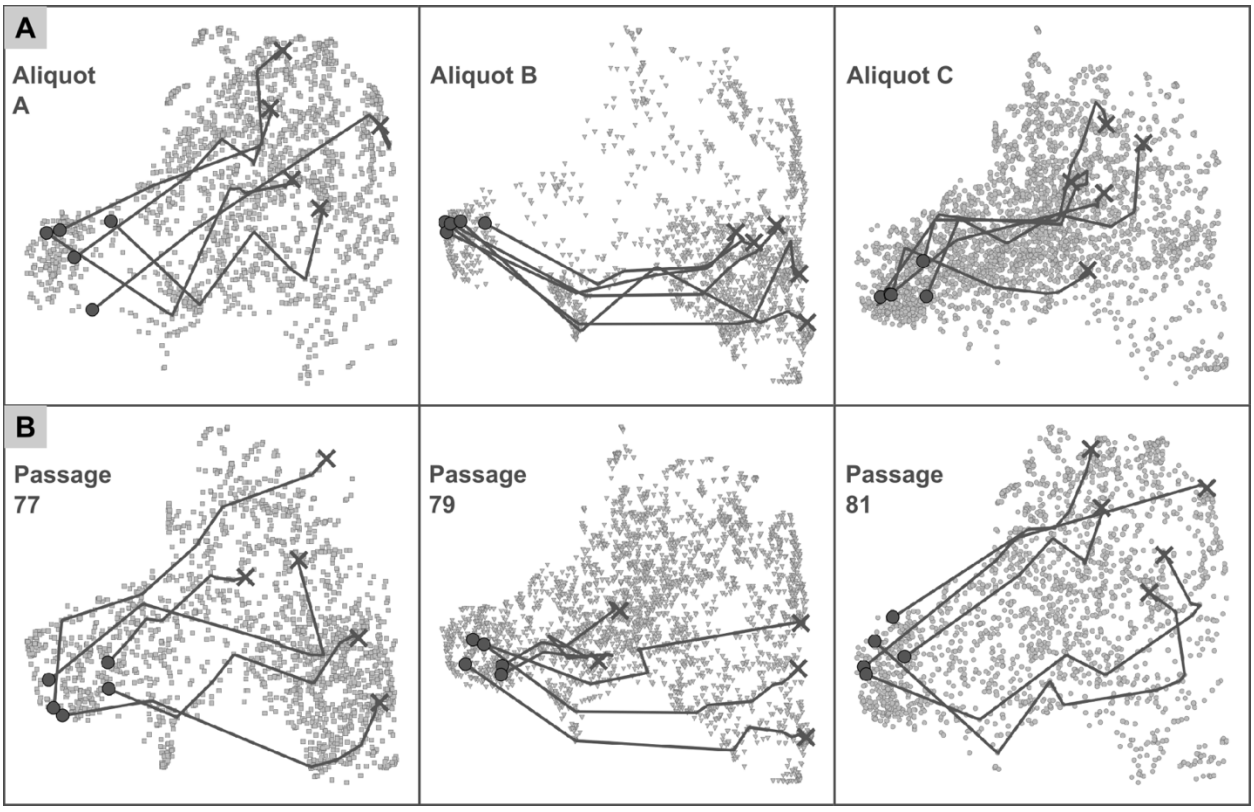

Fig. 4.5. Cell culture vial and passage number also contribute to variability. UMAP subplots visualizing latent representations learned from 2D slices of imaging time-series for each cell culture (a) aliquot and (b) number of passages. Temporal trajectories of 5 gastruloids were randomly sampled for each subplot, where the start (circle) and end points (x) were labeled. N_A=2 batches, N_B=2 batches, N_C=2 batches; N_{77}=2 batches, N_{79}=3 batches, N_{81}=2 batches.

averaged trajectory (as shown in Batches 0630 and 0715). On the other hand, some sampled trajectories followed paths above and below the corresponding batch-specific averaged trajectory (as shown in Batches 0616 and 0729). Similar observations were made from randomly sampled trajectories from the subplots corresponding to cell culture aliquots and passage numbers [Fig. 4.5]. In these subplots, the starting and ending points as well as the trajectory paths all varied. The trajectories from single gastruloids revealed remarkable heterogeneity of SOX2 dynamics that were masked by the batch-level averaged trajectories [Fig. 4.3(c)]. Previously, high-throughput screening of single endpoint gastruloids showed variability across all samples despite the measured features having similar replicate-level means.[63] Overall, the trajectories of the latent representations averaged at the batch-level and randomly sampled from single gastruloids captured the emergence of morphological heterogeneity not only between but also within batches.

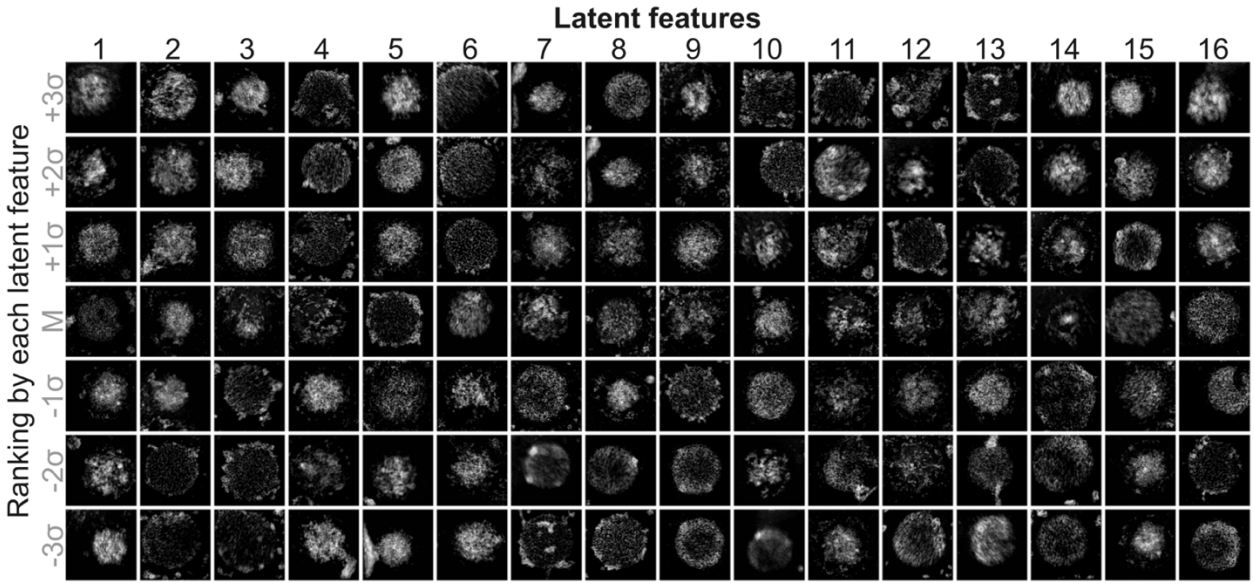

Fig. 4.6. Latent features capture different aspects of gastruloid variability. Latent walks for each latent feature (16 dimensions total) displaying example 7 gastruloids ranked by corresponding latent feature in the range of ±3 standard deviations (σ), including the median (M).

4.3.4. Biologically Relevant Features Can Be Extracted from Gastruloid Latent Representations

The interpretability of the latent features extracted by deep learning approaches can be challenging, but understanding these features can uncover structures with potential biological relevance in the image data. For each latent dimension, counterfactual analyses were performed by generating a series of 7 sample gastruloid images ranked by the specific latent feature within ±3 standard deviations [Fig. 4.6]. Each image series was visually inspected to determine the possible image features that the latent dimensions were capturing. Most of the features were not readily interpretable. Latent feature #1 appeared to encode the position of the gastruloids along the X-axis of the image. Additionally, changes to latent feature #6 appeared to encode the size of the central SOX2+ region within the gastruloids of each image. Latent representations can encompass subtle differences between images, such as small changes in 16-bit depth

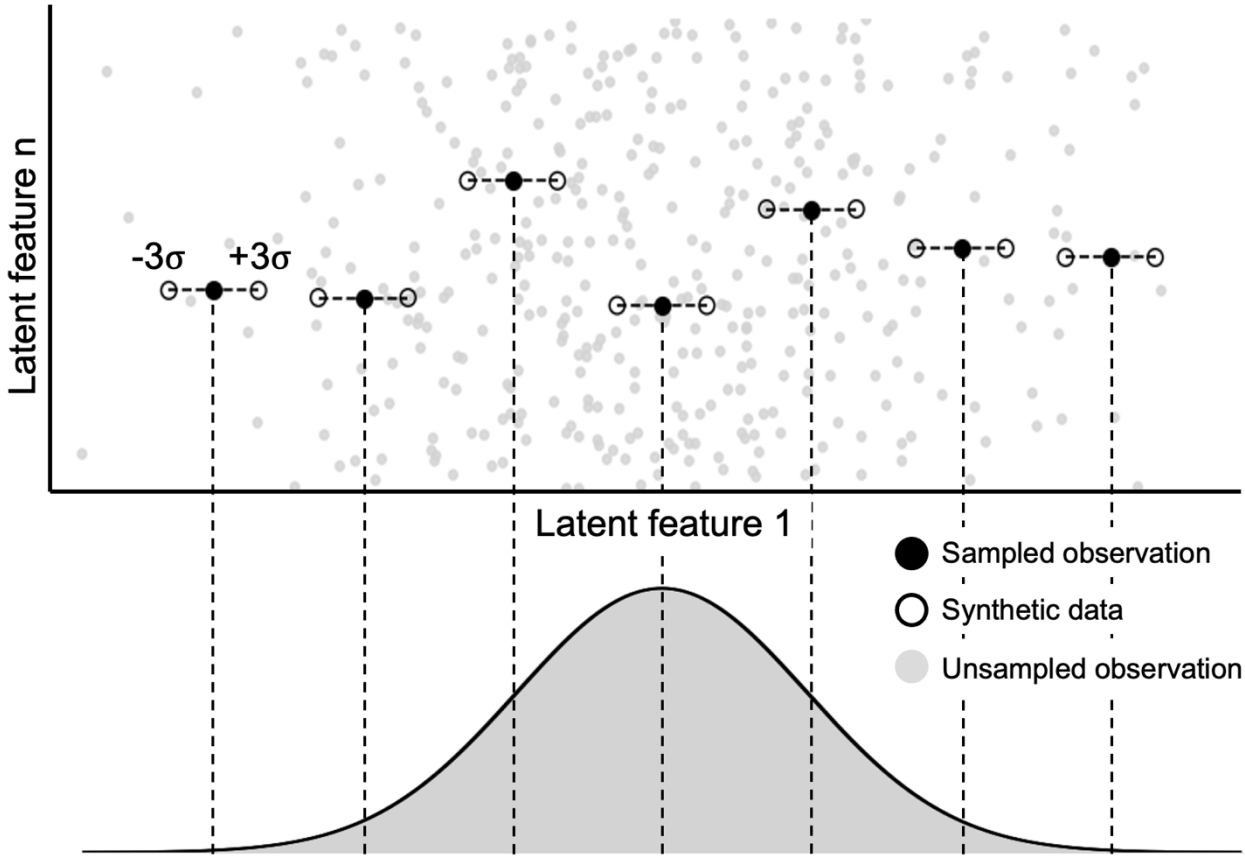

Fig. 4.7. Process overview of latent walk sampling for latent feature analysis. Latent features of all data points were ranked according to a target latent feature (e.g., latent feature 1), and sample points were selected along the resulting distribution. This ordering ignored variation in other latent dimensions (e.g., latent feature n). Synthetic latent vectors were constructed by perturbing only the target dimension while holding the other dimensions fixed. To isolate the effects of the perturbations to only the target feature, images were generated by feeding the synthetic latent vectors through the decoder.

intensity values or abstract structures formed by the SOX2 signal, that are not obvious to the human eye. Formed from the imaging time-series of the gastruloids, the latent representations captured nuanced but important differences with potential biological relevance between each image.

These series of real gastruloid images did not hold any of the other features constant, thereby complicating straightforward interpretation of the latent features. To address this, synthetic gastruloid images were generated from the original real images by perturbing each specific feature by ±3 standard deviations [Fig. 4.3(d) and Fig. 4.7]. The changes in intensity of the generated images were not easily discernable. Therefore, the synthetic images were normalized by the original real image to create a heatmap. Increases/decreases in intensity are indicated by red/blue, respectively. The synthetic heatmap pairs for each image showed that SOX2 intensity mainly in the gastruloid center correlated with the value of latent feature #6. Less obvious were changes in SOX2 intensity at the colony edges. SOX2 intensity increased at the bottom left edge of the gastruloid but decreased along the rest of the edge when latent feature #6 was increased. This counterfactual analysis further supported that latent feature #6 encoded the radial density of the SOX2 signal. The size of the central SOX2+ region is likely biologically relevant for self-patterning. Both cell density and SOX2 stability have been identified as driving parameters for patterning variability.[102] This proof-of-principle approach using both real and synthetic counterfactual images was employed to interpret abstract latent features with minimal prior knowledge.

4.3.5. Latent Representations Constructed from Complete Imaging Time-series Capture Temporal Dynamics

Because embryogenesis is a dynamic process rich with temporal information, the model was applied to study the entire sequence of each gastruloid evolving over time. The goal was to gain more insights into the heterogeneous progression of self-patterning among gastruloids from different experimental batches. Specifically, the model was trained on series of YX images captured over time, which form image stacks with three-dimensions (3D) (TYX). The model constructed a single 16D latent representation that encapsulated the SOX2 patterning over the entire time-series for each gastruloid [Fig. 4.8(a)]. UMAP dimensionality reduction was performed on the dynamic latent representations to show clear batch effects [Fig. 4.8(b)]. As a case study for qualitative interpretation via counterfactuals, latent feature

#5 appeared to encode the rate of condensation of the SOX2+ region at the gastruloid center [Fig. 4.8(c)]. The SOX2 signal is less localized at the gastruloid center at higher than lower values of latent feature #5. Interestingly, the example gastruloids had similar morphology at the initial time point but showed clear differences by 24 h. These dynamic latent representations encompassing the entire time-series captured temporal information missing from the static latent representations formed from YX slices at single time points. The static latent representations required connecting the embeddings from each time point for each gastruloid. Both types of latent representations provide important insights into the SOX2 dynamics across the different batches. In the UMAP plot of the dynamic embeddings, the latent representations from Batches 0623 and 0630 (Aliquot B) are more similar to each other than those from Batches 0722 and 0729 (Aliquot C) [Fig. 4.8(b)]. The average trajectories corresponding to these batches in the UMAP plot of the static latent representations support this observation [Fig. 4.3(c)]. Taken together, the latent representations extracted complex features from high-dimensional imaging data to describe the time-dependent emergence of gastruloid heterogeneity.

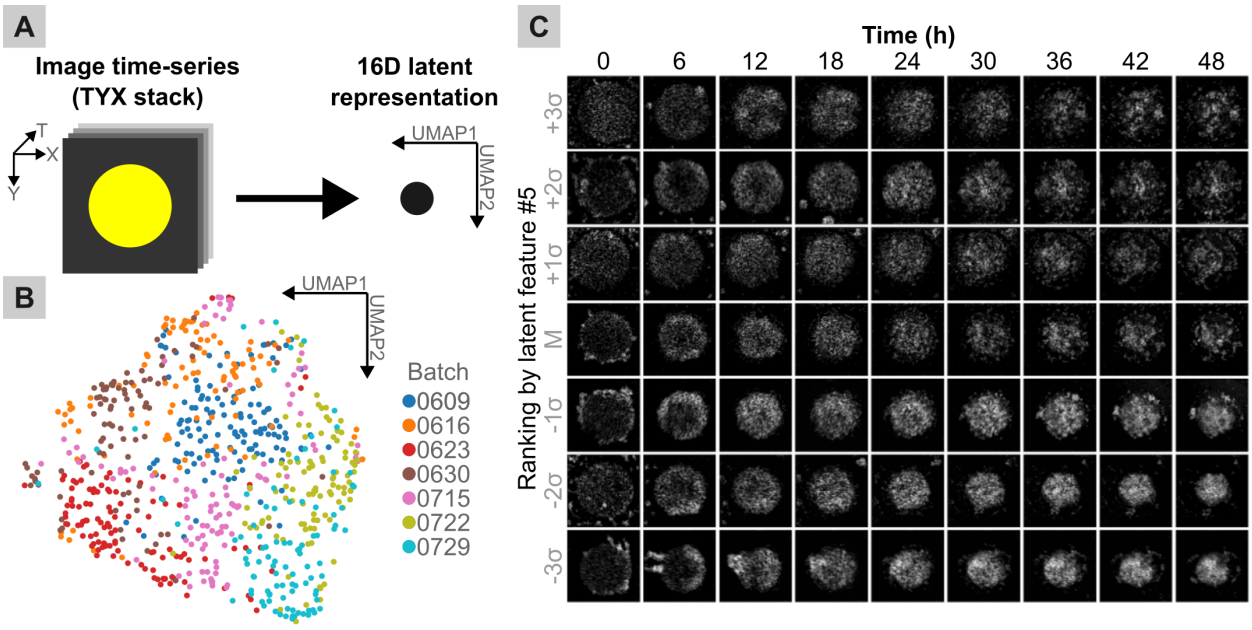

Fig. 4.8. Dynamic latent representations learned from complete gastruloid imaging time-series. (a) Schematic of workflow where each 16D latent representation was formed from a dynamic TYX stack of complete imaging time-series of a single gastruloid. (b) UMAP plot visualizing latent representations learned from 3D imaging time-series stacks. Hue corresponds to batch. N=7 batches. (c) Latent walks for latent feature #5 displaying imaging time-series over 48-h differentiation protocol of 7 example gastruloids ranked by latent feature #5 in the range of ±3 standard deviations (σ), including the median (M).

4.3.6. Transcriptomic Profiles of Single Gastruloids Reveal Heterogeneity

For a comprehensive assessment of gastruloid variability, the gene expression profiles of single gastruloids were investigated. A total of 29 gastruloids from 2 batches (n_{0722}=13 gastruloids, n_{0729}=16 gastruloids) were isolated, sequenced, and analyzed. Principal component analysis (PCA) was performed for dimensionality reduction of the gene expression data to visualize the sample variance of the data clearly [Fig. 4.9(a)]. The gene expression profiles were clearly separated by batch. Additionally, the top 1000 highly variable genes were visualized with a heatmap, where clustering was performed on both the genes and samples [Fig. 4.9(b)]. The samples were not only clustered by batch but also subclustered within each batch. Out of the 1000 genes, the top 10 highly variable genes were labeled. Most of the top 10 highly variable genes play critical roles in embryogenesis [Table 4.2]. For instance, CER1 and DKK4 are antagonists in the BMP, Nodal, and Wnt signaling cascade.[109,110] Other genes are involved in the patterning of specific structures or tissues, such as FGF17 (mesoderm and midbrain-hindbrain boundary), CYP26A1 (rostral neural plate and embryonic tail bud), and MIXL1 (mesoderm and endoderm).[111–114] The gastruloids clearly exhibit single-gastruloid variability across the different batches on both phenotypic and transcriptomic levels. This proof-of-concept experiment can inspire future targeted studies of the highly variable genes to determine whether the heterogeneity is derived from extrinsic or intrinsic factors.

Rank	Gene	Associated Processes	References
1	CER1 (cerberus 1)	Multifunctional inhibitor of BMP, Nodal, and Wnt signaling.	109
2	DKK4 (dickkopf WNT signaling pathway inhibitor 4)	Wnt/β-catenin antagonist.	110
3	FGF17 (fibroblast growth factor 17)	Involved in mesoderm differentiation and in establishing the midbrain-hindbrain boundary.	111,112,115
4	CYP26A1 (cytochrome P450 family 26 subfamily A member 1)	Helps regulate retinoic acid (RA), which is critical in vertebrate embryo patterning and organogenesis. Murine CYP26A1-null mutants died during mid-late gestation and displayed morphogenetic defects in the rostral neural plate and embryonic tail bud.	113
5	GLIPR1L1 (glioma pathogenesis-related protein 1)	Part of mammalian cysteine-rich secretory proteins, antigen 5, and pathogenesis-related 1 proteins (CAP) superfamily. Facilitates sperm-oocyte interaction.	116,117

6	MIXL1 (mix-like 1)	Crucial for mesodermal and endoderm development. Mouse epiblast stem cells showed temporal differences in MIXL expression, where cells with delayed MIXL upregulation were less responsive to NODAL signaling.	114,118,119
7	LINC00458 (long intergenic non-protein coding RNA 458)	Elevated in response to substrate stiffness. Promotes endoderm specification via SMAD2/3.	120
8	LINC01356 (long intergenic non-protein coding RNA 1356)	Elevated in response to substrate stiffness. Unclear role.	120
9	LOC729739	Peptidylprolyl isomerase A (cyclophilin A) pseudogene	
10	MT1G (metallothionein 1G)	Part of a group (metallothionein or MT) of genes encoding metal-binding proteins that perform a variety of roles (including metal homeostasis, oxidative stress, cell proliferation & differentiation, and inflammation). Interestingly, higher expression of MT1G was associated with preterm labor in fetal membranes and myometrium.	121,122

Table 4.2. Top 10 highly variable genes expressed by single euploid gastruloids.

4.3.7. Multimodal Characterization of Single Gastruloids Connects Phenotypic and Transcriptomic Information

Whether the latent representations and gene expression profiles provide correlated or orthogonal information about single gastruloids was unknown. The sorted microrafts have the powerful ability to connect imaging and sequencing data for the same biological sample. Therefore, the dynamic latent representations (encapsulating the complete imaging time-series) of the sequenced gastruloids from Batches 0722 and 0729 were initially visually assessed by subclusters (according to the gene expression profiles) [Fig. 4.9(c)]. The gene expression for the gastruloids from Batch 0722 revealed 3 subclusters, while those for gastruloids from Batch 0729 showed 4 subclusters. In general, the latent representations of gastruloids within the same subcluster did not appear to be closely located in the UMAP subplots derived from the imaging data. The embeddings for Subcluster 1B (Batch 0729) were dispersed along the imaging UMAP2 axis, while those for Subcluster 2B (Subcluster 0722) were spread out along the imaging UMAP1 axis. Consequently, the relationship of the different data modalities required further analysis.

To better identify a possible correlation between the imaging latent dimensions and the gene expression levels of single gastruloids, the normalized values of the imaging latent dimensions and gene expression levels of the top 10 highly variable genes were compared via heatmaps [Fig. 4.10]. The signed

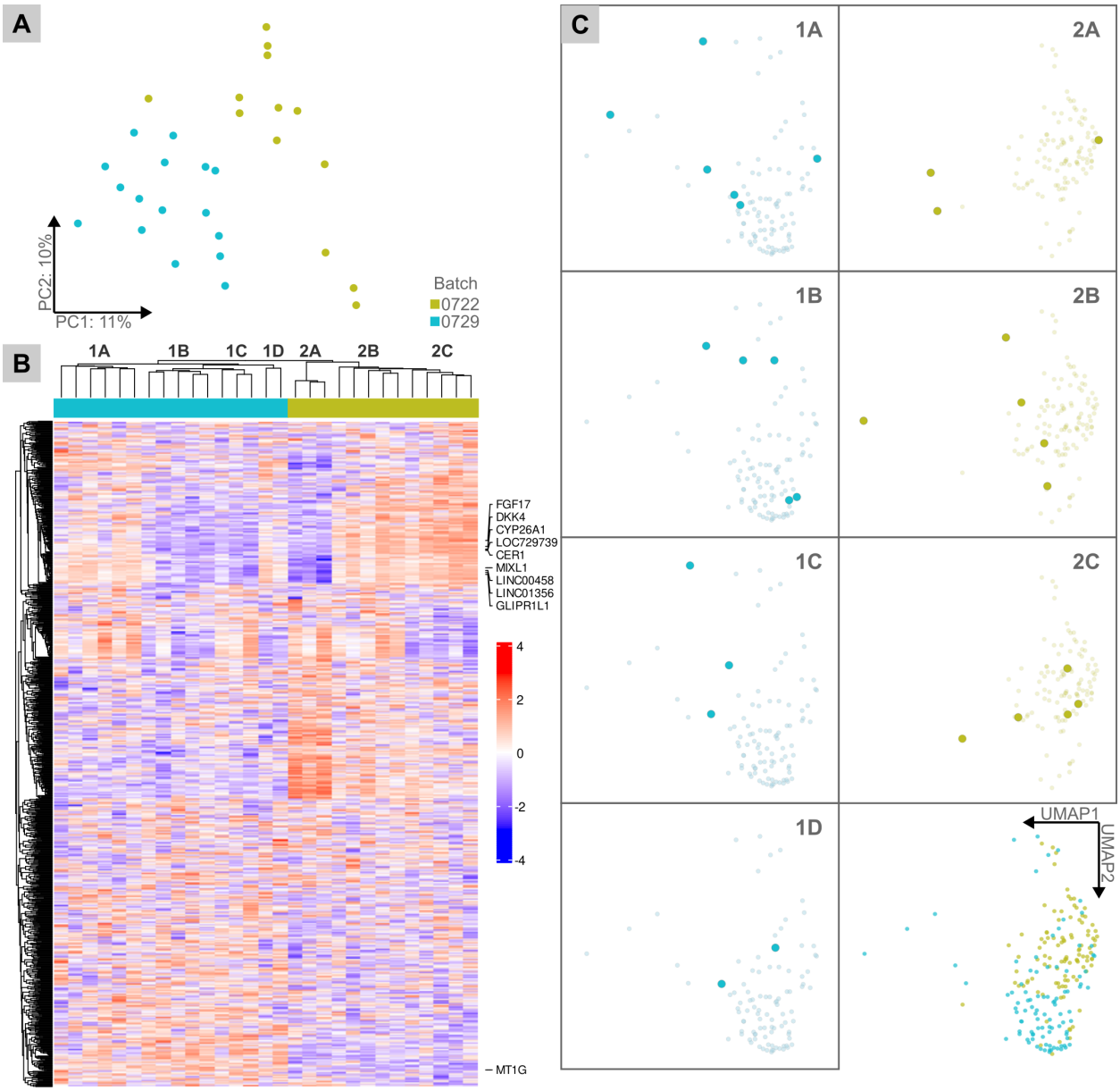

Fig. 4.9. Transcriptomic profiles of single gastruloids are heterogeneous. (a) Principal component analysis (PCA) plot of gene expression profiles from single gastruloids. Proportions of variances indicated for PC1 and PC2. Hue corresponds to batch. (b) Heatmap displaying normalized relative expression of the top 1000 highly variable genes. Hierarchical clustering of both genes and samples (hue corresponds to batch) was performed using Pearson correlation distance with average linkage. Sample clusters and top 10 highly variable genes were labeled. (c) UMAP plots visualizing the dynamic latent representations of the sequenced gastruloids (large markers) in each subcluster and of the gastruloids in each batch (small markers). Hue corresponds to batch. For panels (a-c), N=2 batches, n_{0722}=13 gastruloids, n_{0729}=16 gastruloids were sequenced.

similarity metric (dependent on both sign and magnitude) was calculated for each latent dimension and gene expression level pair. In general, there were no clear consistent patterns across the heatmaps. The similarity metrics of the samples within the same sequencing subclusters did not show trends. Because single genes can perform multiple functions, the connection between the imaging latent dimensions and gene expression levels was likely too complex for this simple visual examination. Machine learning might be employed in the future to elucidate novel combinatorial relationships between the data modalities when a sufficiently large training data set is available. Regardless, the microraft technology can enable these challenging analyses by integrating both imaging and sequencing data for single gastruloids.

These results suggest that the imaging and sequencing data provide orthogonal information regarding each gastruloid. Therefore, multimodal characterization is likely required to quantify gastruloid heterogeneity. To better elucidate the relationship between the imaging latent representations and gene

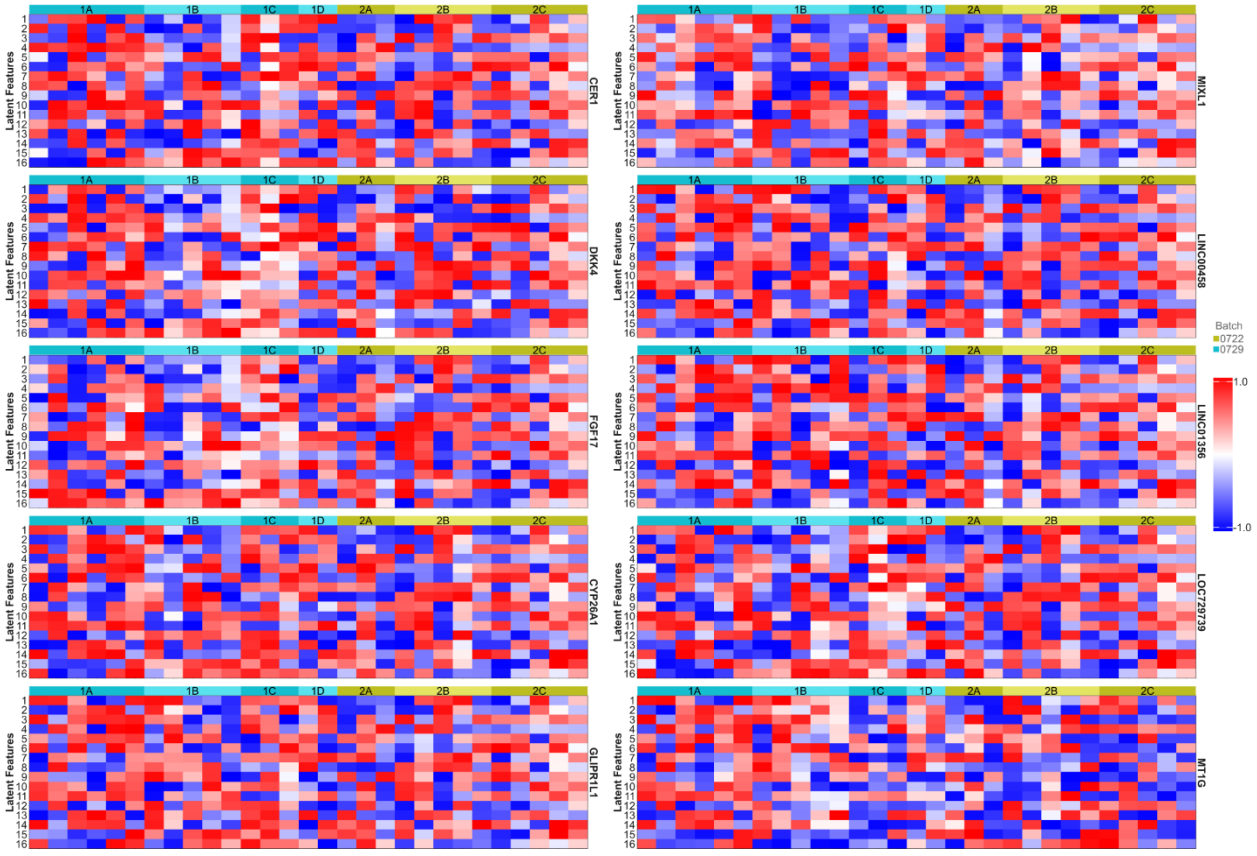

Fig. 4.10. Latent features do not directly correlate to gene expression levels. Heatmaps visualize normalized similarity metric calculated form normalized imaging latent features and expression levels for each of the top 10 highly variable genes. The gastruloid samples were organized by gene expression level subclusters (hue corresponds to batch). N=2 batches, n_{0722}=13 gastruloids, n_{0729}=16 gastruloids were sequenced.

expression profiles, the dimensionality reduction method could be optimized. UMAP dimensionality reduction is a non-linear approach to preserve the local and global structure of multi-dimensional data.[108] This abstraction can result in imaging latent representations of gastruloids with similar gene expression to appear unclustered. Alternatively, a computational pipeline that integrates both imaging and sequencing data could be developed. Recent deep learning-based approaches have been designed to incorporate imaging modalities for multi-omics analysis.[70,73,123] These preliminary findings warrant a larger-scale sequencing experiment to determine the connection between multiple data modalities for quantifying biological heterogeneity.

4.3.8. Mosaic Gastruloids Display Phenotypic Heterogeneity

A key source of heterogeneity in human embryos is aneuploidy (possessing abnormal numbers of chromosomes) that can lead to pregnancy failure or birth defects.[1,40,124] Interestingly, mosaic embryos with heterogeneous populations of euploid and aneuploid cells potentially have comparable developmental potential as their fully euploid counterparts.[11,12,16] Containing aneuploid hPSCs induced by reversine, gastruloids undergo a selective depletion of the cells with embryonic lineages.[16] However, the precise pathways for aneuploidy depletion in human post-implantation embryos are largely unknown.[16] In mouse and human pre-implantation models, aneuploidy resulted in upregulated autophagy and p53-mediated apoptosis in the depleted cell types.[19–21] Autophagy plays a context-dependent dual role in cell survival and death, as seen in human cancer tumorigenesis and metastasis.[22,24,44] Key differences exist between developmental stages and during embryogenesis between species; therefore, autophagy may play an unique role in aneuploidy depletion in human post-implantation embryos. As a preliminary experiment, euploid (100% untreated cells) and mosaic (50% reversine-treated and 50% untreated cells) gastruloids were screened and sorted on the microraft arrays using the workflow devised previously.

The SOX2 patterning of euploid and mosaic gastruloids have yet to be quantitatively compared. Dynamic latent representations were created from imaging time-series stacks (TYX) by training the model

designed earlier on image stacks of both conditions (euploid and mosaic) from 2 batches (0722 and 0729) [Fig. 4.11]. Interestingly, UMAP dimensionality reduction did not reveal clear separation by batch or condition. Because the model was only trained on a smaller dataset (2 batches per condition) than that of only the euploid gastruloids (7 batches), the dynamic latent representations possibly captured trivial details from the images. Additionally, the euploid gastruloids from these 2 batches showed distinctly variable behavior [Fig. 4.3(c) and Fig. 4.8(b)]. The cell culture may have exhibited excessive intrinsic heterogeneity that overwhelmed the contributions to variability from both batch and condition. This proof-of-concept experiment demonstrated that more experimental replicates are required to discern the heterogeneity of single gastruloids.

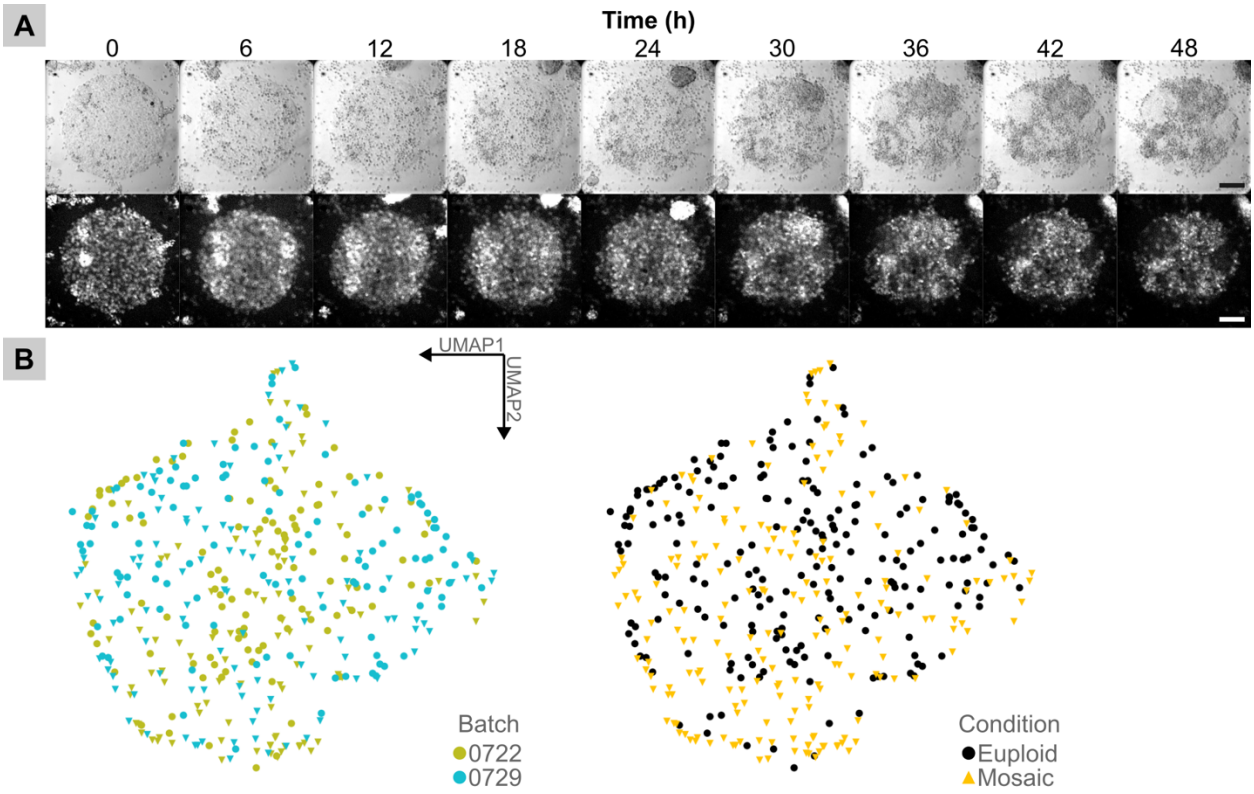

Fig. 4.11. Exploring heterogeneity of single euploid and mosaic gastruloids. (a) Sequential brightfield (upper row) and fluorescence (lower row) images using widefield microscopy of a single microraft possessing a mosaic gastruloid derived from euploid/aneuploid hPSCs expressing a SOX2-mCitrine reporter. Scale bars, 100 μm. (b) UMAP plot visualizing latent representations learned from dynamic TYX stacks of complete imaging time-series of single euploid (circle) and mosaic (triangle) gastruloids. Hue corresponds to batch or condition. N=2 batches for each condition.

4.3.9. Euploid and Mosaic Gastruloids Show Transcriptomic Differences

To further explore the variability of euploid and mosaic gastruloids, the heterogeneous gene expression profiles of both conditions from multiple batches were assessed. 60 individually sorted gastruloids across 2 batches were sequenced ($n_{euploid,0722}$=13 gastruloids, $n_{euploid,0729}$=16 gastruloids; $n_{mosaic,0722}$=16 gastruloids, $n_{mosaic,0729}$=15 gastruloids) [Fig. 4.12]. PCA and heatmap (showing the top 200 highly variable genes) plots revealed clustering of samples mainly by condition and less so by batch [Fig. 4.12(a) and Fig. 4.12(b)]. Interestingly, there were outlying euploid gastruloids from Batch 0722 that had gene expression profiles resembling those of mosaic gastruloids [Fig. 4.12(b)]. The labeled top 10 highly variable genes ranked in order were LINC00458, CER1, LINC01356, MIXL1, T, GLIPR1L1, EOMES, CYP26A1, DKK4, and FGF17. The gene expression levels of all 10 genes were lower in the mosaic gastruloids than those in their euploid counterparts. Interestingly, most of these variable genes overlapped with the variable genes among only euploid gastruloids, except for T (T-box transcription factor T) and EOMES (eomesodermin). This suggested that the overlapping genes were intrinsically variable in the gastruloids regardless of condition. T, also known as the Brachyury (BRA) protein, is conserved across all animals and is mainly required for mesoderm formation in chordates.[125] The BRA+ region in the gastruloids correlates to the mesoderm lineage and exhibits cell behavior similar to the primitive streak region in a gastrulating embryo.[36] Evolutionarily conserved in vertebrates, EOMES performs roles in cell lineage specification, morphogenesis during gastrulation, and extraembryonic tissue formation during intrauterine development.[126] The variable expression of these two genes involved in lineage specification parallels the disruption of normal patterning in gastruloids with aneuploidy.[16] Heterogeneity of gene expression was clearly observed across conditions and experimental batches using the microraft array technology.

The morphological differences between euploid and mosaic gastruloids were highlighted by the model, but the transcriptomic differences have yet to be elucidated on a single gastruloid level. Differentially expressed gene (DEG) analysis was performed on the samples from both conditions [Fig. 4.12(c) and Fig. 4.12(d)]. Out of the 22651 unique RNA transcripts, 379 and 198 transcripts were significantly downregulated and upregulated (FDR<0.05), respectively, in mosaic gastruloids when compared to their euploid

counterparts [Fig. 4.12(c)]. Enrichment analysis based on Gene Ontology (GO) Biological Process terms was conducted to interpret the large set of DEGs [Fig. 4.12(d)]. The processes with the greatest magnitude

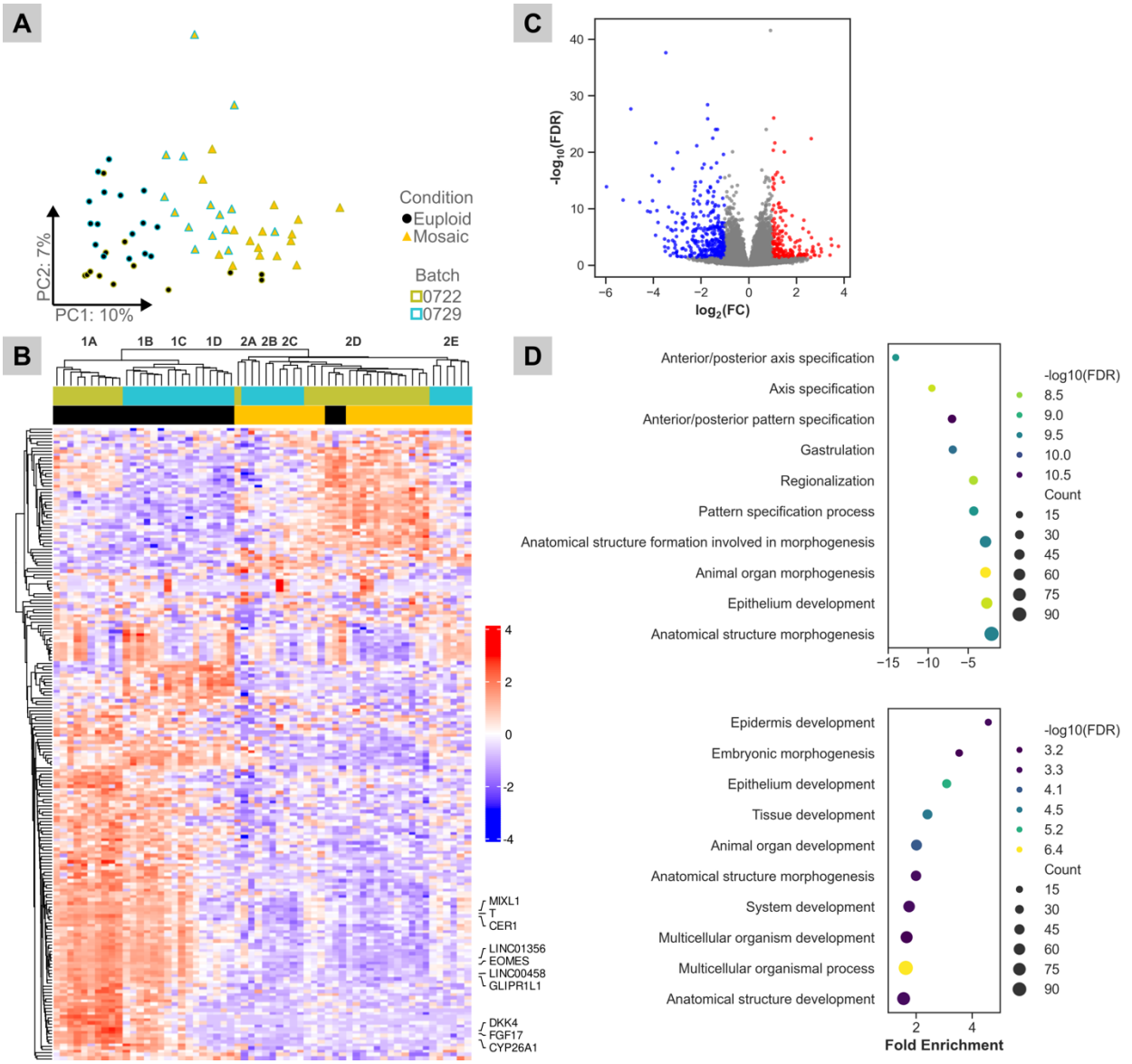

Fig. 4.12. Transcriptomic profiles of single euploid and mosaic gastruloids are heterogeneous. (a) Principal component analysis (PCA) plot of gene expression profiles from single gastruloids. Proportions of variances indicated for PC1 and PC2. Marker hue corresponds to condition. Outline hue corresponds to batch. (b) Heatmap displaying normalized relative expression of the top 200 highly variable genes. Hierarchical clustering of both genes and samples (hues corresponds to condition/batch) was performed using Pearson correlation distance with average linkage. Sample clusters and top 10 highly variable genes were labeled. (c) Volcano plot showing statistically significant downregulated (blue) and upregulated (red) genes below FDR threshold (<0.05) in mosaic gastruloids. (d) GO enrichment analysis of differentially expressed genes in mosaic gastruloids. GO Biological Process terms significantly enriched among downregulated and upregulated genes were shown. Hue corresponds to enrichment significance. Marker size indicates number of genes corresponding to each term. For panels (a-d), N=2 batches for each condition.

fold enrichments were related to embryogenesis—including anterior/posterior axis specification, gastrulation, and pattern specification process. Multiple terms appeared in both plots showing downregulated and upregulated terms, such as epithelium development or anatomical structure development. This can occur when complex pathways are associated with the same GO term. Therefore, dissecting the individual DEGs that constitute each GO term will provide a clearer picture of gene interactions. In addition to obvious morphological differences, euploid and mosaic gastruloids revealed clear transcriptomic differences.

Because the mechanisms of aneuploid depletion in the gastruloids are still unknown, autophagy was hypothesized to play a role in this process. Consequently, the expression levels of genes for autophagy markers (MAP1LC3B and SQSTM1 encodes for LC3B and p62, respectively) and p53-related genes involved in inducing autophagy (TP53, CDKN1A, CCNG1, and BCL2 encodes for p53, p21, Cyclin G1, and BCL-2, respectively) were compared between the euploid and mosaic gastruloids. All these genes except for CDKN1A showed no significant difference between the conditions (FDR>0.05). CDKN1A displayed upregulation in mosaic gastruloids (1.4-fold enrichment, FDR<<0.001). Further analysis is required, because there are important details regarding the experimental design to consider. Firstly, the autophagy levels between the euploid and mosaic gastruloids without additional perturbations might not have been significantly different enough to detect clear differences in the expression levels of this set of genes. In the studies of mouse pre- and post-implantation embryos with aneuploidy, bafilomycin A1 (Baf-A1) and rapamycin were used to disrupt and induce autophagy, respectively.[21] Secondly, gastruloids with greater proportions of aneuploid cells should be assayed for their autophagy levels. There may be a higher threshold of aneuploid cells beyond 50% that would result in significantly different autophagy levels. Lastly, the different cell types in the gastruloids may exhibit variable cellular responses. The mean expression level would thereby average to an intermediate level. In response, single-cell RNA-seq can be performed to dissect the heterogeneous expression levels associated with each tissue layer. This detailed analysis of a human post-implantation model of aneuploidy could potentially help elucidate the novel role of autophagy in embryonic aneuploidy depletion.

4.3.10. Multimodal Characterization of Single Mosaic Gastruloids Connects Phenotypic and Transcriptomic Information

A similar approach to assess the relationship between imaging and sequencing data for single euploid gastruloids was used for single mosaic gastruloids. The dynamic latent representations of sequenced gastruloids for both conditions from Batches 0722 and 0729 were visually assessed by gene expression subcluster [**Fig. 4.13**]. In general, the embeddings of gastruloids with similar gene expression profiles were not necessarily clustered in the UMAP plots. The latent representation of the single mosaic gastruloid from Batch 0722 was distanced from the other latent representations of the mosaic gastruloids from Batch 0729 in Subcluster 2A. In Subcluster 2D, the embeddings of 2 of the 3 euploid gastruloids (the minority) were loosely clustered with those of the mosaic gastruloids from the same batch. The imaging and sequencing appeared to encode orthogonal information, which was similar for the previous analysis with only euploid gastruloids [Fig. 4.9(c)]. Consequently, the convoluted relationship between phenotype and gene expression levels appears to require more robust computational tools to decipher.

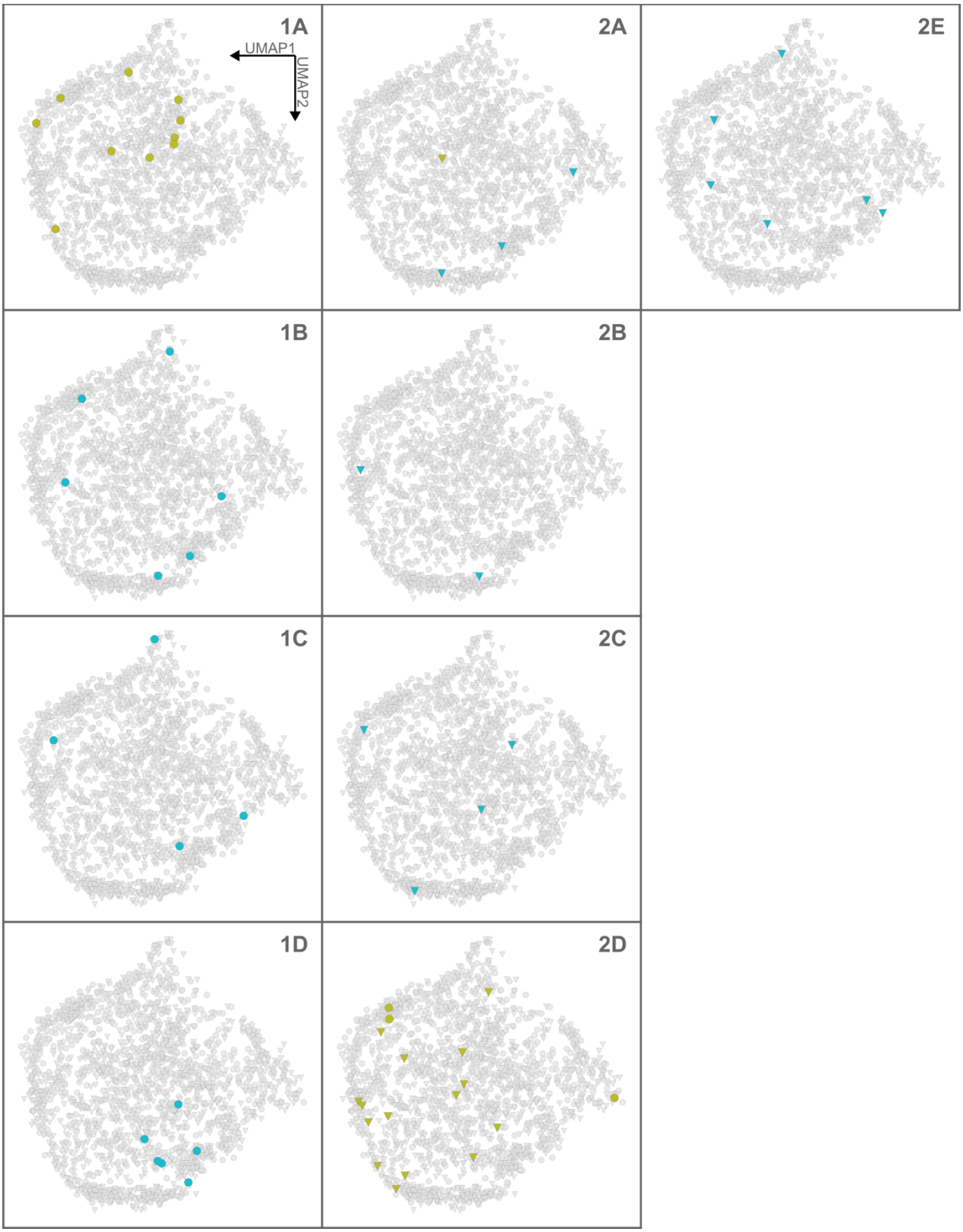

Fig. 4.13. Imaging and sequencing encode orthogonal information. UMAP plots visualizing the dynamic latent representations of the sequenced euploid (large circles) and mosaic gastruloids (large triangles) in each subcluster and of all sequenced gastruloids (small markers). Hue corresponds to batch.

CHAPTER 5. OTHER CONTRIBUTIONS

I have collaborated with Dr. Mia Yang's group (specializing in reproductive health research), Dr. Neda Bagheri's group (specializing in computational biology), and Dr. Cecilia Villegas-Novoa (specializing in an intestinal model). For Dr. Yang's research, I contributed both image analysis and surface patterning. In Wang et al. (2025), the chromosomal instability intrinsic in isogenic trophoblast stem cells (TSCs) and placentas was studied.[127] I measured the surface area of 3D organoids (consisting of TSCs derived via different methods) developing over time. Key pathways involved in spontaneous aneuploidy and continued growth were identified. Additionally, I devised computational tools to quantify the gradient of marker intensity values in stained gastruloids in a high-throughput manner. Applying my skills in photopatterning and microfabrication, I produced consistently patterned glass coverslips for gastruloid culture and designed 3D-printed molds to form PDMS ceilings (to apply pressure on organoids and embryos) for implantation experiments. For Dr. Bagheri's work, I contributed imaging time-series of euploid and aneuploid gastruloids as training data to develop an autoencoder-based model using a Fourier Neural Operator. In return, Dr. Yang and Dr. Bagheri have provided their expertise in embryology and advanced image processing for my project, respectively. I also contributed to the image analysis of the disruption of the mucus layer by microbial toxins in an intestine-on-chip model for Dr. Villegas-Novoa. For reference, please refer to "6.3. Complete List of Publications."

CHAPTER 6. CONCLUSION

6.1. Development of Large Scale Gastruloid Array to Identify Aberrant Developmental Phenotypes

I developed a novel automated technology for the image-based screening and sorting of single gastruloids with heterogeneous patterning behavior. Major innovations to the microraft array system—or microarrays consisting of releasable flat elements (microrafts)—included larger dimensions to accommodate the near-millimeter-sized gastruloids, optimizations to the automated microraft sorting system for the enlarged microrafts, and a novel computational pipeline to categorize colonies based on immunofluorescence images. The focus was on improving the precision of microraft isolations by modifying the motorized needle release and collection devices. To validate this new system, single gastruloids derived solely from euploid or aneuploid cells were sorted based on clear phenotypic differences to measure the relative expression of two biologically relevant genes. Moreover, the microraft array platform detected unique phenotypes within both conditions that are otherwise overlooked with traditional micropatterning of arrays of gastruloids on a monolithic surface. This lays the groundwork for large-scale gastruloids screens. For instance, the microraft array technology can be used to compare mosaic gastruloids (derived from mixtures of euploid and aneuploid cells) or track the divergent development of gastruloids formed from single cells on each microraft. Another potential future direction is to knock out key genes of the BMP, Wnt, and Nodal pathways via CRISPR followed by sorting gastruloids with novel patterning with subsequent gene expression analysis to reveal the signaling networks responsible for normal self-patterning. The development of a more advanced computational pipeline utilizing neural networks to extract complex and high-dimensional features from time-series imaging of the cell fate decisions in the gastruloids (consisting of cells expressing live reporters for the different lineages) can reveal the detailed dynamics of self-patterning, which was limited by the endpoint imaging in this work. Although I demonstrated gene expression analysis using qPCR, devising a workflow to perform bulk RNA sequencing of single gastruloids (or single cells from within a gastruloid) will provide a richer transcriptomic dataset. Furthermore, our strategy to micropattern on numerous large-sized releasable elements within an array can be applied to other multicellular developmental models. Embryonic models in two dimensions (for studying neural differentiation or epithelial-mesenchymal transition) and in three dimensions (such as blastoids

recapitulating the human preimplantation blastocyst and 3D gastruloids modeling complex structures formed during gastrulation) are all compatible with the microrafts with tailored modifications to the microraft dimensions and image analysis pipelines. The microraft array technology opens the door to both high-throughput and high-content screens of embryonic models that can elucidate critical molecular mechanisms during early human embryogenesis

6.2. Heterogenous Patterning Behavior Emerges from Human Pluripotent Stem Cell-Based Embryo Model

Gastruloids serve as a scalable model to quantitatively recapitulate aspects of early lineage specification in human embryogenesis; however, analytical techniques for assessing the emergence of heterogeneity in gastruloids derived from thawed aliquots of a single cell line have yet to be developed. Coupling time-series imaging of a fluorescently tagged lineage (SOX2) reporter in living gastruloids and endpoint transcriptomic data from single gastruloids, the automated microraft array platform revealed key heterogeneous patterning behavior and gene expression profiles among gastruloids between and within batches. Unique advantages of this technology include (*i*) a novel computational pipeline that extracts embeddings directly from the time-series images of the SOX reporter to generate hypotheses regarding biological variability, and (*ii*) the ability to study the RNA-seq data from individual imaged gastruloids. Observing both morphological and transcriptomic information simultaneously allows the parsing of single gastruloid heterogeneity within the same batch, which would be overlooked with bulk or pooled analyses. Future work includes acquiring high-resolution and high-content imaging of additional lineage reporters, since the widefield microscope used here presented limitations detecting the low signal from the live reporters. Because only a single cell line was studied, incorporating additional hPSC lines can potentially reveal cell line diversity. Human models may provide improvements in translatability, reproducibility, and cost-effectiveness over their animal counterparts; however, the gastruloid heterogeneity derived from homogeneous culture conditions calls for careful experimental design that considers single gastruloid differences. Although the variability of *in vitro* models is often reduced for consistency in applications such as drug screens, technical noise of these models can instead be exploited as a proxy for biological noise of diverse developmental dynamics.

6.3. Complete List of Publications

1. Wang, D., Cearlock, A., Lane, K., Xu, C., **Jan, I.**, McCartney, S., Glass, I., McCoy, R., Yang, M. Chromosomal instability in human trophoblast stem cells and placentas. Nat Commun 16, 3918 (2025).
2. **Jan, I.**, Cearlock, A., Yang, M. & Allbritton, N. L. Development of large-scale gastruloid array to identify aberrant developmental phenotypes. APL Bioengineering 9, 026121 (2025).
3. Evarts, J.I., Cain, J.Y., **Jan, I.**, Chiu, P., Allbritton, N.L., Bagheri, N. Inductive bias determines the spatial scale of biological features learned from images. Under review in Bioinformatics Advances (2025).
4. Villegas-Novoa, C., Wang, Y., Wang, H., **Jan, I.**, Sims, C.E., Allbritton, N.L. Geometrically constrained growth factor concentration favors enrichment of goblet cells and mucus formation. Under review in ACS Biomaterials Science & Engineering (2025).
5. **Jan, I.**, Evarts, J.I., Cain, J.Y., Chiu, P., Yang, M., Bagheri, N., Allbritton, N.L. Heterogeneous patterning behavior emerges from human stem cell-based model. Under review in APL Bioengineering (2026).

REFERENCES

1. Nikitina, T. V. & Lebedev, I. N. Stem Cell-Based Trophoblast Models to Unravel the Genetic Causes of Human Miscarriages. *Cells* **11**, 1923 (2022).
2. Currie, C. E. *et al.* The first mitotic division of human embryos is highly error prone. *Nat Commun* **13**, 6755 (2022).
3. Palmerola, K. L. *et al.* Replication stress impairs chromosome segregation and preimplantation development in human embryos. *Cell* S0092867422007802 (2022) doi:10.1016/j.cell.2022.06.028.
4. Coticchio, G. *et al.* Plasticity of the human preimplantation embryo: developmental dogmas, variations on themes and self-correction. *Human Reproduction Update* **27**, 848–865 (2021).
5. West, J. D. & Everett, C. A. Preimplantation chromosomal mosaics, chimaeras and confined placental mosaicism. *Reproduction and Fertility* **3**, R66–R90 (2022).
6. Wu, J. & Barbaric, I. Fitness selection in human pluripotent stem cells and interspecies chimeras: Implications for human development and regenerative medicine. *Developmental Biology* **476**, 209–217 (2021).
7. Baker, N. E. & Montagna, C. Reducing the aneuploid cell burden – cell competition and the ribosome connection. *Disease Models & Mechanisms* **15**, dmm049673 (2022).
8. Infertility FAQs. https://www.cdc.gov/reproductivehealth/infertility/index.htm (2023).
9. Jewett, A. *et al.* 2020 Assisted Reproductive Technology Fertility Clinic and National Summary Report. (2022).
10. Barad, D. H., Albertini, D. F., Molinari, E. & Gleicher, N. IVF outcomes of embryos with abnormal PGT-A biopsy previously refused transfer: a prospective cohort study. *Human Reproduction* **37**, 1194–1206 (2022).
11. Capalbo, A., Poli, M., Jalas, C., Forman, E. J. & Treff, N. R. On the reproductive capabilities of aneuploid human preimplantation embryos. *The American Journal of Human Genetics* **109**, 1572–1581 (2022).
12. Viotti, M. *et al.* Let the data do the talking: the need to consider mosaicism during embryo selection. *Fertility and Sterility* **116**, 1212–1219 (2021).
13. Patrizio, P. *et al.* Worldwide live births following the transfer of chromosomally “Abnormal” embryos after PGT/A: results of a worldwide web-based survey. *J Assist Reprod Genet* **36**, 1599–1607 (2019).
14. Treff, N. R. & Marin, D. The “mosaic” embryo: misconceptions and misinterpretations in preimplantation genetic testing for aneuploidy. *Fertility and Sterility* **116**, 1205–1211 (2021).
15. How Much Does IVF Cost? *Forbes Health* https://www.forbes.com/health/family/how-much-does-ivf-cost/ (2021).
16. Yang, M. *et al.* Depletion of aneuploid cells in human embryos and gastruloids. *Nat Cell Biol* **23**, 314–321 (2021).
17. Starostik, M. R., Sosina, O. A. & McCoy, R. C. Single-cell analysis of human embryos reveals diverse patterns of aneuploidy and mosaicism. *Genome Res.* **30**, 814–825 (2020).
18. van Echten-Arends, J. *et al.* Chromosomal mosaicism in human preimplantation embryos: a systematic review. *Human Reproduction Update* **17**, 620–627 (2011).
19. Regin, M. *et al.* Complex aneuploidy triggers autophagy and p53-mediated apoptosis and impairs the second lineage segregation in human preimplantation embryos. *eLife* **12**, RP88916 (2024).
20. Bolton, H. *et al.* Mouse model of chromosome mosaicism reveals lineage-specific depletion of aneuploid cells and normal developmental potential. *Nat Commun* **7**, 11165 (2016).
21. Singla, S., Iwamoto-Stohl, L. K., Zhu, M. & Zernicka-Goetz, M. Autophagy-mediated apoptosis eliminates aneuploid cells in a mouse model of chromosome mosaicism. *Nat Commun* **11**, 2958 (2020).
22. Mariño, G., Niso-Santano, M., Baehrecke, E. H. & Kroemer, G. Self-consumption: the interplay of autophagy and apoptosis. *Nat Rev Mol Cell Biol* **15**, 81–94 (2014).
23. Liu, J.-T., Wu, S.-X., Zhang, H. & Kuang, F. Inhibition of MyD88 Signaling Skews Microglia/Macrophage Polarization and Attenuates Neuronal Apoptosis in the Hippocampus After Status Epilepticus in Mice. *Neurotherapeutics* **15**, 1093–1111 (2018).
24. Dikic, I. & Elazar, Z. Mechanism and medical implications of mammalian autophagy. *Nat Rev Mol Cell Biol* **19**, 349–364 (2018).
25. Biga, L. M. *et al.* 28.2 Embryonic Development. https://open.oregonstate.education/aandp/chapter/28-2-embryonic-development/ (2019).

26. Solnica-Krezel, L. & Sepich, D. S. Gastrulation: Making and Shaping Germ Layers. *Annu. Rev. Cell Dev. Biol.* **28**, 687–717 (2012).
27. Hayashi, Y., Ohnuma, K. & Furue, M. K. Pluripotent Stem Cell Heterogeneity. in *Stem Cells Heterogeneity - Novel Concepts* (ed. Birbrair, A.) vol. 1123 71–94 (Springer International Publishing, Cham, 2019).
28. Nakamura, S. *et al.* Asymmetricity Between Sister Cells of Pluripotent Stem Cells at the Onset of Differentiation. *Stem Cells and Development* **27**, 347–354 (2018).
29. Lamba, A. & Zernicka-Goetz, M. The role of polarization and early heterogeneities in the mammalian first cell fate decision. in *Current Topics in Developmental Biology* vol. 154 169–196 (Elsevier, 2023).
30. Siegel, J. J. & Amon, A. New Insights into the Troubles of Aneuploidy. *Annu. Rev. Cell Dev. Biol.* **28**, 189–214 (2012).
31. Malle, L. *et al.* Excessive negative regulation of type I interferon disrupts viral control in individuals with Down syndrome. *Immunity* **55**, 2074-2084.e5 (2022).
32. Notarangelo, L. D. & Bosticardo, M. Interferons in Down syndrome: When more is less. *Immunity* **55**, 1967–1969 (2022).
33. Coonen, E. *et al.* Anaphase lagging mainly explains chromosomal mosaicism in human preimplantation embryos. *Human Reproduction* **19**, 316–324 (2004).
34. Viotti, M. *et al.* Using outcome data from one thousand mosaic embryo transfers to formulate an embryo ranking system for clinical use. *Fertility and Sterility* **115**, 1212–1224 (2021).
35. Zhu, W. *et al.* Comparative proteomic landscapes elucidate human preimplantation development and failure. *Cell* **188**, 814-831.e21 (2025).
36. Warmflash, A., Sorre, B., Etoc, F., Siggia, E. D. & Brivanlou, A. H. A method to recapitulate early embryonic spatial patterning in human embryonic stem cells. *Nat Methods* **11**, 847–854 (2014).
37. Santaguida, S., Tighe, A., D'Alise, A. M., Taylor, S. S. & Musacchio, A. Dissecting the role of MPS1 in chromosome biorientation and the spindle checkpoint through the small molecule inhibitor reversine. *Journal of Cell Biology* **190**, 73–87 (2010).
38. Nichols, J., Lima, A. & Rodríguez, T. A. Cell competition and the regulative nature of early mammalian development. *Cell Stem Cell* **29**, 1018–1030 (2022).
39. Coorens, T. H. H. *et al.* Inherent mosaicism and extensive mutation of human placentas. *Nature* **592**, 80–85 (2021).
40. Abdelbaki, A. *et al.* Live imaging of late-stage preimplantation human embryos reveals de novo mitotic errors. *Nat Biotechnol* https://doi.org/10.1038/s41587-025-02851-1 (2025) doi:10.1038/s41587-025-02851-1.
41. Shahbazi, M. N., Siggia, E. D. & Zernicka-Goetz, M. Self-organization of stem cells into embryos: A window on early mammalian development. *Science* **364**, 948–951 (2019).
42. Klionsky, D. J. *et al.* Guidelines for the use and interpretation of assays for monitoring autophagy (3rd edition). *Autophagy* **12**, 1–222 (2016).
43. Shahbazi, M. N. *et al.* Developmental potential of aneuploid human embryos cultured beyond implantation. *Nat Commun* **11**, 3987 (2020).
44. Li, X., He, S. & Ma, B. Autophagy and autophagy-related proteins in cancer. *Mol Cancer* **19**, 12 (2020).
45. Zhao, H. *et al.* Blocking autophagy enhances the pro-apoptotic effect of bufalin on human gastric cancer cells through endoplasmic reticulum stress. *Biology Open* bio.026344 (2017) doi:10.1242/bio.026344.
46. Kim, Y. C. & Guan, K.-L. mTOR: a pharmacologic target for autophagy regulation. *J. Clin. Invest.* **125**, 25–32 (2015).
47. M'hamdi, H. I. Language and labels from the lab: Definitions in the stem cell-based embryo model debate. *Stem Cell Reports* **20**, 102477 (2025).
48. Rossant, J. & Tam, P. P. L. Opportunities and challenges with stem cell-based embryo models. *Stem Cell Reports* **16**, 1031–1038 (2021).
49. Rosner, M., Horer, S., Kiss, I. & Hengstschläger, M. Stem cell-based human embryo models: current knowledge and open questions. *Stem Cell Res Ther* **16**, 471 (2025).
50. Cheng, D., Clark, C. T. & Smith, Q. Advances in engineered models of peri-gastrulation. *iScience* **28**, 112659 (2025).
51. Avni, L., Farag, N., Ghosh, B. & Nachman, I. Gastruloid optimization. *Emerging Topics in Life Sciences* **7**, 409–415 (2023).

52. Martinez Arias, A. *et al.* Criteria for the standardization of stem-cell-based embryo models. *Nat Cell Biol* **26**, 1625–1628 (2024).
53. Beckett, M., Franklin, S. & Rugg-Gunn, P. J. Identifying enabling strategies for effective public dialogue in human embryo research. *Stem Cell Reports* **20**, 102498 (2025).
54. Chhabra, S., Liu, L., Goh, R., Kong, X. & Warmflash, A. Dissecting the dynamics of signaling events in the BMP, WNT, and NODAL cascade during self-organized fate patterning in human gastruloids. *PLoS Biol* **17**, e3000498 (2019).
55. Tewary, M. *et al.* High-throughput micropatterning platform reveals Nodal-dependent bisection of peri-gastrulation–associated versus preneurulation-associated fate patterning. *PLoS Biol* **17**, e3000081 (2019).
56. Smith, A. Formative pluripotency: the executive phase in a developmental continuum. *Development* **144**, 365–373 (2017).
57. Weinberger, L., Ayyash, M., Novershtern, N. & Hanna, J. H. Dynamic stem cell states: naive to primed pluripotency in rodents and humans. *Nat Rev Mol Cell Biol* **17**, 155–169 (2016).
58. Etoc, F. *et al.* A Balance between Secreted Inhibitors and Edge Sensing Controls Gastruloid Self-Organization. *Developmental Cell* **39**, 302–315 (2016).
59. Deglincerti, A. *et al.* Self-organization of human embryonic stem cells on micropatterns. *Nat Protoc* **11**, 2223–2232 (2016).
60. Vuille-dit-Bille, E. *et al.* Tools for manipulation and positioning of microtissues. *Lab Chip* **22**, 4043–4066 (2022).
61. Wang, Y. *et al.* Micromolded arrays for separation of adherent cells. *Lab Chip* **10**, 2917 (2010).
62. Cortés-Llanos, B., Wang, Y., Sims, C. E. & Allbritton, N. L. A technology of a different sort: microraft arrays. *Lab Chip* **21**, 3204–3218 (2021).
63. Jan, I., Cearlock, A., Yang, M. & Allbritton, N. L. Development of large-scale gastruloid array to identify aberrant developmental phenotypes. *APL Bioengineering* **9**, 026121 (2025).
64. Welch, J. D. *et al.* Selective single cell isolation for genomics using microraft arrays. *Nucleic Acids Res* **44**, 8292–8301 (2016).
65. Gracz, A. D. *et al.* A high-throughput platform for stem cell niche co-cultures and downstream gene expression analysis. *Nat Cell Biol* **17**, 340–349 (2015).
66. Kaelbling, L. Introduction to Machine Learning. (2020).
67. Funke, J., Krull, Alexander & Mehta, Shalin. DL@MBL: Deep Learning for Microscopy Image Analysis.
68. Kopf, A. & Claassen, M. Latent representation learning in biology and translational medicine. *Patterns* **2**, 100198 (2021).
69. Chen, K. *et al.* Deep manifold learning reveals hidden developmental dynamics of a human embryo model. *Science Advances* (2025).
70. Ballard, J. L., Wang, Z., Li, W., Shen, L. & Long, Q. Deep learning-based approaches for multi-omics data integration and analysis. *BioData Mining* **17**, 38 (2024).
71. Rotem, O. *et al.* Visual interpretability of image-based classification models by generative latent space disentanglement applied to in vitro fertilization. *Nat Commun* **15**, 7390 (2024).
72. Yang, K. D. *et al.* Multi-domain translation between single-cell imaging and sequencing data using autoencoders. *Nat Commun* **12**, 31 (2021).
73. Zhang, X., Wang, X., Shivashankar, G. V. & Uhler, C. Graph-based autoencoder integrates spatial transcriptomics with chromatin images and identifies joint biomarkers for Alzheimer's disease. *Nat Commun* **13**, 7480 (2022).
74. Heydari, A. A. & Sindi, S. S. Deep learning in spatial transcriptomics: Learning from the next next-generation sequencing. *Biophysics Reviews* **4**, 011306 (2023).
75. Jia, Y., Liu, J., Chen, L., Zhao, T. & Wang, Y. THItoGene: a deep learning method for predicting spatial transcriptomics from histological images. *Briefings in Bioinformatics* **25**, bbad464 (2023).
76. Wang, J. M. *et al.* Deep learning integrates histopathology and proteogenomics at a pan-cancer level. *Cell Reports Medicine* **4**, 101173 (2023).
77. Wakui, T. *et al.* Predicting reprogramming-related gene expression from cell morphology in human induced pluripotent stem cells. *MBoC* **34**, ar45 (2023).
78. Fu, J., Warmflash, A. & Lutolf, M. P. Stem-cell-based embryo models for fundamental research and translation. *Nat. Mater.* **20**, 132–144 (2021).
79. Galgoczi, S. *et al.* Huntingtin CAG expansion impairs germ layer patterning in synthetic human 2D gastruloids through polarity defects. *Development* **148**, dev199513 (2021).

80. Yu, T. & Scolnick, J. Complex biological questions being addressed using single cell sequencing technologies. *SLAS Technology* **27**, 143–149 (2022).
81. Yanik, M. F., Rohde, C. B. & Pardo-Martin, C. Technologies for Micromanipulating, Imaging, and Phenotyping Small Invertebrates and Vertebrates. *Annu. Rev. Biomed. Eng.* **13**, 185–217 (2011).
82. Hwang, H. & Lu, H. Microfluidic tools for developmental studies of small model organisms -nematodes, fruit flies, and zebrafish. *Biotechnology Journal* **8**, 192–205 (2013).
83. Yuan, H. *et al.* Microfluidic-Assisted *Caenorhabditis elegans* Sorting: Current Status and Future Prospects. *Cyborg Bionic Syst* **4**, 0011 (2023).
84. LaBelle, C. A., Zhang, R. J., Armistead, P. M. & Allbritton, N. L. Assay and Isolation of Single Proliferating CD4+ Lymphocytes Using an Automated Microraft Array Platform. *IEEE Trans. Biomed. Eng.* **67**, 2166–2175 (2020).
85. Wheeler, E. C. *et al.* Pooled CRISPR screens with imaging on microraft arrays reveals stress granule-regulatory factors. *Nat Methods* **17**, 636–642 (2020).
86. Smiddy, N. M., DiSalvo, M., Allbritton-King, J. D. & Allbritton, N. L. Microraft array-based platform for sorting of viable microcolonies based on cell-lethal immunoassay of intracellular proteins in microcolony biopsies. *Analyst* **145**, 2649–2660 (2020).
87. Attayek, P. J. *et al.* Automated microraft platform to identify and collect non-adherent cells successfully gene-edited with CRISPR-Cas9. *Biosensors and Bioelectronics* **91**, 175–182 (2017).
88. Blakeley, P. *et al.* Defining the three cell lineages of the human blastocyst by single-cell RNA-seq. *Development* **142**, 3613–3613 (2015).
89. Pai, J.-H. *et al.* Photoresist with Low Fluorescence for Bioanalytical Applications. *Anal. Chem.* **79**, 8774–8780 (2007).
90. Freeburne, E. *et al.* Spatial Single Cell Analysis of Proteins in 2D Human Gastruloids Using Iterative Immunofluorescence. *Current Protocols* **3**, e915 (2023).
91. Otsu, N. A Threshold Selection Method from Gray-Level Histograms. *IEEE Transactions on Systems, Man, and Cybernetics* **9**, 62–66 (1979).
92. Li, C. H. & Tam, P. K. S. An iterative algorithm for minimum cross entropy thresholding. *Pattern Recognition Letters* **19**, 771–776 (1998).
93. Lord, S. J., Velle, K. B., Mullins, R. D. & Fritz-Laylin, L. K. SuperPlots: Communicating reproducibility and variability in cell biology. *Journal of Cell Biology* **219**, e202001064 (2020).
94. DiSalvo, M. *et al.* Characterization of Tensioned PDMS Membranes for Imaging Cytometry on Microraft Arrays. *Anal. Chem.* **90**, 4792–4800 (2018).
95. Schwanhäusser, B. *et al.* Global quantification of mammalian gene expression control. *Nature* **473**, 337–342 (2011).
96. Liu, Y., Beyer, A. & Aebersold, R. On the Dependency of Cellular Protein Levels on mRNA Abundance. *Cell* **165**, 535–550 (2016).
97. NIH to prioritize human-based research technologies | National Institutes of Health (NIH). *NIH* https://www.nih.gov/news-events/news-releases/nih-prioritize-human-based-research-technologies (2025).
98. FDA Announces Plan to Phase Out Animal Testing Requirement for Monoclonal Antibodies and Other Drugs. *FDA* https://www.fda.gov/news-events/press-announcements/fda-announces-plan-phase-out-animal-testing-requirement-monoclonal-antibodies-and-other-drugs (2025).
99. Minn, K. T., Dietmann, S., Waye, S. E., Morris, S. A. & Solnica-Krezel, L. Gene expression dynamics underlying cell fate emergence in 2D micropatterned human embryonic stem cell gastruloids. *Stem Cell Reports* **16**, 1210–1227 (2021).
100. Phipson, B. *et al.* Evaluation of variability in human kidney organoids. *Nat Methods* **16**, 79–87 (2019).
101. Arora, N. *et al.* A process engineering approach to increase organoid yield. *Development* dev.142919 (2017) doi:10.1242/dev.142919.
102. Rufo, J. *et al.* An explainable map of human gastruloid morphospace reveals gastrulation failure modes and predicts teratogens. Preprint at https://doi.org/10.1101/2024.09.20.614192 (2024).
103. LaBelle, C. A., Zhang, R. J., Hunsucker, S. A., Armistead, P. M. & Allbritton, N. L. Microraft arrays for serial-killer CD19 chimeric antigen receptor T cells and single cell isolation. *Cytometry Pt A* **103**, 208–220 (2022).
104. Martyn, I., Siggia, E. D. & Brivanlou, A. H. Mapping cell migrations and fates in a gastruloid model to the human primitive streak. *Development* dev.179564 (2019) doi:10.1242/dev.179564.

105. Kingma, D. P. & Ba, J. Adam: A Method for Stochastic Optimization. Preprint at https://doi.org/10.48550/ARXIV.1412.6980 (2014).
106. Paszke, A. *et al.* PyTorch: An Imperative Style, High-Performance Deep Learning Library. in *Advances in Neural Information Processing Systems* (eds Wallach, H. et al.) vol. 32 (Curran Associates, Inc., 2019).
107. Ge, S. X., Son, E. W. & Yao, R. iDEP: an integrated web application for differential expression and pathway analysis of RNA-Seq data. *BMC Bioinformatics* **19**, 534 (2018).
108. McInnes, L., Healy, J. & Melville, J. UMAP: Uniform Manifold Approximation and Projection for Dimension Reduction. Preprint at https://doi.org/10.48550/ARXIV.1802.03426 (2018).
109. Piccolo, S. *et al.* The head inducer Cerberus is a multifunctional antagonist of Nodal, BMP and Wnt signals. *Nature* **397**, 707–710 (1999).
110. Lou, X., Meng, Y. & Hou, Y. A literature review on function and regulation mechanism of DKK4. *J Cellular Molecular Medi* **25**, 2786–2794 (2021).
111. Jo, K. *et al.* Endogenous FGFs drive ERK-dependent cell fate patterning in 2D human gastruloids. Preprint at https://doi.org/10.1101/2024.07.08.602611 (2024).
112. Oberholzer, Z., Loubser, C. & Nikitina, N. V. Fgf17: A regulator of the mid/hind brain boundary in mammals. *Differentiation* **140**, 100813 (2024).
113. Abu-Abed, S. *et al.* The retinoic acid-metabolizing enzyme, CYP26A1, is essential for normal hindbrain patterning, vertebral identity, and development of posterior structures. *Genes Dev.* **15**, 226–240 (2001).
114. Masamsetti, V. P. *et al.* Lineage contribution of the mesendoderm progenitors in the gastrulating mouse embryo. *Developmental Cell* **60**, 1991-2006.e9 (2025).
115. Jovelin, R. *et al.* Evolution of developmental regulation in the vertebrate *FgfD* subfamily. *J Exp Zool Pt B* **314B**, 33–56 (2010).
116. Gibbs, G. M., Roelants, K. & O'Bryan, M. K. The CAP Superfamily: Cysteine-Rich Secretory Proteins, Antigen 5, and Pathogenesis-Related 1 Proteins—Roles in Reproduction, Cancer, and Immune Defense. *Endocrine Reviews* **29**, 865–897 (2008).
117. Gaikwad, A. S. *et al.* GLIPR1L1 is an IZUMO-binding protein required for optimal fertilization in the mouse. *BMC Biol* **17**, 86 (2019).
118. Zhang, H., Fraser, S. T., Papazoglu, C., Hoatlin, M. E. & Baron, M. H. Transcriptional Activation by the Mixl1 Homeodomain Protein in Differentiating Mouse Embryonic Stem Cells. *Stem Cells* **27**, 2884–2895 (2009).
119. Kaufman-Francis, K. *et al.* Differential response of epiblast stem cells to Nodal and Activin signalling: a paradigm of early endoderm development in the embryo. *Phil. Trans. R. Soc. B* **369**, 20130550 (2014).
120. Chen, Y.-F. *et al.* Control of matrix stiffness promotes endodermal lineage specification by regulating SMAD2/3 via lncRNA LINC00458. *Sci. Adv.* **6**, eaay0264 (2020).
121. Babula, P. *et al.* Mammalian metallothioneins: properties and functions. *Metallomics* **4**, 739 (2012).
122. Lappas, M. Expression and regulation of metallothioneins in myometrium and fetal membranes. *American J Rep Immunol* **80**, e13040 (2018).
123. Saunders, R. A. *et al.* Perturb-Multimodal: A platform for pooled genetic screens with imaging and sequencing in intact mammalian tissue. *Cell* S0092867425005720 (2025) doi:10.1016/j.cell.2025.05.022.
124. Martis, A. S. A. *et al.* Chromosome number alterations cause apoptosis and cellular hypertrophy in induced pluripotent stem cell models of embryonic epiblast cells. *Biology Open* **14**, BIO061814 (2025).
125. Bruce, A. E. E. & Winklbauer, R. Brachyury in the gastrula of basal vertebrates. *Mechanisms of Development* **163**, 103625 (2020).
126. Probst, S. & Arnold, S. J. Eomesodermin—At Dawn of Cell Fate Decisions During Early Embryogenesis. in *Current Topics in Developmental Biology* vol. 122 93–115 (Elsevier, 2017).
127. Wang, D. *et al.* Chromosomal instability in human trophoblast stem cells and placentas. *Nat Commun* **16**, 3918 (2025).